

**The Role of Turbulence on the Entrainment of a Single Sphere
and the Effects of Roughness on Fluid-Solid Interaction**

Mahalingam Balakrishnan

Dissertation submitted to the Faculty of the
Virginia Polytechnic Institute and State University
in partial fulfillment of the requirements for the degree of

Doctor of Philosophy
in
Mechanical Engineering

C. L. Dancey, Chair

P. Diplas

W. F. Ng

E. F. Brown

F. J. Pierce

August 28, 1997

Blacksburg, Virginia

Key Words: Incipient Sediment Motion, Open-Channel Flow, Roughness Sublayer

Copyright 1997, Mahalingam Balakrishnan

The Role of Turbulence on the Entrainment of a Single Sphere and the Effects of Roughness on Fluid-Solid Interaction

Mahalingam Balakrishnan

(ABSTRACT)

Incipient motion criterion in sediment transport is very important, as it defines the flow condition that initiates sediment motion, and is also frequently employed in models to predict the sediment transport at higher flow conditions as well. In turbulent flows, even a reasonably accurate definition of incipient motion condition becomes very difficult due to the random nature of the turbulent process, which is responsible for sediment motion under incipient conditions. This work investigates two aspects, both of which apply to incipient sediment transport conditions. The first one deals with the role of turbulence in initiating sediment motion. The second part deals with the nature of sediment-fluid interaction for more general and complex flows where the number of sediment particles that form the rough surface is varied.

The first part of this work that investigates the role of turbulence in initiating sediment motion, uses a video camera to simultaneously monitor and record the sediment (glass ball) motion and corresponding fluid velocity events measured by a three-component laser Doppler Velocimeter (LDV). The results of the single ball experiment revealed that the number of LDV flow measurements increase dramatically (more than four folds) just prior to the ball motion. The fluid mean velocity and its root-mean-square (rms) values also are significantly higher than the values that correspond to the flow conditions that yield no ball motion.

The second part of the work, investigation of the fluid-sediment interaction, includes five tests with varying number of sediment particles. In order to understand the nature and extent of fluid-solid interaction, velocity profile measurements using the 3-D laser system were carried out at three locations for each of these five cases. Plots of mean velocities, rms quantities located the universal layer at about 1.5 ball diameters above the porous bed. However, at higher sediment particle concentrations, this distance reduced and the beginning of the universal layer approached the top of the porous bed.

Acknowledgments

I am grateful to many people for offering their help, and advice during the course of this study. I sincerely thank my advisor, Dr. C. L. Dancey, for giving me the opportunity to work with him, for being patient and for being a source of constant encouragement during the course of this study.

I thank the members of the committee, Dr. P. Diplas, Dr. F. Pierce, Dr. W. Ng, and Dr. E. F. Brown for their valuable suggestions, and in helping me refine this dissertation.

I am very grateful to Dr. J. B. Jones, and Dr. W. C. Thomas for all the great advice, for providing me with an opportunity to work for them, learn and earn.

I have been very fortunate to have friends of the caliber of John Risi and Athanasios Papanicolaou. Thank you, fellows, for all the good memories, discussions, help and friendship. Many other friends helped me at various stages of my work and I am grateful for all their time and help.

I cannot thank enough my wife, Anu, who put aside her career ambitions and helped me immensely in completing this study, all the while battling a life-threatening, and potentially debilitating illness. Without her extraordinary sacrifice, completion of this study would not have been possible. I wholeheartedly dedicate this work to her.

Through all the tumultuous times my family support was unwavering, and I am very grateful for their patience and understanding.

The support of this work by the United States Geological Society is gratefully acknowledged.

Table of Contents

Abstract	ii
Acknowledgements	iii
List of Figures	viii
List of Tables	xii
Nomenclature	xiii
I: Introduction	1
I-1 Fluid-Solid Interaction and Incipient Sediment Motion	1
I-2 Applications of Fluid-Solid Interaction	2
I-3 Existing Incipient Motion Studies	4
I-4 Objective	7
I-5 Outline of Later Chapters	8
II: Background	9
II-1 Introduction	9
II-2 Rough Wall Flows over Immobile Beds	10
II-3 Classification of Rough Wall Flows	11
II-4 Roughness Sublayer and Surface Packing Density	12
II-5 Flow Regimes Based on Packing Density	14
II-6 Turbulent Bursting Process	16
II-7 Turbulent Flow over Mobile Sediment Beds	20
II-8 Some Complicating Features of Sediment Transport Studies	22
II-9 Stochastic versus Deterministic Approach to Sediment Incipient Motion	23
II-10 The Role of Turbulence in Particle Motion Initiation	25
II-11 Flow Description and Measurement Techniques	27

III: Experimental Facilities	38
III-1 Basic Facilities	38
III-2 Flume	38
III-3 Laser Doppler System	40
III-4 Video Camera	41
IV: Preparatory Work	45
IV-1 Introduction	45
IV-2 Flume Preparatory Work	45
IV-2-1 Flume Slope Calibration	45
IV-2-2 Rough Particle Selection Camera	46
IV-2-3 Test Section Location	48
IV-2-4 Distribution of Particles	48
IV-2-5 Modified Gate Arrangement	51
IV-3 Camera Setup	51
IV-4 Flow Seeding for LDV Measurements	52
IV-4-1 Optical Window for the LDV System	54
IV-4-1 LDV Data Post-Processing	55
V: Experimental Procedure and Data Analysis	68
V-1 Introduction	68
V-2 Basis for the Determination of Flow Conditions	69
V-3 Nondimensional Fractional Entrainment Rate as an Incipient Motion Criterion	73
V-4 Establishing the Hydraulic Conditions	74
V-A Single Ball Experiment	78
V-A-1 Preparation of the Rough Wall	79
V-A-2 LDV Work	80
V-A-3 Camera and Mirror Arrangement	86
V-A-4 LDV Data Post-Processing	88

V·B	Sediment Bed Packing Density Experiments	90
V·B·1	Experimental Flow Conditions	91
V·B·2	LDV Procedure for Packing Density Experiments	93
V·B·3	Camera and Mirror Arrangement	86
V·A·4	LDV Data Post-Processing	88
VI:	Analysis and Results	101
VI·1	Introduction	101
VI·2	Moment Balance of a Single Ball	101
VI·3	Results	106
VI·4	Single Ball Experiment	107
VI·4·1	Correlation Between Ball Motion and Turbulence Events	110
VI·4·2	Correlation Between Ball Motion and Upstream Velocity	110
VI·4·3	Characterization of Velocity Events Prior to Ball Motion	116
VI·4·4	Computing the Critical Condition	122
VI·4·5	Summary	123
VI·5	Sediment Bed Packing Density Tests	125
VI·5·1	Comparison of Different Flow Regimes	128
VI·5·2	Roughness Sublayer	129
VI·5·3	Streamwise Velocity Profiles	130
VI·5·4	Normal Velocity Profiles	132
VI·5·5	Root-Mean-Square Velocity Profiles	134
VI·5·6	Profile of the Reynolds Stress	135
VII:	Conclusions and Recommendations	182
VII·1	Single Ball Experiment	182
VII·2	Sediment Bed Packing Density Experiment	185
VII·3	Recommendations	187
	References	189

Appendix A1: LDV Background	198
Appendix A2: Estimation of Experimental Uncertainty	206
Vita	214

List of Figures

<u>Figure</u>	<u>Page</u>
II·1 Categorization of wall-bounded flows	29
II·2 Different regions in smooth wall flow	30
II·3 Packing density concept. The figure shows 7% packing density	31
II·4 Three regions of rough wall flow based on packing density (Morris, 1955)	32
II·5 Four quadrants in the u-w plane	33
II·6 Plan view of an incompletely packed bed. The dotted lines denote vacant spots	34
II·7 (a) Single, exposed ball atop a porous bed, plan view	35
II·7 (b) Single, exposed ball atop a porous bed, side view	35
II·8 (a) Fully packed bed, plan view	36
II·7 (b) Fully packed bed, side view	36
III·1 Photograph of the flume	42
III·2 Schematic of the flume	43
III·3 The LDV system	44
IV·1 Variation of the non-dimensional bed shear stress, τ_* , with particle's Reynolds number, Re_p	57
IV·2 Angle of repose change due to shift of the 4 th layer balls	58
IV·3 Distribution of roughness particles in the flume	59
IV·4 End plexiglass plate arrangement at flume exit	60
IV·5 Schematic of the modified gate arrangement	61
IV·6 Camera arrangement for the single ball experiment	62
IV·7 Optical window setup for the LDV system	63
IV·8 Tilt of the LDV system	64
V·1 Two fundamentally different ball entrainment situations arising purely from Geometry	97
V·2 Ball distribution for the 20% case	98
V·3 LDV measurement locations for the five sediment bed packing density cases	99

VI.1 Forces exerted on a single, exposed ball placed atop identical spheres	138
VI.2 LDV measurement location for the single ball experiment	139
VI.3 Time series representation of the LDV velocity signals and ball motion	140
VI.4 Variation of ρ with t for $\Delta t = 40000 \mu s$	141
VI.5 Variation of ρ with t for $\Delta t = 100000 \mu s$	142
VI.6 Variation of ρ with t for $\Delta t = 250000 \mu s$	143
VI.7 Time series representation of ball motion and velocity	144
VI.8 Variation of local streamwise mean velocity with τ , $\Delta t = 40000 \mu s$	145
VI.9 Variation of local normal mean velocity with τ , $\Delta t = 40000 \mu s$	146
VI.10 Variation of local streamwise rms velocity with τ , $\Delta t = 40000 \mu s$	147
VI.11 Variation of local normal rms velocity with τ , $\Delta t = 40000 \mu s$	148
VI.12 Probability density function of ϕ for the global and local data	149
VI.13 Probability density function of ϕ for the global and local, and randomly selected data	150
VI.14 Schematic of probability density function for an arbitrary variable, η	151
VI.15 Variation of streamwise mean velocity for the 2% sediment bed packing density case	152
VI.16 Variation of streamwise mean velocity for the 20% sediment bed packing density case	153
VI.17 Variation of streamwise mean velocity for the 35% sediment bed packing density case	154
VI.18 Variation of streamwise mean velocity for the 50% sediment bed packing density case	155
VI.19 Variation of streamwise mean velocity for the 70% sediment bed packing density case	156
VI.20 Variation of normal mean velocity for the 2% sediment bed packing density case	157
VI.21 Variation of normal mean velocity for the 20% sediment bed packing density case	158

VI-22 Variation of normal mean velocity for the 35% sediment bed packing density case	159
VI-23 Variation of normal mean velocity for the 50% sediment bed packing density case	160
VI-24 Variation of normal mean velocity for the 70% sediment bed packing density case	161
VI-25 Variation of streamwise rms velocity for the 2% sediment bed packing density case	162
VI-26 Variation of streamwise rms velocity for the 20% sediment bed packing density case	163
VI-27 Variation of streamwise rms velocity for the 35% sediment bed packing density case	164
VI-28 Variation of streamwise rms velocity for the 50% sediment bed packing density case	165
VI-29 Variation of streamwise rms velocity for the 70% sediment bed packing density case	166
VI-30 Variation of normal rms velocity for the 2% sediment bed packing density case	167
VI-31 Variation of normal rms velocity for the 20% sediment bed packing density case	168
VI-32 Variation of normal rms velocity for the 35% sediment bed packing density case	169
VI-33 Variation of normal rms velocity for the 50% sediment bed packing density case	170
VI-34 Variation of normal rms velocity for the 70% sediment bed packing density case	171
VI-35 Variation of the Reynolds stress for the 2% sediment bed packing density case	172
VI-36 Variation of the Reynolds stress for the 20% sediment bed packing density case	173

VI-37 Variation of the Reynolds stress for the 35% sediment bed packing density case	174
VI-38 Variation of the Reynolds stress for the 50% sediment bed packing density case	175
VI-39 Variation of the Reynolds stress for the 70% sediment bed packing density case	176
VI-40 Schematic of the roughness sublayer	177

List of Tables

<u>Table</u>		<u>Page</u>
II·1	Height above bed at which the effective drag force, F_D , acts (see Bridge and Bennett, 1992)	37
IV·1	Different length scales of the conceptual model of the bursting cycle	65
IV·2	channel length requirement for fully-developed smooth wall flow	66
IV·3	Number of spheres for different sediment bed packing conditions	67
V·1	Summary of hydraulic conditions for the five packing cases	100
VI·1	Relevant time scales for the single ball experiment	178
VI·2	Tabulation of SNR values at different Δt values	179
VI·3	Flow statistics and error estimates of the global and local data	180
VI·4	Extent of the roughness sublayer based on different variables for each packing configuration	181
A2·1	Velocity bias error summary for the streamwise component	211
A2·2	Transformation matrix elements	212
A2·3	Summary of uncertainty from beam angle measurements	213

Nomenclature

The following list includes abbreviations and symbols that are frequently used in this work.

Units are expressed in terms of length (L), time (t), and mass (M).

A_1, A_2	Constants in the moment equation. [M]
C_D	Coefficient of drag.
C_L	Coefficient of lift.
d	Diameter of the particle. [L]
d_f	Mean fringe spacing. [L]
f_a	Average frequency of sediment entrainment. [1/t]
f_d	Frequency of the Doppler signal. [1/t]
f_i	Proportion of fraction i in the bed.
F_D	Net drag force. [ML/t ²]
F_L	Net lift force. [ML/t ²]
f_{mi}	Proportion of the i^{th} size fraction present on the bed surface.
Fr	Froude number.
g	Acceleration due to gravity. [L/t ²]
G	Submerged weight of the particle. [ML/ t ²]
Δh	Height difference. [L]
H	Flow depth. [L]
k_s	Equivalent sand-grain roughness size. [L]
N_E	Number of particles entrained in Δt_{obs} .
N_T	Total number of particles placed in the test area at the beginning of Δt_{obs}
Q	Volumetric flow rate. [L ³ /t]
Q_b	Bed load transport rate. [M/L/t]
q_{bi}	Transport rate of a fraction i per unit width. [1/t]
P_E	Probability of entrainment of a particle.
P	Probability.
Re	Reynolds number.

Re_p	Particle Reynolds number.
S	Slope of the flume.
t	Particle transit time to cross the 8 fringes. [t]
t	Time. [t]
T_B	Mean bursting period. [t]
Δt_{obs}	Period of sediment entrainment observation. [t]
U_B	Depth-Average or bulk velocity. [L/t]
U	Instantaneous stream-wise velocity. [L/t]
U_f	Mean flow velocity at the particle centerline. [L/t]
u_*	Friction velocity. [L/t]
u	Fluctuating stream-wise velocity. [L/t]
u'	Root mean square value of the fluctuating stream-wise velocity. [L/t]
U_+	Normalized stream-wise velocity, defined as $\langle U \rangle / u_*$.
U_N	Standard normal definition of U , $[(U - \langle U \rangle) / u']$.
V	Instantaneous span-wise velocity. [L/t]
W	Instantaneous normal velocity. [L/t]
W	Width of the flume. [L]
W_i	Fractional sediment transport parameter.
w	Fluctuating normal velocity. [L/t]
w'	Root mean square value of the normal velocity. [L/t]
W_i	Velocity bias correction factor. [t/L]
W_+	Normalized normal velocity.
$x, y, z, \text{ or } x_i$	Cartesian stream-wise, span-wise, and normal coordinates. [L]
$()_+$	The + sign denotes normalized variables. Thus, u_+, l_+, k_{s+} , etc. are defined. The normalization is carried out with u_* .
$\overline{(\)}$	The overbar denotes time-averaging operation.
$\langle (\) \rangle$	Ensemble average.

Greek Symbols

α Shape parameter in the gamma distribution.

β	Scaling parameter in the gamma distribution.
l	Wavelength of the laser light. [L]
λ	Porosity of the bed.
θ	Angle between two coherent laser beams.
ν	Fluid kinematic viscosity. [L^2/t]
κ	von Karmann constant.
ρ	Fluid density. [M/L^3]
ρ_s	Particle density. [M/L^3]
μ	Fluid absolute viscosity. [$M/L/t$]
τ	Average bed shear stress. [$M/L/t^2$]
τ^*	Non-Dimensional average bed shear stress.
τ^*_{cr}	Non-Dimensional critical bed shear stress.
ϕ	Variable formed from the moment balance equation for a single exposed ball. Defined as $A_1U^2 + A_2W^2$. [ML^2/t^2]
Φ	Normalized ϕ , defined as $\phi/\langle\phi\rangle$.
$\Gamma(x)$	Denotes the gamma value x.

Abbreviations

LDA	Laser Doppler anemometry
LDV	Laser Doppler velocimetry
pdf	Probability density function
TBD	Time Between Data
TBL	Turbulent boundary layer
VITA	Variable interval time averaging
1-, 2- or 3-D	One-, two-, three-dimensional, respectively

Chapter I

Introduction

I-1 Fluid-Solid Interaction and Incipient Sediment Motion

Interaction between solid surfaces and fluid occurs very frequently in nature as well as in technological processes. Some instances of such interactions may be seen in rivers, oceans, air flow over vegetation canopies, buildings, and vehicular traffic. While the subject of fluid-solid interaction covers a wide range of areas, the current work pertains to sediment transport, where the interaction may include solid motion and/or entrainment.

Consider a situation where a completely immersed, and initially immobile solid particle is resting on a surface and is exposed to a fluid stream. Under appropriate flow conditions, the fluid-solid interaction leads to the displacement of the solid particle. Depending on the flow conditions, the particle once displaced could move either as suspended, saltating or bedload (moving along the bottom wall) material. Both suspended and saltating movements typically occur in extreme, flood-like (for rivers) flow situations. Under such extreme flow situations the mean fluid force acting on the sediment particle itself may be capable of initiating particle motion. However, the bedload regime (which includes rolling or sliding of the particle along the bed) is different in that the mean fluid force is typically incapable of initiating the particle motion. The bedload regime, where the flow just

starts to move the particle, is called the incipient or threshold motion condition for the specified particle. In the present work particle motion and flow near the threshold condition are investigated.

I-2 Applications of Fluid-Solid Interaction

Extensive experimental studies have been carried out in an effort to understand the nature of solid-fluid interaction (e.g., Einstein and El-Samni, 1949; Marshall, 1971; Antonia and Luxton, 1971 and 1972; Bandyopadhyay and Watson, 1988; Rashidi, et al., 1990; Raupach, et al. 1991; and, Grass, et al., 1993). Such studies embrace varied fields such as meteorology, oceanography, and engineering. Fluid-solid interaction investigations can be broadly classified into two categories based on whether the bed material is mobile (Chen, 1970; Fenton and Abbott, 1977; Bettess, 1984; Williams, et al., 1989; Clifford, et al., 1991; and, Lyn, 1992) or immobile (Antonia and Luxton, 1971 and 1972; Grass, 1971; Marshall, 1971; and, Raupach et al., 1991).

Practical applications of immobile rough wall flows are numerous. For example, in the atmosphere the vegetation located on the ground offers a rough, porous surface to airflow. This vegetation is an important factor that determines the rate of ground erosion due to airflow. Architects and designers compute wind forces on buildings by modeling the buildings as 'blocks' immersed in atmospheric turbulent boundary layer (for example, Lee and Soliman, 1977). Other applications of the immobile bed studies include investigation of forces applied to under-water structures.

Study of the mobile bed has many uses. The longevity of dams is predicted by computing the rate of sediment deposition at its foot. Over a long enough period, typically decades, the 'effective' height of the dam available for water storage gets reduced due to sediment deposition and accumulation brought about by the river flow. This height reduction reduces the water storage capacity of the dam. Also, when such a dam with excessive sediment accumulation is discharged, the sediment present at the foot of the dam can cause increased downstream ground erosion and/or deposition. In tropical countries, floods are often encountered during the monsoons (for example, south-east Asia). Increased discharges of these rivers sometimes lead to top-soil erosion of cultivable soil. This in turn, affects the agricultural productivity and economy of the region. The applications mentioned above typically involve above-normal flow situations. However, mobility of bed material, even under flood-like flow situations, is computed based on the information of incipient condition. Thus, investigation of incipient conditions of sediments is of paramount importance.

As stated earlier, under incipient conditions, the mean fluid force may be incapable of moving the sediment; however, instantaneous turbulent fluid forces, frequently several times larger than the mean, can initiate the motion, and the mean force may help sustain it. Experimental investigation of incipient conditions, provides the opportunity to observe and measure the effect of turbulence on sediment motion initiation, and help enhance our understanding of the role of turbulence in sediment transport. The flow condition that may be regarded as "incipient" or "threshold" for the specific bed material is very important in determining bed or channel stability and in estimating the bed erosion rate around under-

water structures, such as bridge piers. In fact, the notion of a “threshold” condition is frequently used in models for predicting sediment transport for conditions in excess of threshold. For example, Paintal (1971) modeled the dimensionless bed material transport rate, q_{s*} as,

$$q_{s*} = 13 \left(\tau_{0*}^{2.5} \right) ; \quad \text{for flows close to incipient conditions} \quad [\mathbf{I}\cdot\mathbf{1}]$$

$$q_{s*} = 6.56 \left(10^{18} \right) \tau_{0*}^{16} ; \quad \text{for flows higher than incipient conditions} \quad [\mathbf{I}\cdot\mathbf{2}]$$

Where, τ_{0*} is the threshold or incipient stress value. In this case, τ_{0*} is treated as a mean bed shear stress level, rather than a turbulent fluctuating level, above which significant transport occurs and below which almost no transport occurs.

The incipient motion condition also plays an important role in predicting the rate of removal (cleansing) of solid contaminants, that may otherwise stay in the interstices between large rough bed particles, possibly causing depletion of dissolved oxygen, affecting the under-water life forms.

I-3 Existing Incipient Motion Studies

Most of the existing incipient motion criteria are deterministic in nature. By deterministic it is meant that the flow parameters that are used to define threshold conditions typically have a well-defined value, which remains constant for the given flow condition. Such a deterministic criterion assumes that the mean flow parameters, such as the bed-shear (Shields, 1936; Paintal, 1971) or the mean velocity (Neill, 1967), can accurately model the sediment transport rate. For example, for sediment of specified size, shape and density a particular value of the mean bed shear stress might be used to define the incipient or

threshold of motion for the sediment (see for example, Equations I-1 and I-2). One procedure for obtaining this value may involve collecting transported sediment at the downstream end of a laboratory flume at different flow conditions. The threshold shear stress, then, corresponds to the flow condition at which zero sediment transport rate occurs, as determined through linear extrapolation of the data (Shields, 1936).

Several researchers (e.g., Gessler, 1965; Fenton and Abbott, 1977; Grass, 1983; and, Naden, 1987) have observed that under a range of conditions, incipient particle motion occurs rather randomly, indicating that the stochastic turbulent field may be the reason for particle motion initiation, and not the mean quantities that have traditionally been used. This implies that the deterministic approach employed in defining incipient motion is too simplistic, and that a stochastic model may be more appropriate. In support of the stochastic approach, it must be mentioned that many researchers have observed sediment motion even under very low flow conditions (lower than the “established” deterministic threshold values), strongly indicating that the movement of the particle is determined by the occurrence of a chance or a random turbulent flow event, large enough to move the particle. The reader is directed to Papanicolaou’s (1997) work that provides a detailed comparative discussion of various deterministic and stochastic incipient motion criteria.

A stochastic approach to determining the sediment incipient criterion has been suggested previously by others (e.g., Einstein and El-Samni, 1949; Gessler, 1965; Chen, 1970; Christiansen, 1977; Grass, 1983; and, Naden, 1987). Despite their potential advantages, the stochastic models have not been widely accepted, and continue to exist as

“sound” concepts that have little field use. The basics of the stochastic approach are considered next.

The turbulent fluid forces exerted on a particle, and the inter-particle arrangements of a mobile bed are random events that can be characterized better by a probabilistic approach rather than a deterministic one. The stochastic model assumes that particle motion under incipient conditions is initiated by randomly occurring instantaneous, turbulent events that are several times greater in magnitude than their time-averaged counterparts. As mentioned before, though the stochastic approach has been suggested previously by other researchers, to the best of the author’s knowledge the approach has never been seriously developed nor implemented in practice and has not supplanted the deterministic approach used by practicing engineers for decades. One of the goals of this investigation and Papanicolaou’s (1997) work, therefore, is the formulation, definition and implementation of a stochastic approach, that employs the probability of entrainment of a particle as the determining criterion in defining the incipient condition (the concept of probability of particle entrainment is described and revisited in later chapters).

I-4 Objective

The overall objective of the research program was to establish a consistent incipient motion criterion accounting for the stochastic nature of the entrainment process. Two separate investigations were developed for the purpose of achieving this objective.

- i. Experimentally establish the correspondence between specific turbulent velocity events and particle motion for a single exposed ball placed atop a porous bed of identical

particles in a fully-rough wall flow. The flow during this investigation represents the incipient condition for the “isolated regime” (defined later). This investigation is referred to as the single ball experiment.

- ii. Investigate the nature of sediment-fluid interaction under incipient conditions for sediment beds with many mobile spheres under different sediment bed packing conditions. The incipient condition is based on the stochastic concept that considers probability of entrainment of the particle (to be discussed later) as the determining criterion.

This latter investigation (detailed in Papanicolaou, 1997), is referred to as the packing density case, since the flow conditions appropriate to incipient motion vary with the concentration or “density” of the mobile spheres. Item “i” is the main focus of the present work, although the two studies are complementary. Some velocity field measurements appropriate to “ii” are also presented in this thesis. The investigation of ii with mobile spheres is the subject of Papanicolaou’s (1997) work. Results of this work were used by Papanicolaou in deducing the particle incipient motion criterion that considered the stochastic nature of the flow.

I-5 Outline of Later Chapters

In Chapter II, background information is presented, followed by a description of the experimental facilities in Chapter III. Chapter IV outlines the experimental preparatory work, Chapter V includes the experimental methodology and data acquisition, followed by

results in Chapter VI. Conclusions are outlined in Chapter VII, followed by the References section. The Appendices are provided at the end.

Chapter II

Background

II·1 Introduction

In Chapter I, the major goals of the work were listed in general terms. In this chapter relevant background information is presented. Rough wall investigations can be divided into two categories, based on whether the bed is immobile or mobile. Both are reviewed here. The flow chart shown in Figure II·1 provides an overview of flow classifications pertinent to rough wall flows.

The immobile bed material presented here includes, a brief review of the rough wall studies, rough wall flow classification based on roughness size and the concept and definition of sediment bed packing density, a discussion on the roughness sublayer, and the turbulent bursting process.

The discussion on mobile bed reviews the sediment motion in geophysical flows, followed by the simplifications effected in this work. Next, the stochastic approach to modeling sediment transport is compared with the deterministic approach. The objectives of this work are repeated at the end of this chapter.

II·2 Rough Wall Flows over Immobile Beds

Rough flows over an immobile bed have no sediment motion associated with them. Such flows have been extensively investigated by several researchers (e.g., Nikuradse, 1933; O’Loughlin, 1965; Wooding et al., 1973; Raupach et al., 1980), and have applications in varied fields such as meteorology, building construction, and hydraulics. Generally speaking, the presence of roughness favors transition to turbulence. This results from the additional flow perturbations generated by the presence of the roughness, on top those present in the free stream itself. However, the relative magnitudes of the perturbations associated with the roughness and the flow are important. If the roughness elements are very small in physical size, their effect on the flow may be insignificant; thus, the flow may be closer to that over a smooth wall. In such a case transition to turbulence occurs at conditions close to those for smooth wall flows and the turbulent flow field behaves as if the wall were smooth. If the roughness size is large, then the effects of the roughness may make a significant contribution to the total flow perturbation generated, thus, hastening transition to turbulence and the turbulence about such a rough wall is directly influenced by the roughness elements. Thus, earlier investigations were geared toward establishing the relative “sizes” of the roughness (Schlichting, 1979) and their influence on the flow. Using the roughness size as the criterion, roughwall flows are categorized into three regimes (shown in Figure II·1). The three categories and the criterion are reviewed next.

II·3 Classification of Rough Wall Flows

Rough immobile wall flows, classified based on the size of the roughness, fall into three distinct flow regimes. Actual roughness physical size is not appropriate for the classification of rough flows, only the roughness size as compared to flow length scales is relevant, thus the Reynolds number based on the roughness size, $Re_p = k u_* / \nu$, is typically employed as the criterion to delineate the three regimes as:

- (a) hydrodynamically smooth for $Re_p \leq 5$
- (b) intermediate region for $5 < Re_p \leq 70$
- (c) fully rough for $Re_p > 70$

where, k is the roughness height (for a ball or sphere it is its diameter, d), u_* is the friction velocity defined as $(\bar{\tau}_{wall}/\rho)^{1/2}$, where ρ and ν are the fluid density and kinematic viscosity, respectively, and $\bar{\tau}_{wall}$ is the time-averaged shear stress exerted by the fluid on the bottom wall.

Small particles that can be buried within the viscous sublayer (refer to Figure II·2), constitute the hydrodynamically smooth regime. In this regime the viscous stresses play a more dominant role in entraining the particles. Bigger particles that protrude through the viscous sublayer into the buffer layer (refer to Figure II·2), experience both viscous and pressure drag, while particles that extend all the way into the logarithmic layer (refer to Figure II·2), experience mostly pressure drag (Schlichting, 1979). The pressure drag (equivalently called form drag) is typically modeled adequately by the square of the local velocity (to be discussed).

In this work only the fully rough case was considered, as it is more common in gravel bed river flows. Most of the earlier rough wall investigations typically considered only a completely packed sediment bed and the effect of sediment bed packing density (to be discussed) on overall bed resistance to the flow was not considered. A “completely packed sediment bed” has the maximum number of sediment particles packed in a given volume. If the packing is less than the maximum possible, then the bed is incompletely packed. The need for examining the role of surface packing has been expressed by several researchers (e.g., Naden, 1987; Billi, 1988; Reid et al., 1992; Ling, 1995). The reason for such a suggestion is that the sediment transport characteristics are affected by the sediment bed packing density, and the bed resistance changes as packing conditions are altered (Schlichting, 1979).

II-4 Roughness Sublayer and Surface Packing Density

The following discussion pertains to a fully rough case (i.e., $Re_p > 70$). Even in the fully rough case the fluid-solid interaction leads to the formation of a disturbed fluid layer called the roughness sublayer (see, for example, Raupach et al., 1991). Presence of the roughness particles and projection above the viscous sublayer leads to wake formation downstream of the roughness elements. Wakes from each of the multiple particles may interact to create a fluid layer that is very non-homogeneous. The fluid layer associated with the element wakes is called the roughness sublayer. Within the roughness sublayer the flow is highly disturbed, non-homogeneous, and is locally influenced by the roughness geometry. The local roughness sublayer thickness depends on individual roughness element shape, the

particle's position with respect to the neighboring elements, and the incident flow direction. The fluid disturbance (or wake diffusion) created due to the presence of the solid elements, decays in the direction that is normal to the plane containing the roughness elements (Raupach et al., 1991). Beyond the roughness sublayer the turbulent flow is generally regarded as universal and, in essence, does not reflect the details of the bottom boundary condition, except through the mean wall shear. One of the goals of this work is to investigate and identify differences in turbulent flow field characteristics within the roughness sublayer for different sediment bed packing conditions, which may lead to a better understanding of fluid-solid interaction. Since formation of the roughness sublayer depends on the mutual location of the roughness particles, the sediment bed packing density is defined next.

Surface packing density, loosely speaking, denotes the inter-particle distance. A particle's position with respect to its neighbors (in the same layer or plane) defines the surface packing density or simply referred to as the packing density. Typically, surface packing density is defined as the ratio between the total frontal (sometimes, plan area) area of the particle to the total ground area on which they are located. Figure II-3 illustrates the concept of surface packing density. Based on Raupach et al.'s (1991) definition, the surface packing density, λ , can be defined as

$$\lambda = \frac{hl_y}{D^2} \quad [\text{II}\cdot\mathbf{1}]$$

where h is the height of the roughness layer (for a bed of spheres, it is the diameter, d), l_y , the particle dimension in y direction (d , here), and D , the particle mean separation distance,

defined as $D \equiv (A/n)^{0.5}$, where A is the horizontal ground area upon which ‘ n ’ particles are located.

The surface packing density could also be defined such that it includes the porosity, ϵ , of the bed. Porosity of a bed is defined as the fraction of the total volume that is not filled by the roughness elements. Thus, ϵ depends on the geometry of the roughness particles that form the bed. For example, a tightly packed bed of spheres has an ϵ -value of about 0.3.

In this work the packing density, S_p , is defined based on the ratio of actual particles (N_a) that are placed in a given area, A , to the maximum number (N_T) that can be placed in A . Thus,

$$S_p = \frac{N_a}{N_T}(1 - \epsilon) \quad [\text{II}\cdot\text{2}]$$

When N_a equals N_T , the bed is fully or completely packed. Then, the packing for that case becomes 70 %. Next, flow categorization based on surface packing density is discussed.

II-5 Flow Regimes Based on Packing Density

In Section II-3 rough wall regimes based on particle size were addressed. Here rough wall regimes based on the sediment bed packing density are reviewed (refer to Figure II-1). Morris (1955), and later, Lee and Soliman (1977), identified three distinct regimes of bed friction based on different packing densities. The three regimes based on sediment bed packing density are:

1. Isolated roughness regime, that corresponds to a surface packing density that is less than about 8% ($S_p \leq 8\%$). In this regime the roughness elements are sufficiently isolated such that fluid separation (wake formation) and reattachment occurs before the next particle is encountered, so that any given particle does not 'feel' the presence of any of its neighbors, and behaves as if it is isolated.
2. The wake interference regime, ($8\% \leq S_p \leq 40\%$) where downstream particles are in the wake of those upstream. In this regime the roughness particles are close enough that the wakes generated by individual particles interact.
3. The skimming regime, ($S_p \geq 40\%$) where the flow appears to skim the crest of the roughness. Here the particles are so close together that the flow appears to skim the roughness surface.

Figure II-4 shows three packing density cases, 2 %, 20 %, and 70 %, that encompass the three regimes discussed above. The single ball experiment belongs to the isolated regime. The five sediment bed packing density tests encompass all three regimes, the isolated (2% case), the wake interference (20% and 35% cases), and the skimming flow (50% and 70% cases) regimes.

The discussion on immobile rough walls provided thus far included some important features of the flow, and categorization based on roughness size and packing density. Next, the smooth and rough turbulence structure in the wall layer is considered. It is well known that both smooth and rough wall flows have very similar turbulence structure in the outer layer, a region of weak shear. However, both the flows differ in the wall layer in that they are characterized by length scales that are vastly different. The wall layer of the smooth wall

flow is characterized by viscous length scales, while the rough wall flows, by the size of the roughness located on the bottom surface.

The wall layer of both smooth and rough wall flows is a region of intense shear, generating turbulent kinetic energy. The energy for this intense turbulent activity is derived from the core part of the flow, a site of weak shear. Fluid momentum exchange between the low-speed fluid near the solid boundary, and the high-speed core flow, is described by the Reynolds shear stress term, $\langle uw \rangle$ (transfer of x moment (u), in the z (w) direction). Here, u and w are the fluctuating streamwise and normal velocity components, respectively. Thus, in this work, $U = \langle U \rangle + u$, and $W = \langle W \rangle + w$, and so on, with “ $\langle \rangle$ ” denoting ensemble-averaging). The turbulent bursting process is closely related to the generation of turbulent energy and Reynolds shear stress in the near wall region, and, it has been suggested that uw and turbulent bursts are closely related to many other boundary phenomena such as heat (Rajagopalan and Antonia, 1982), mass transfer (Komori et al., 1982), and sediment motion (e.g., Grass, 1983; Williams et al., 1989). Because of its presumed relevance to sediment transport, the turbulent bursting process is reviewed next.

II-6 Turbulent Bursting Process

Ever since Kline et al. (1967) and Corino and Brodkey (1969) identified the turbulent bursting process for smooth wall flows, enhancement of most of boundary phenomena, such as heat transfer, mass transfer and sediment transport, have been linked to turbulent bursting events. Here the discussion is restricted to sediment motion.

Grass' (1971) flow visualization study over smooth and rough walls established the existence of turbulent bursts in rough wall flows and identified more violent bursting activity in rough wall flows than in the smooth wall case. This observation lent further credence to the assumption that bursts are responsible for sediment motion.

The existence of turbulent bursts has been confirmed by several researchers both in smooth, as well as, rough wall flows. However, investigations of the turbulent bursting phenomenon on smooth walls far exceed those for rough wall (e.g., Nezu and Nakagawa, 1991) flows. In flows with rough or smooth walls the events that constitute a bursting cycle and their sequence of occurrence are the same. The following sequence of events describe a bursting cycle in smooth wall flows. The bursting cycle begins with the lift up of a low-speed fluid parcel close to the solid boundary, from within the viscous sublayer, referred to as an ejection. This fluid parcel continues to rise, and when it reaches the buffer region, an oscillatory motion sets in. The amplitude of this oscillation increases, until rapid disintegration of the fluid parcel results. The rapid disintegration is brought about by violent turbulent mixing. High-momentum fluid from the core part of the flow rushes toward the wall to presumably replace the fluid removed during the ejection phase of the bursting process. The inrush of the core fluid is termed a sweep. Though the sequence of events described above is common to both smooth and rough walls, the burst-generation mechanisms in smooth and rough walls are believed to be different. For the smooth wall, the presence of a continuous solid surface, retards and organizes fluid motion in the form of low-speed streaks (e.g., Kline et al., 1967; Corino and Brodkey, 1969; Offen and Kline, 1974). These are the streaks that lift off from near the smooth wall. In rough wall flows the

low-speed streaks are less conspicuous (Sumer and Deigaard, 1981; Grass, 1973; Grass et al., 1991), presumably because the roughness elements ‘break’ the low-speed fluid parcels. Consequently, the parcels actually tend to scale with the roughness size (Grass, 1971). The main differences in sweeps and ejections between smooth and rough wall flows appeared to be mainly associated with the detailed mechanics of the low momentum fluid entrainment at the bottom bed, following sweeps. In the smooth wall viscous layer, and in rough walls, the fluid trapped in the roughness interstices, serve as the reservoir of low momentum fluid, which is drawn on during the ejection process (Grass, 1971). In rough wall flows, features such as vortex shedding of individual particles have also been suggested as possible mechanism for the bursting cycle generation (e.g., Gyr, 1983).

To summarize, the turbulent bursting process -- common in both rough and smooth wall flows -- is envisaged as a consequence of a three-dimensional instability mechanism which is not yet fully understood. The bursting process mainly consists of the sweeping events that bring in high-momentum fluid from the core part of the flow to the boundary, and ejection events that transfer momentum from near the boundary to the core.

Flow visualization studies have identified the bursting process as a mass of fluid with phase-correlated (coherent) vorticity, called a coherent structure (see, Hussain, 1983, for a thorough discussion on coherent structures). The spatial extent of this fluid mass defines its extent in space. While flow visualization studies have helped obtain extensive qualitative data on coherent structures, they have not provided detailed information at each point of the coherent structure. In order to obtain such “hard” quantitative data, single point measurement techniques, such as x-wire anemometry, and laser Doppler velocimetry (LDV)

have been used. But these single point measurement techniques provide useful quantitative data at only one point of the coherent structure, while providing very little information about the rest of the flow structure. This situation challenged researchers to introduce imaginative schemes to deduce the nature of the coherent structure from single point measurements.

The characterization of the coherent structures from the commonly-used single-point measurement techniques, is achieved by employing special analysis schemes. Popular ones among these schemes are the quadrant method (Willmarth and Lu, 1972), the u-level algorithm (Luchic and Tiederman, 1987), and the Variable Interval Time Average Technique, or VITA (Blackwelder and Kaplan, 1976).

Of these schemes the quadrant method comes highly recommended due to its superior correspondence between visual and detection methods (Nezu and Nakagawa, 1991). The quadrant method divides the uw -plane into four quadrants based on the sign of u and w . They are, the outward (1st quadrant, $u > 0, w > 0$) and inward interactions (3rd quadrant, $u < 0, w < 0$), ejection (2nd quadrant, $u < 0, w > 0$), and sweeps (4th quadrant, $u > 0, w < 0$). The idea behind this classification is to categorize and identify specific portions of the burst cycle that are important in momentum transport and the production of turbulent energy and Reynolds stress. Figure II-5 shows the four quadrants in the u - w plane and the so called hole event (Willmarth and Lu, 1972). The hole size, H determines the magnitude of uw -events that are included in the region defined by the hyperbolas shown in Figure II-5. The quadrant method was employed in this work; its implementation will be discussed later.

Next turbulent flow over a mobile sediment bed is considered. The flow condition at which the previously-immobile bed becomes mobile is addressed. The section includes

definition of incipient motion, a review of the deterministic and stochastic models of sediment transport, and shortcomings of the existing models.

II·7 Turbulent Flow over Mobile Sediment Beds

In this section background information on a mobile sediment bed is presented. Shields (1936) used naturally occurring sediment and measured the gravel transport rate at different flow conditions to establish the relation between sediment transport rate and *average* bed shear. The result of this work is perhaps, one of the most widely used sediment transport studies. Deviations from Shields results, observed by several researchers were mainly from the uncertainty in the estimation of the average bed shear stress, and due to the uneven nature of the sediment particles themselves (such as shape, size, density, number of particles available to move, and bed geometry. See Naden, 1987, for example). Some of the earlier studies investigated the role of instantaneous turbulent quantities on sediment transport (e.g., Kalinske, 1939; Gessler, 1965; Naden, 1987), while others examined the role of relative particle protrusion (Fenton and Abbott, 1977; White and Day, 1982).

Consider an initially immobile sediment bed. As the flow is increased, at some specified flow discharge, sporadic movement of sediment is detected. Under these flow conditions, the sediment bed is mobile. Continued increase of the flow discharge will lead to greater sediment motion, and as discussed in Chapter I, the flow conditions may start to resemble flood-like conditions. In this work, such extreme flow conditions were not considered. Instead, attention was restricted to flow conditions at which the sediment particles just start to be moved.

The flow condition at which sporadic movement of sediment just begins to occur is referred to as the incipient condition of the sediment. The incipient condition of a sediment particle refers to the *flow* condition that causes the sediment to just begin to move. What flow condition is adequate to cause such a motion depends on the characteristics of the sediment, such as its weight, size, shape, and geometrical feature of the surrounding sediment. Usually, the incipient motion condition of a specified sediment particle is visually judged by the experimenter, thus, probably, tainted by “subjective” judgment. The existence of the incipient condition itself has been considered by some researchers as being artificial (e.g., Paintal, 1971; He and Han, 1982). The difficulties in establishing the incipient condition accurately is complicated by the stochastic nature of the turbulent flow, sediment particle size, shape, density, inter-particle arrangement, and numerous other factors discussed in the next section.

II-8 Some Complicating Features of Sediment Transport Studies

As stated earlier, the problem of sediment incipient motion in general, depends on the particle shape, size and density non-uniformities, its cohesiveness and orientation with respect to the flow, geometrical arrangement of surrounding particles, and non-uniformity of the bed level.

Non-uniform particle size and shape add to the complexity in investigating the mobility of natural gravel. It should be noted that some of the earlier experimental, theoretical, and modeling studies (Bettess, 1984; Bridge and Bennett, 1992; Clifford, et al., 1991; and, Drake et al., 1988) were done with natural gravel as the sediment, which typically

has widely varying size and shape. Different sizes and shapes affect the flow field locally around the particles, thus altering the nature of solid-fluid interaction, producing more scatter in the experimentally determined incipient motion threshold values. In most of these studies the mobile bed layer was completely packed, and the effect of inter-particle distance on fluid-sediment interaction, and the particle entrainment rate were not investigated. In other words, most of the investigations considered a gravel bed that was tightly packed. Sediment transport studies of loosely or incompletely packed beds (Figure II-6 is an example of an incompletely packed bed) are not common. The effect of an incompletely packed bed on sediment transport is important, as packing density is an additional parameter that may affect the nature of fluid-solid interaction, and the sediment incipient motion condition itself.

The net effect of variable particle size, shape and density is that the fluid force required to initiate particle motion varies throughout the bed. The virtually countless permutations of inter-particle arrangement adds further to the complexity of the problem. In this work, spheres of same diameter and density were employed as sediment particles in order to avoid this complication. Equi-sized spheres minimize variable-size, -shape and -density effects. Since the bed was leveled flat, problems due to bed non-uniformity were reduced as well.

Next, traditional modeling approaches to predicting sediment incipient motion are addressed. Basically two modeling approaches are followed, and both were briefly discussed in Chapter I. They are the deterministic, and the stochastic approaches.

II-9 Stochastic versus Deterministic Approach to Sediment Incipient Motion

In Chapter I, the more-common deterministic approach to sediment transport modeling was introduced and briefly contrasted with the stochastic approach. The deterministic approach models sediment transport as a function of the flow mean parameters such as time-average bed friction (Shields, 1936) or flow mean velocity (Neill, 1969). Shields' (1936) pioneering work, employed similarity theory to describe incipient motion, and continues to hold a very important place in sediment transport research. Several extensions to Shields work have been forwarded in an attempt to include effects of low particle Reynolds number (Mantz, 1977), particle relative protrusion (Fenton and Abbott, 1977), and particle size and shape (Komar and Li, 1986). Other studies considered the balance of fluid drag force and immersed particle weight (Egiazaroff, 1965), balance of moments created by fluid lift, drag forces, and the immersed weight (Coleman, 1967). Sediment motion models based on similarity models have been forwarded by Neill and Yalin (1969), and Yalin (1977). Wilcock (1988) extended their work to include effects of non-uniform sediment size. To summarize, the deterministic models have the following shortcomings:

1. The models ignore the effects of instantaneous turbulent fluid forces on sediment entrainment and assume that the flow mean values determine the incipient values for the specified sediment.
2. The particle size, shape, inter-particle arrangement are considered deterministic, whereas, in reality, they are not.

3. The models do not account for the effect of sediment bed surface packing density on sediment entrainment characteristics.

The stochastic approach models sediment motion based on instantaneous fluid forces exerted on sediment particles. The stochastic concept and the role of turbulence has been addressed by various researchers (e.g., Lane and Kalinske, 1939; Einstein and El-Samni, 1949; Gessler, 1965; Nakagawa and Nezu, 1981; Grass, 1983; Sekine and Kikkawa, 1988; Naden, 1987). Some of the listed works are outlined in Section II-4. In Chapter I, for sediment incipient conditions, the stochastic approach modeling was favored over the deterministic approach.

While, conceptually the stochastic approach appears to hold more promise in modeling the role of turbulence in initiating particle motion, several questions remain unanswered:

1. For a given bed configuration and surface packing density, the turbulent flow (force) event that most frequently causes sediment motion is not known.
2. The roles which different flow events play in initiating particle motion under different surface packing conditions is not known. For example, a single exposed particle (see, Figures II-7a and II-7b) is likely to experience more form drag, F_D (to be discussed) than skin friction. However, a particle in a fully packed bed (refer to Figures II-8a and II-8b), will initially move vertically due to the lift force, F_L (to be discussed). Thus, from a physical argument, form drag plays a less dominant role in the fully-packed case. This

predicted change of role from form drag to particle lift, with surface packing change, has not been systematically investigated.

3. Assuming that the turbulent flow event that most frequently initiates particle motion is known, how the stochastic flow field is linked to particle entrainment is not clear.

Of the questions listed above, the third one is addressed by Papanicolaou (1997). The incipient motion criterion based on the probability of particle entrainment was used to determine the experimental conditions for the present, and Papanicolaou's (1997) work. While, Papanicolaou's (1997) work assumed that a specific turbulent flow feature (a combination of instantaneous drag and lift force, discussed later) that caused the sediment motion was known, the present work attempted to establish the validity of such an assumption for the case of a single, exposed ball placed atop a rough, porous bed. Specifically, an attempt was made to establish a correspondence between sediment motion and specific turbulent velocity events, for a given bed configuration. This part of the experiment is referred to as the single ball experiment.

The second question in the above list is proposed as future work.

II-10 The Role of Turbulence in Particle Motion Initiation

The statistical nature of the entrainment problem was investigated, among others, by Naden (1987), Paola (1996), and Grass (1983). The probability density distribution of the instantaneous bed shear was considered the fluid dynamic parameter relevant to the initiation of particle motion and was hypothesized as a Gaussian (Grass, 1983) or a two-parameter

gamma (Paola, 1996) distribution. Naden (1987), modeled sediment initiation by considering the instantaneous fluid lift (F_L), and drag (F_D) forces balanced by the particle's immersed weight. Naden modeled F_L and F_D as (refer to Figures II-7a and II-7b for the direction of velocities in the flume coordinate system):

$$F_L = \frac{1}{2} C_L \rho A W^2 \quad \text{[II-3]}$$

and

$$F_D = \frac{1}{2} C_D \rho A U^2 \quad \text{[II-4]}$$

where C_L and C_D are the lift and drag coefficients, respectively, ρ , the fluid density, A , the projected area of the particle, and U and W are the instantaneous, stream-wise and normal velocity components, respectively.

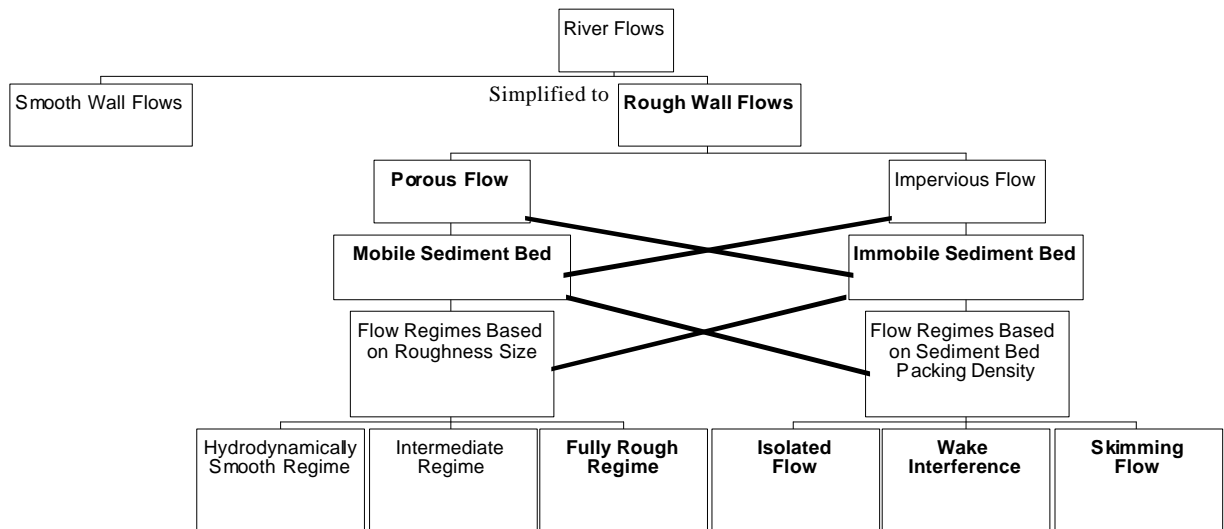
It should be noted that both F_L and F_D do not act at a single point on the particle, but rather have a time-dependent distribution across the projected area of the particle. This complex situation is much simplified by considering the “effective” F_D and F_L to act at a specified location of the particle. Table II-1 gives some of the recommended distances from the top of the bed at which the effective F_D appears to act. For the lift force, Einstein and El-Samni (1949) recommend that the velocity measured at $0.35d$ from the reference plane yielded a constant C_L value of 0.178 (for all the flow conditions they encountered). They did not find any physical reason for this observation. In order to simplify the problem, Naden (1987) assumed that the instantaneous W value was proportional to the U value ($W = 0.77U$). While such an assumption is reasonable for the root-mean-square values of U and

W (i.e. u' and w'), it is not so for the instantaneous ones. Based on the above simplifications, Naden reduced the balance of forces to a function of just U.

II·11 Flow Description and Measurement Techniques

For turbulent flows, since theoretical solutions can offer very little at present, experimental methods continue to be the backbone of turbulence research. Typically, complex natural turbulent flows are simplified and produced under controlled conditions in the laboratory. The simplification, such as the fully-developed uniform flow condition, helps to isolate different features of the turbulent flow and limits the dynamic processes which must be considered, thereby simplifying the fluid-solid interaction problem. Even for simplified rough wall flow situations experimental problems with traditional probes arise primarily due to measurement difficulties in and around roughness. Additional flow disturbances caused by the physical presence of the probe close to the roughness, will affect the experimental measurement accuracy, particularly in studies near the incipient flow condition. With the advent of non-intrusive measurement techniques such as laser Doppler anemometry (LDA), particle image velocimetry (PIV), laser induced fluorescence (LIF), and other optical techniques, the role of laboratory-based experiments in understanding the complex rough wall flows holds more promise than ever before. Such optical techniques have been used successfully before by several researchers (Grass, 1971 and 1993; Nelson, 1995; Smith and Metzler, 1983; Nezu and Rodi, 1983; Durst et al., 1981) in studying a wide variety of fluid flows. At this point, the objectives of this work are restated so that the importance and usefulness of the optical techniques discussed above are highlighted.

The objectives of this work are to investigate: (1) the turbulent event associated with particle movement for a single, exposed glass sphere placed atop a porous bed. Specifically, correlate velocity events measured at a single point immediately upstream of the ball with the ball motion, and (2) the nature of fluid-solid interaction for different sediment bed packing conditions. Using velocity profile measurements made at three specific locations, upstream, above and downstream of a ball analyze the extent of the roughness sublayer under the specified flow conditions. The facilities used to achieve the objectives are detailed next.



Note: Flow conditions for the present investigation indicated in **bold** letters.

Figure II.1. Categorization of wall-bounded flows.

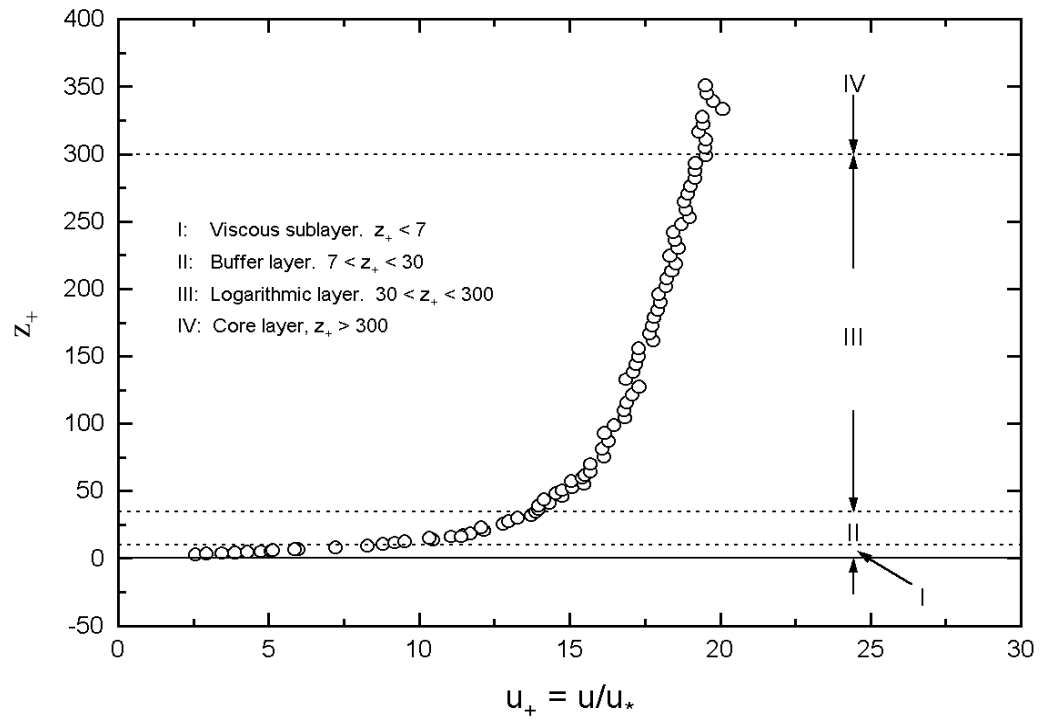


Figure II.2. Different regions in smooth wall flow.

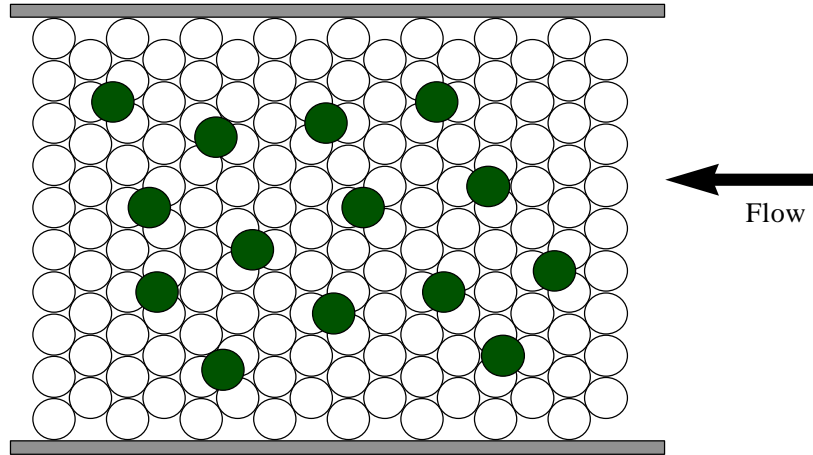
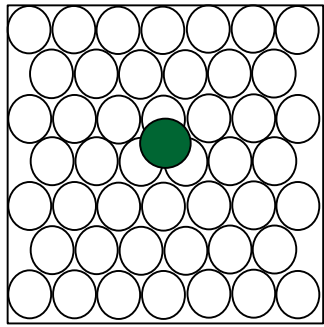
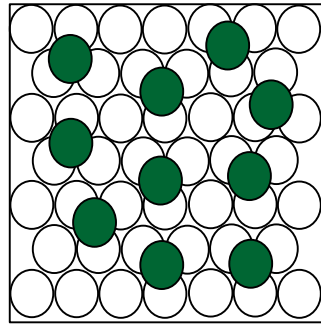


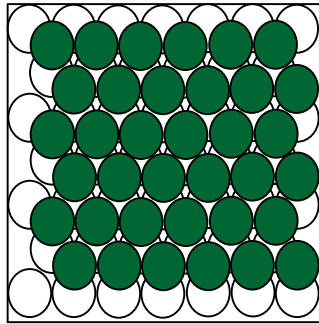
Figure II-3. Packing density concept. The figure shows 7 % packing density.



Isolated Ball Regime



Wake Flow Regime



Skimming Flow Regime

Figure II.4. Three regions of rough wall flow based on packing density (Morris, 1955).

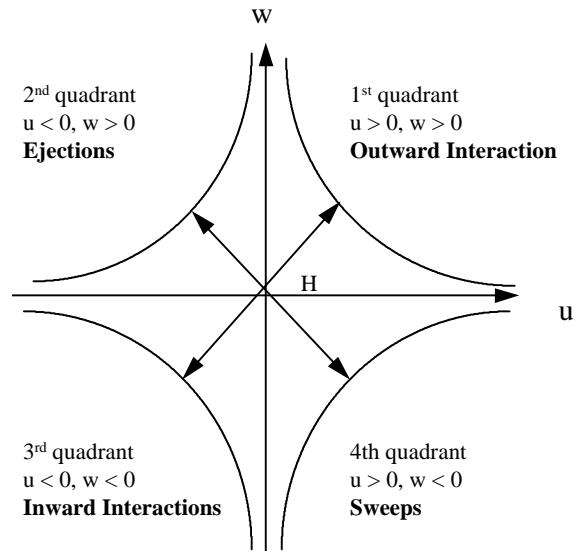


Figure II.5. Four quadrants in the uw -plane.

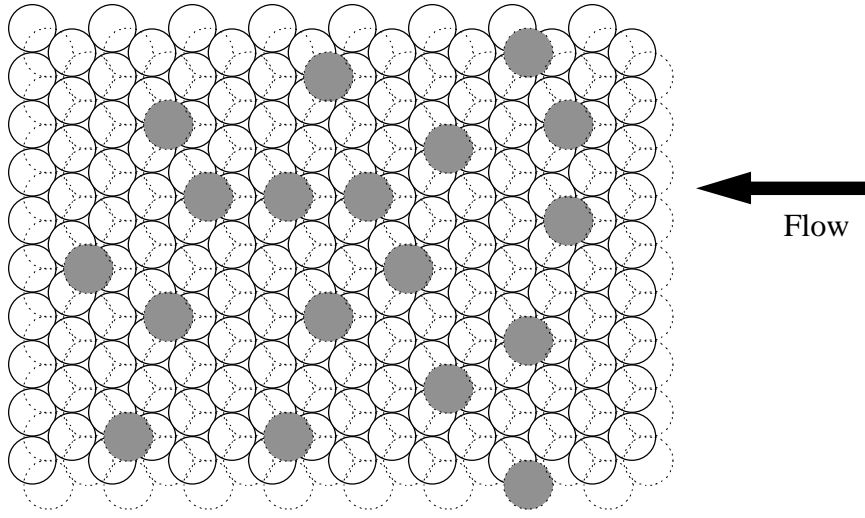


Figure II-6. Plan view of an incompletely packed bed. The dotted lines denote vacant spots.

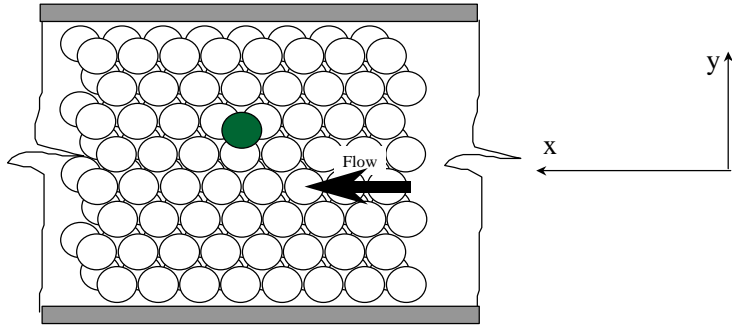


Figure II-7a. Single, exposed ball atop a porous bed, plan view.

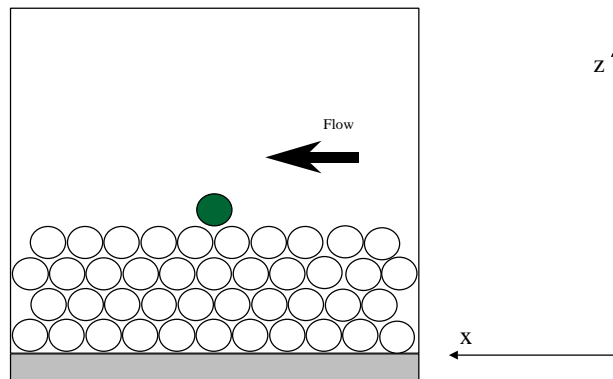


Figure II-7b. Single, exposed ball atop a porous bed, side view.

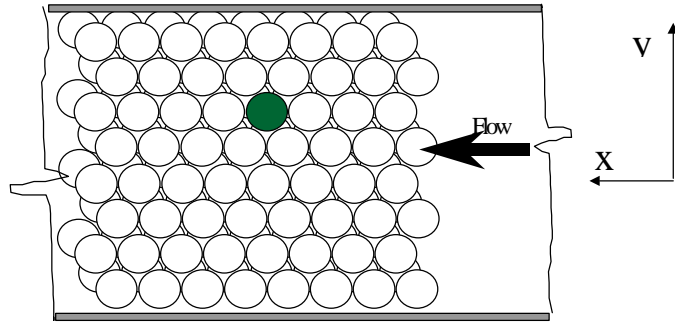


Figure II-8a. Fully-Packed bed, plan view.

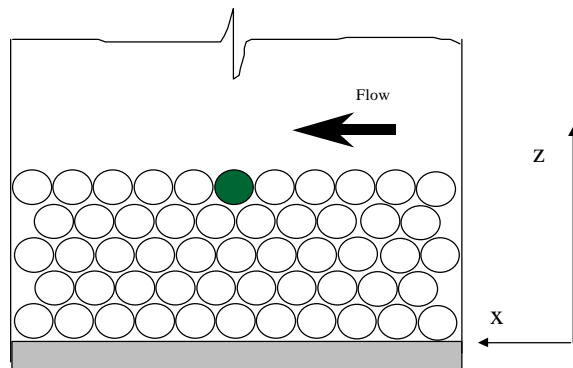


Figure II-8b. Fully-Packed bed, side view.

Table II.1. Height above bed[†] at which the effective drag force, F_D , acts (see, Bridge and Bennett, 1992).

Value	Source
0.35d	Einstein and El-Samni (1949)
0.7d	Chepil (1959)
0.63d	Egiazaroff (1965)
0.5d	Ikeda (1982); Weiberg and Smith (1985, 1987)
0.6d	van Rijn (1984); Komar and Li (1988)
0.57d	Naden (1987)

[†] The distance at which the net drag acts cannot be evaluated accurately, as the location of the reference plane itself is not known. The reference plane distance below bed must be added to the values shown Table II-1 to get the distance from the reference plane.

Chapter III

Experimental Facilities

III.1 Basic Facilities

The experimental facilities used in this study can be divided into three major parts: (1) the flume facility, (2) the laser Doppler system, and (3) the video camera system. Each is described in the following sections.

III.2 Flume

The experimental investigation was carried out in a tilting, Plexiglas-walled flume of rectangular cross section. The flume is 20.5 m long, 0.6 m wide, and 0.3 m deep, with a useful length of 14.5 m. The flume has a 11.3-m³ tank at the downstream end. Two centrifugal pumps facilitate re-circulation of the tank water through the flume. Both pumps are rated at 7.5 hp, closed-impeller type, powered by individual 3 phase, air-cooled motors. One of the centrifugal pumps is equipped with an externally located, user-adjustable, variable-frequency speed controller (Toshiba, Tosvert-130H1), while the second pump runs at a fixed speed. Peak discharge of both the pumps are equal. The clearance between the impeller and the casing in the two pumps is about 0.75 inch, thus, both units are designed to handle sediments up to 0.75-inch size, although no sediment was recirculated in this

investigation. The outlet line from both the pumps join a 8 inch diameter water supply line, located underneath the flume main body. The supply pipe runs the entire length of the flume and ends at the entrance. A venturi located in the 8-inch diameter water pipe, and connected to water and mercury manometers, enables flow rate measurements to within $\pm 2\%$. A knife-edge gate valve, located downstream of the venturi serves as an additional flow-control device. The gate valve is vital, especially for high flow rates, as it enables gradual, controlled filling of the flume and helps prevent the initial surge of water from dislocating the entrainable sediment and disrupting the experiment. Figure III-1 shows a picture of the flume. Figure III-2 shows the schematic of the flume that identifies major flume features.

The downstream end of the flume has a motorized, adjustable gate, which was made inoperative during all of the experiments. A modified gate arrangement, that produced much better uniform-flow depth condition, was used in this study. This gate arrangement will be discussed later. The flume also is equipped with a sediment trap, a 1/2-hp sediment return pump with a rubber impeller, a volumetric sediment feeding tank, and associated piping. Since the sediment handling circuit was not used in the present experiments, it will not be discussed further.

The entire flume can be tilted about its downstream end, with the help of a 50-hp motor, and gear boxes with non-slip, chain drives. The range of flume slope is from -1 % to 5 % and can be read from a scale attached to the flume. Careful calibration of the flume slope, performed before the start of the experiments, and repeated again before the single ball experiment, will be outlined later.

III.3 Laser Doppler System

Laser Doppler velocimetry, commonly called LDV, is a non-intrusive, optical technique, that is employed in measuring flow velocities. The non-intrusive nature is particularly beneficial in rough wall studies, as measurement uncertainty caused by probe interference is completely eliminated. In addition, LDV does not require calibration, is linear (measured Doppler frequency is directly proportional to the flow velocity), is sensitive only to the fluid velocity, and is completely insensitive to changes in fluid properties such as temperature and pressure. LDV systems are especially valuable for flow measurements in corrosive or high temperature environments, re-circulating and rough wall flows, restricted or confined spaces. Furthermore, LDV has excellent temporal and spatial resolution.

The flow measurements were obtained using a three-component, three-color, six-beam, frequency-shifted, non-orthogonally oriented laser Doppler velocimetry system, operating in an off-axis, back-scatter data acquisition mode. The entire laser system is mounted on a traverse table (TSI, Model 9500), that can be moved in three orthogonal directions by individual stepper motors. The specified accuracy and repeatability of spatial positioning of the traverse table is ± 2.5 microns¹. A coordinate displayer (Sony, Magnescale, LM22S-32R) shows the table's position with respect to an arbitrary origin. The main laser beam is split into its constituent colors by a prism, and the three most powerful beams are selected to effect the velocity measurements. The colors, in decreasing order of power, are green (514.5 nm), blue (488 nm) and violet (478.5 nm). The blue and green color beams form one optical axis and the violet forms the other. Each of the three

¹ 1 micron = 10^{-6} m = 1 μ m

color beams is split into two by a beam splitter (thus, a total of six beams), and one of the split beams of each color is frequency shifted (TSI, Model 9186A). The advantages of beam splitting are discussed later. Figure III-3 shows the laser system used in this study. The optical train of the laser system consists of, polarizers, beam splitters, collimator, prisms, mirrors, frequency shifter assemblies, beam displacer, beam stops, steering modules, lenses, beam expanders, and photo multiplier tubes. Each of these components, their purpose and basic principles of LDV operation are included in Appendix A-1.

III-4 Video Camera

The video camera was employed for two purposes. First, it provided particle movement information in the five packing density cases. The particle movement information was essential in determining the hydraulic conditions that represented the incipient conditions for the different sediment bed packing density cases.

Second, the video camera was employed in the single ball experiment. The main goal of the single ball experiment was to correlate turbulent velocity events with the motion of a single glass ball placed atop the porous bed. A counter placed within the camera field of view, displayed the most recent validated LDV data, while simultaneously, the camera monitored the ball motion. The preparatory work associated with the single ball and sediment packing density experiments is discussed in the next chapter.



Figure III.1. Photograph of the flume

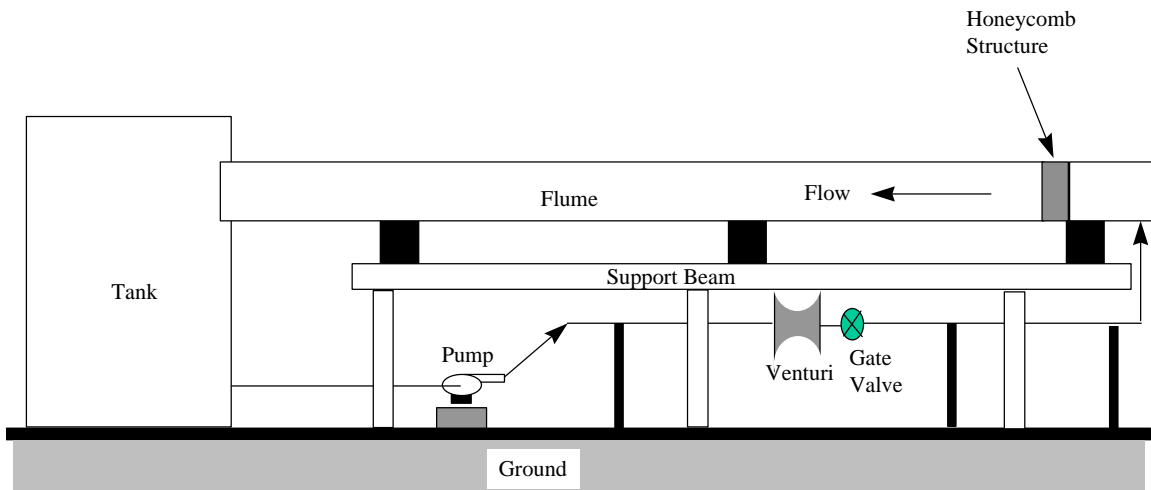


Figure III-2. Schematic of the flume.

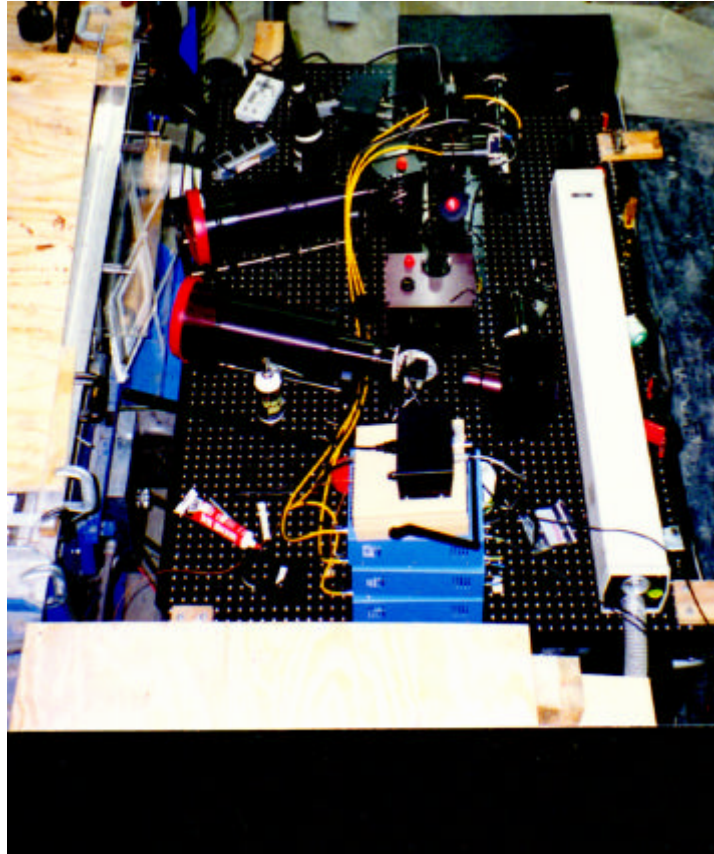


Figure III-3. The LDV system.

Chapter IV

Preparatory Work

IV·1 Introduction

The preparatory work discussed in this chapter includes a discussion on the modifications that were effected to the experimental facilities described in Chapter III, and roughness selection and distribution in the flume. Experimental setup and the preparatory work for the single ball case is discussed separately, followed finally by a discussion on post-processing of the LDV data.

IV·2 Flume Preparatory Work

The flume preparatory work for the present experiments included the flume slope calibration, establishing uniform flow depth using a modified gate arrangement, rough particle selection for the porous bed, its distribution, and test section location.

IV·2·1 Flume Slope Calibration

Determination of the flume slope with good accuracy is important for establishing uniform, fully-developed flow. Also, the accuracy of the determination of the friction velocity, u_* , given by $(gHs)^{1/2}$ (see, for example, Roberson and Crowe, 1985), depends on the flume slope, s , in addition to g , the acceleration due to gravity, and H , the water depth.

Accurate determination of u_* is important, as it is employed as a scaling parameter for normalizing flow variables.

The slope of the flume was calibrated twice during the experiments, once before the start, and again before the single-ball experiment. The calibration was carried out using a precision leveling instrument. Measurements were effected at seven equi-spaced (eight feet apart) locations along the entire length of the flume. At each of these locations, three slope measurements were made across the span of the flume. The slope readings were taken at least four times at each location, and an average was used in estimating the flume slope. The specified accuracy of the leveling instrument was 0.006° [$\tan^{-1}(10^{-4})$] and the maximum deviation of the slope from that at the test section was found to be within 10 per cent.

After careful calibration of the flume slope, rough particles were distributed over the plexiglass smooth wall. The selection, and distribution of the roughness are addressed next.

IV·2·2 Rough Particle Selection

Sediment particle selection was such that the fully-rough case criteria ($Re_p > 70$, see Chapter II) was met. Glass spheres of uniform diameter were chosen as the bed material. The diameter of the spherical particles was chosen so that the nondimensional threshold stress, based upon Shields (1936) criterion and later modified by Vanoni (1975), was independent of the particle's Reynolds number, Re_p (see Figure IV·1). Thus,

$$\frac{d}{n} \sqrt{0.1Rgd} \geq 500 \quad [\text{IV}\cdot\mathbf{1}]$$

where d is the particle diameter, ν , the fluid kinematic viscosity, $R \equiv \frac{\rho_s}{\rho} - 1$, the submerged mass of the particle per unit volume, ρ_s and ρ are the particle and fluid density, respectively, and g , the acceleration due to gravity. While Equation IV-1 determines the lower limit of the particle size, the relative depth ratio, H/d , determines the upper limit. The relative ratio is set such that particle is not too large for the water depth, H . To meet this criteria, H/d is typically set greater than or equal to 3 (Bettess, 1984).

In open channel flows the greater the flow depth, the more pronounced is the secondary flow produced by the flume side walls. The maximum allowable depth, H_{\max} , depends on the width, W , of the flume, so that secondary flows induced by the side wall of the flume wall do not penetrate to the centerline of the flume. The ratio of W/H (W is the flume width, and H , the flow depth) was limited to 6 (Nezu and Nakagawa, 1993) so that the side-wall generated recirculatory flow was confined to about 10 cm from the side wall. Based on the above restrictions, and commercial availability, the particle diameter was chosen to be 8 mm (see also, Papanicolaou, 1997).

The length scales of the turbulence in comparison to the sediment size may be of interest here. In Chapter II, the role of the Reynolds shear stress in sediment motion initiation was discussed. The length and time scales associated with the bursting process that is responsible for the production of Reynolds shear stress have been studied in detail for smooth wall flows. Similar studies for rough wall flows are difficult, and inconclusive (Nezu and Nakagawa, 1993). Grass (1971) suggested that the turbulent bursts in rough wall flows scaled with the roughness size. Notwithstanding the fact that the turbulence production mechanisms in smooth and rough wall are suspected to be different (e.g., Grass, 1971; and,

Nakagawa and Nezu, 1977), *as a first approximation*, the length scales associated with the bursting process, estimated based on the smooth wall investigation (see Nezu and Nakagawa, 1993) results, are provided in Table IV-1.

IV-2-3 Test Section Location

The test section is located about 11.4 m downstream of the flume inlet. To ensure the fully-developed flow condition in rough wall flows, Nezu and Nakagawa (1986) recommend, $x \geq 180R_h$, where x is the channel length required to achieve fully-developed condition, and R_h is the hydraulic radius, defined as A/P , where, A is the area of cross section of the flow, and P is the wetted perimeter. Table IV-2 summarizes the development length required for different flow conditions encountered in this work. The calculations provided in Table IV-2 are for smooth wall, and for rough walls the development length is likely to be shorter (Antonia and Luxton, 1971 and 1972).

IV-2-4 Distribution of Particles

Naturally worn gravel ($d_{50} = 7/8$ inch, where d_{50} is the diameter of the sieve hole that can pass 50 % of the gravel) was placed in the first 10.4 m of the flume, such that the top of the gravel surface was nearly 2.9 cm thick, as measured from the plexiglass bottom surface of the flume channel. To ensure uniform height of the gravel roughness layer, a leveling screed, attached to a movable trolley, was used. The flume has guides, along which the trolley could be rolled. The screed, a rigid metal plate, was positioned approximately 2.9 cm from the smooth wall, and attached securely to the trolley. The width of the screed is slightly less than that of the flume. By moving the trolley along the guides, the roughness

particles were roughly leveled. The step was repeated several times, and local ‘bald’ patches were filled with additional roughness particles, and leveled. The final packing was done by hand using a flat wooden surface. Local packing to fill up bald patches accompanied the last step.

Spherical balls were placed in the remaining length of the flume following the gravel section. The number of balls required to fill four layers over a specified area was calculated. The calculated number of balls were distributed to form the four layers. The finishing process involved gentle rolling of the balls, so that they packed as tightly as possible. An appropriately packed bed of spheres felt tight to the hand, and the 4th layer particles did not yield and move easily to small loads. An improperly packed bed of spheres would shift during the experiment, altering the angle of repose (refer to Figure IV·2), such that motion of the 5th layer particles became very much rarer. In other words, proper packing is imperative to ensure good and repeatable test results.

After the gravel section, three layers of glass balls were tightly packed in the remaining 4 m of flume length. The fourth layer at the gravel-ball junction comprised lead balls (at a mean diameter of 0.33 inch, the lead balls are about 4% bigger than the glass balls). The presence of lead prevented possible erosion and movement of fourth layer balls at the gravel-ball transition. Lead balls were placed on the fourth layer for a length of approximately 2 m from the end of the gravel section. The fourth layer of the final stretch of the flume, which included the test section, comprised entirely the 8-mm glass balls. Figure IV·3 illustrates the distribution of the roughness particles.

For identifying sediment motion through image analysis (Papanicolaou, 1997), the entrainable glass particles were painted green. The green-colored particles were placed atop

the 4th layer to form a 5th layer of mobile sediment, and their movement, over a specified area, was then recorded with the use of the video camera. The entrainable particles were painted so that the image analysis program could distinguish the moving particles from the immobile (4th layer) background more easily.

However, single-point velocity measurements around roughness particles, require an immobile bed, as bed mobility alters the local flow conditions and interrupts LDV data acquisition. This problem was overcome by splitting the experiment into two parts. For extracting bed mobility information using the video imaging, the green-colored glass balls were used, and for velocity profile measurements in close proximity to the 5th layer sediment, lead balls were used in the same configuration, so that the geometrical features of the 5th layer were retained, but with no particle mobility. This is equivalent to freezing the bed morphology so that single point profile measurements could be completed. The number of lead (or glass) balls placed on the 5th layer varied for the different sediment bed packing cases, and are summarized in Table IV-3. The results presented in this work include measurements taken over the immobile bed with lead balls placed in the 5th layer. Part of the experimental measurements from this work were used by Papanicolaou (1997), who attempted to establish an incipient motion criteria for 8-mm glass balls using a stochastic approach.

The last 0.2 m of the flume, was covered by a 0.6m-wide plexiglass plate, that allowed seepage flow to proceed underneath it. The purpose of the plexiglass plate is to prevent erosion effects at the flume exit. Figure IV-4 shows the details of the end plexiglass plate mounting.

IV·2·5 Modified Gate Arrangement

A modified downstream flume gate setup, shown in Figure IV·5, was employed in this work. The downstream section of the flume has a motorized gate, which moves vertically to adjust the flow depth. The gate movement is guided by a rectangular notch cut on both sides of the flume wall. The motorized gate was lowered so that it was flush with the bottom wall, and two 0.25-inch diameter rods, about 1.5-inch long were placed in the notch on each side of the flume and were used as props. Rods and flats of different sizes, resting on the props, were employed as gates spanning the width of the flume and adjusting the flow resistance and depth. The number and size of the rods and flats required to produce uniform flow depend on the flow conditions and were determined by trial and error. The modified gate arrangement produced uniform flow conditions nearly throughout the entire length of the flume, freely allowing seepage flow to reach the tank, and the entrained sediment to reach the collection basket placed at the flume exit.

IV·3 Camera Setup

The video camera was used for two purposes. First, it provided visual information about roughness particle movement over a defined area (see, Papanicolaou, 1997, for details), and second, it helped monitor the movement of a single glass ball. The experimental arrangement of the camera for the single ball case is outlined first.

For the single ball experiment, a Sony (Model CCDF501C) 8-mm camcorder, with a filming rate of 30 frames per second, was used. The camera was positioned 1.02 m from the downstream end of the flume. Other relevant distances of the camera are shown in Figure IV·6. A mirror, placed in the camera view, reflected the display window of a pulse counter

(not the LDV system frequency counter) that showed the LDV data number. Whenever data is validated, a digital pulse is sent to the computer from the frequency counter. Simultaneously, the same pulse is sent to the counter. On receiving the pulse the counter cumulatively updates its number display by 1. Therefore, the pulse counter displays at any instant the current LDV data count. In this manner the current LDV data count is imaged on the video record for later correlation of the LDV measurements with sediment motion.

The area of coverage of the camera was about 0.12 m x 0.12 m (covering a square area of about 15 ball diameters per side). A high-intensity quartz halogen lamp (DVY GE 650W), appropriately positioned, helped illuminate the sediment bed.

The camera setup for the packing density case was quite similar to the single ball case except that there was no mirror or pulse counter. Two halogen lights were employed and the area of coverage was approximately 28 x 30 cm². For more details about the camera setup, reader is directed to Papanicolaou's (1997) work.

IV.4 Flow Seeding for LDV Measurements

First, the LDV preparatory work is addressed. LDV measurements are effected by "seeds" or "impurities" that are either artificially added to or are naturally present in the fluid. In other words, LDV measures the velocity of the seed particles and not of the fluid molecules themselves. Appendix A-1 includes a more detailed discussion of the role of the seed particles in LDV measurements.

Proper selection of seed material for LDV measurements is very important, as the seed determines not only the quality of signal, but also affects the accuracy of the flow velocity measurement. In the present work Silicon Carbide (SiC) was used as the seed

material. SiC has a high refractive index ($\mu = 2.65$), is about 3.2 times as dense as water, and is a popular seed choice for LDV measurements in water (Laser Velocimetry Systems, 1986; Menon and Lai, 1991).

Different sizes of SiC particles (1, 4, 10, 20, and 50 micron) were investigated to see the effect of seed size on data rate and signal quality. Titanium dioxide powder was also used on a trial basis. The four-micron diameter ($4 \mu\text{m}$) SiC seed, which produced the best quality signal and data rate, was chosen as the seed material.

The ability of the seed material to closely follow the flow is characterized by its aerodynamic diameter. The aerodynamic diameter of a particle is defined as the diameter of a unit-density sphere that has the same settling velocity as the particle under consideration. The aerodynamic diameter depends on the particle size, shape, and its density. The relaxation time, τ (time it takes for the particle to approach the fluid velocity), of the particle is given by (Laser Velocimetry Systems, 1986):

$$\tau \cong \frac{\rho_p d_p^2}{18\mu} \quad \text{[IV-2]}$$

where d_p is the particle (seed) aerodynamic diameter, ρ_p , the seed density, ρ and μ , the fluid density, and absolute viscosity, respectively. For a $4 \mu\text{m}$ diameter, spherical SiC seed, Equation IV-2 yields $\tau = 2 \mu\text{s}$, using a μ value for water at 20°C . Following the procedure outlined in Laser Velocimetry Systems (1986) the $4 \mu\text{m}$ SiC seed can be estimated to track a flow frequency up to 65 kHz. The expected frequency of the flow is estimated to be less than 1 kHz.

The SiC seed is introduced into the flume as follows. The seed is mixed with water and fed from a bucket positioned about 18 inches above the water free surface through a

0.25-inch aluminum tube. The seed outlet tube is positioned nearly 500 tube-diameters upstream of the LDV measurement volume. The flow rate through the tube was approximately 3 gallons per hour, with the average discharge velocity being 0.2 m/sec at the discharge end. After about 5-6 buckets of the seed-filled water, additional seed was typically not required. In fact, most the experimental runs reported in this work did not require injection of seed, as the presence of previously injected seed material was sufficient.

IV-4-1 Optical Window for the LDV System

Since the velocity measurements are required to be made in water, the current work mandates that the LDV measurement volume be in water. When LDV beams enter from air to water, adverse refraction effects can make overlapping of the six beams very difficult. To limit the refraction effects for both the incident and scattered beams, a specially-constructed, adjustable water box (Lindsay and Owsenek, 1993) was used. The water box, made of plexiglass, and sealed to the flume side wall using putty, was rigidly attached to the LDV traverse table. To facilitate the motion of the box with the traverse table, it was provided with rubber bellows, that allowed approximately an inch of movement in each of the three traverse directions. The plexiglass sides of the water box were normal to the incident laser beams, so that refraction effects were minimized. The laser beams then entered water in the box, and again through the flume side wall to water in the flume. When the LDV traverse table was moved, the rigidly attached water box moved with it, maintaining its relative position with respect to the incident laser beams. Figure IV-7 illustrates the optical window setup.

To facilitate measurements close to the roughness elements, the LDV traverse table was tilted about the x-axis of the flume (refer to Figures II·7a and II·7b for the coordinate system), making 3.8° with the y-plane of the flume (see Figure IV·8 for LDV tilt). The angle between the bisectors of the two optical axes (blue-green and violet) is about 30° . Thus, the velocity measurements were made in a non-orthogonal coordinate system, and required transformation to the flume coordinate system. This transformation was effected during the post processing of data.

IV·4·2 LDV Data Post-Processing

The validated LDV data signals that are stored in the computer are in machine readable form (raw). The data acquisition and storage are accomplished by the commercial software package, FIND, Flow Information Display Software, developed by TSI, Inc. FIND runs in the DOS (Disk Operating System, IBM) environment. FIND also can compute the flow statistics, although this feature was not utilized in this study.

Conversion to human-readable form (ASCII) from the 'raw' file was effected using the program that again was developed and provided by TSI, Inc. This program did not run in batch mode, and batch-mode operation was achieved by constructing a DOS batch file program. The DOS batch file was generated by using a FORTRAN program (written for a Watfor77 compiler) developed in-house. The data in the ASCII files are not in flume coordinates. To convert from beam to flume coordinates required a coordinate transformation. All the programs that effected the coordinate transformation and facilitated further data analysis were developed in-house. These are further explained below.

A FORTRAN program (again written for a Watfor77 compiler) was developed to transform the data from the LDV beam coordinate system to flume coordinates. This program also corrected the mean statistics for velocity bias (discussed in the appendix). The program runs in batch mode and outputs both average fluid quantities such as the velocities, rms quantities, and the Reynolds shear stresses, as well as the instantaneous velocities. This program (Menu3d) required the coordinate transformation matrix values as input. This matrix was obtained separately by solving the appropriate transformation equations (Ldageor) using TKSolver software. The output data of Menu3d that contained the instantaneous velocity details was used for any subsequent analyses (such as the quadrant analysis, Willmarth and Lu, 1972, and probability density distributions, Nezu and Nakagawa, 1993 of various parameters).

Furthermore, programs that clean the ‘noise’ in the experimental data based on some specified statistical criteria, were also developed. The WATFOR program, Looper.for, used a criteria based on the joint probability density distribution of two measured velocity components for data cleaning. In addition to the above, specific programs for analyzing the LDV data associated with the single ball experiment were developed. Details will be discussed in the next chapter.

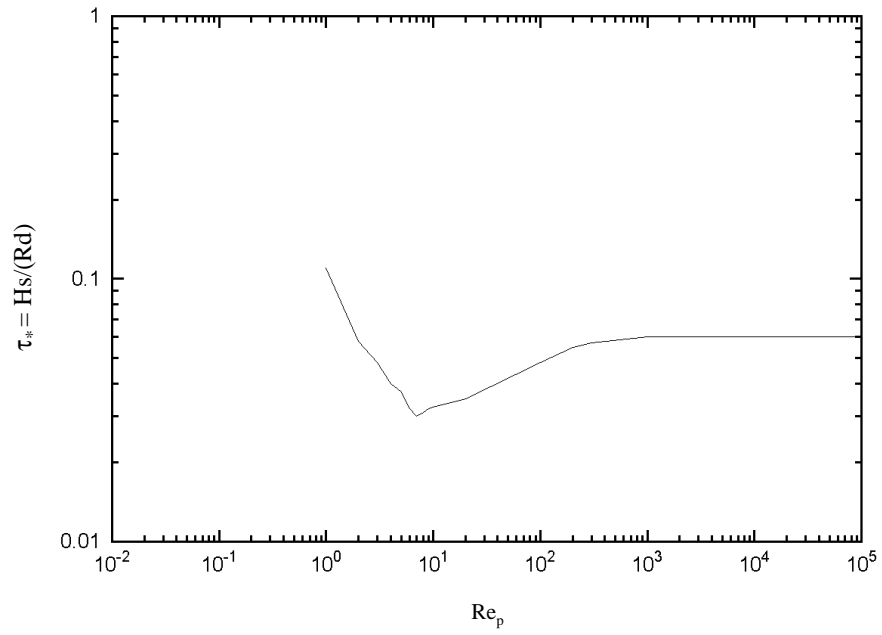


Figure IV.1. Variation of the non-dimensional bed shear stress, τ_* , with particle's Reynolds number, Re_p .

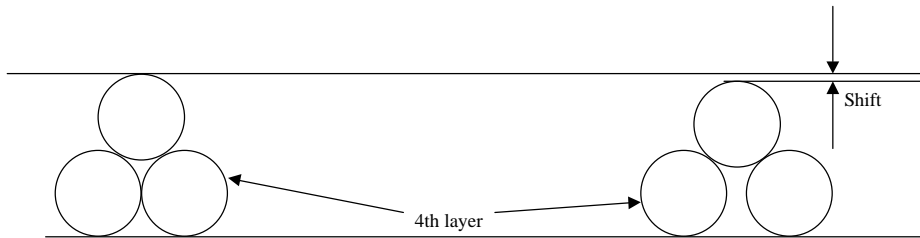


Figure IV.2. Angle of repose change due to shift of the 4th layer balls.

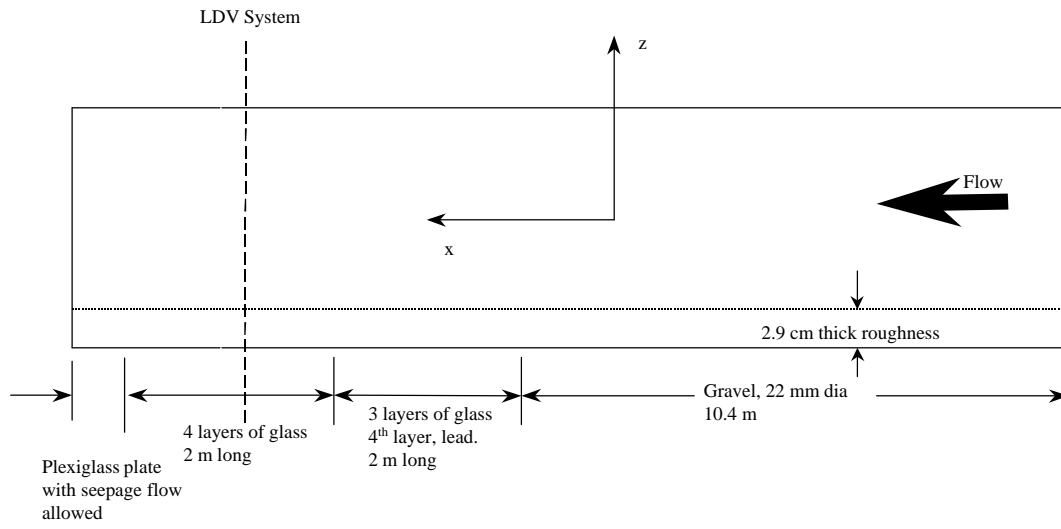


Figure IV.3. Distribution of roughness particles in the flume.

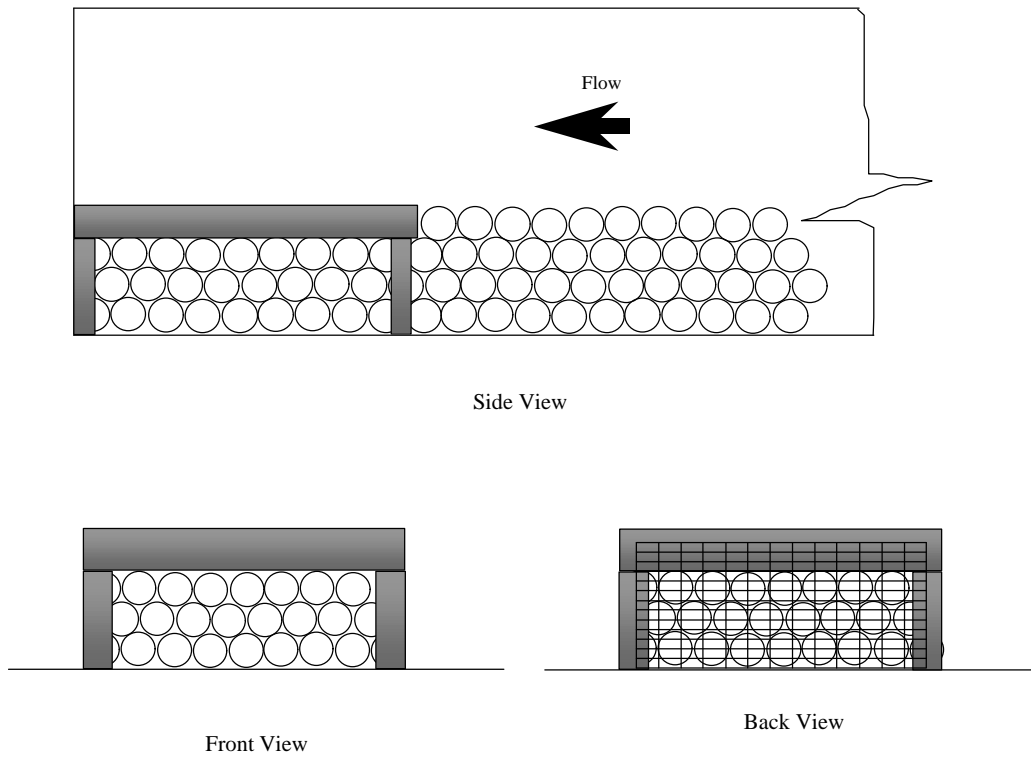


Figure IV.4. End plexiglass plate arrangement at flume exit.

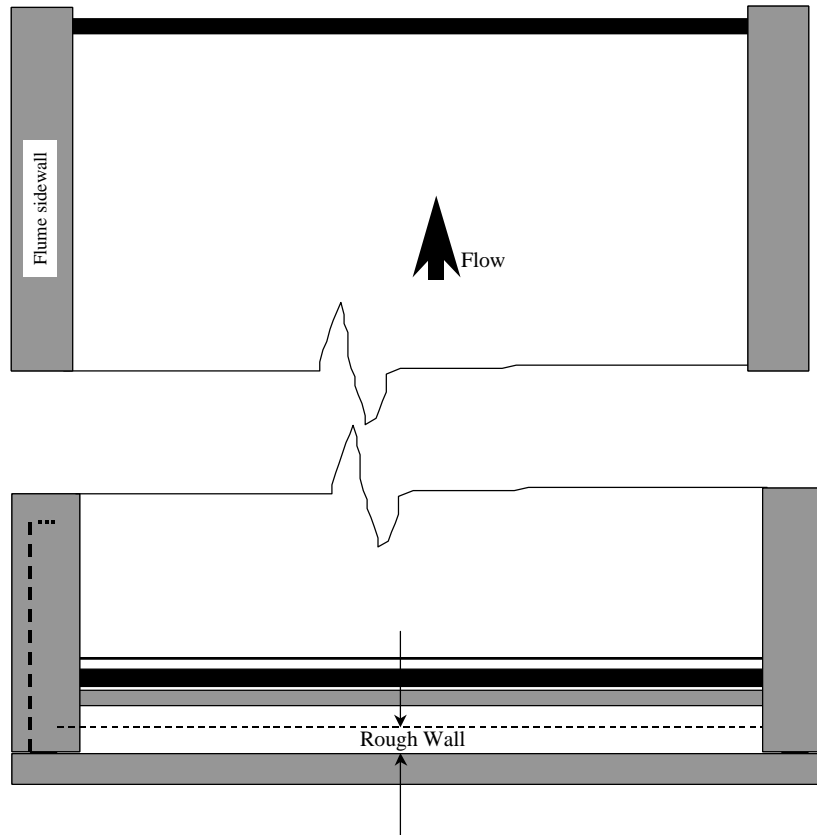
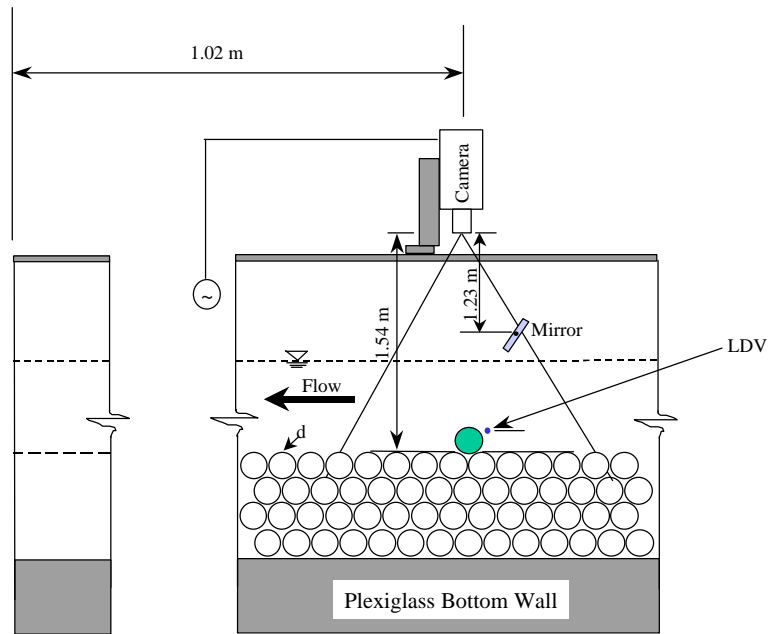


Figure IV-5. Schematic of the modified gate arrangement.



Note: Figure not to scale

Figure IV.6. Camera arrangement for the single ball experiment.

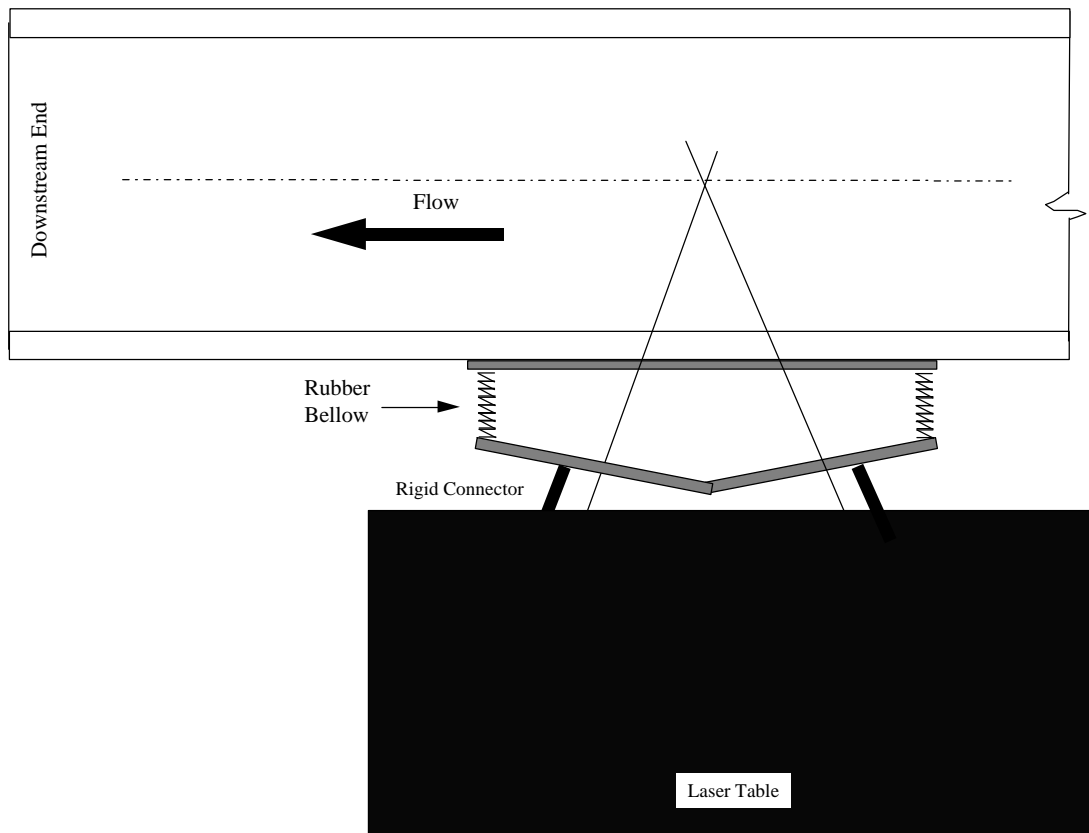


Figure IV-7. Optical window setup for the LDV system.

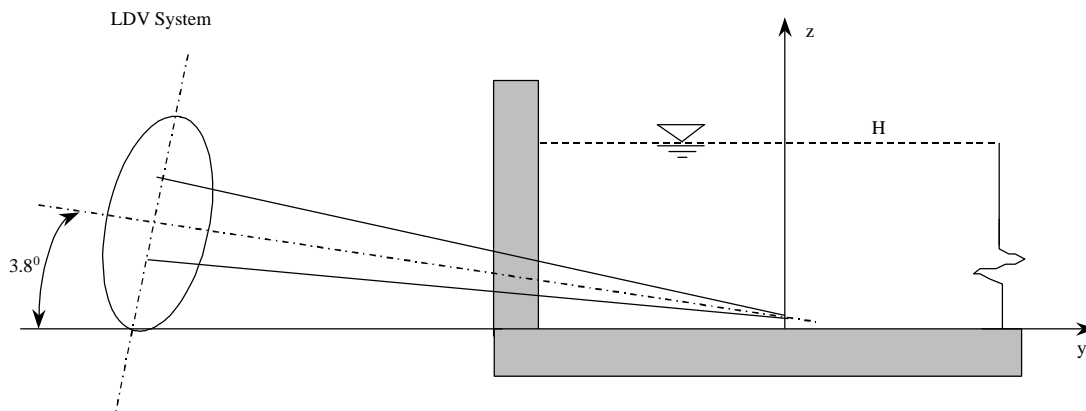


Figure IV-8. Tilt of the LDV system.

Table IV.1. Different length scales of the conceptual model of the bursting cycle (after Wallace, 1985)[†]

Packing	Friction Velocity u_* m/s	Viscous Length $v_l = \nu/u_*$ μm	Length of Burst $L_b = 1000v_l$ mm	Vortex Diameter $v_d = 35 v_l$ mm	Distance between Legs $L_l = 55 v_l$ mm	Spanwise Spacing $\lambda_z = 100v_l$ mm	Length of Head $L_H = 250 v_l$ μm	Life Time of Bursts $T = 500 \nu / u_*^2$ sec
2	0.0313	34.5	34.5	1.2	1.9	3.45	8.63	0.552
20	0.036	30	30	1.05	1.65	3	7.5	0.417
35	0.067	16.1	16.1	0.56	0.89	1.61	4	0.12
50	0.075	14.4	14.4	0.5	0.79	1.44	3.6	0.096
70	0.093	11.6	11.6	0.41	0.64	1.16	2.9	0.062
1 ball	0.0313	34.5	34.5	1.2	1.9	3.45	8.63	0.552

[†] All calculations of length scales based on smooth wall investigations
Smooth wall flow visualization through hydrogen bubbles by Smith and Metzler, 1983. They found some streaks to persist five times longer than the values shown in the table above.

Table IV.2. Channel length requirement for fully-developed smooth wall flow.

Packing Density (%)	H ^(†) (cm)	$R_h = \frac{wh}{w+2h}$ ^(†) (cm)	$x \geq 180 R_h$ (m)
2	5	4.3	8
20	6.8	5.54	10
35	5.7	4.8	9
50	5.7	4.8	9
70	7.6	6.1	11
Single Ball	5	4.3	8

(†) Height measured from top of the porous bed.

(†) The flume width, w, is 60 cm.

Table IV.3. Number of spheres for different sediment bed packing conditions.

Surface Packing, %	Number of spherical particles
2	788
20	7886
35	13801
50	19716
70	27610

Chapter V

Experimental Procedure and Data Analysis

V-1 Introduction

In this chapter the experimental procedure and the data analysis are described. The experimental procedure details the steps followed and the precautions taken in conducting the tests, while the data analysis details methodology and the post-processing of the data.

To recapitulate, in this work two different experiments, viz., the single ball and five sediment bed packing tests, were carried out. The objective of the single ball test was to correlate fluid velocity events measured upstream of the single isolated glass ball with the dislodgment of the ball. For this purpose LDV measurements at a single location upstream of the ball were performed with simultaneous video imaging of the particle motion.

The objective of the five packing tests was to investigate the nature of fluid-solid interaction at flow conditions that produced sediment incipient motion. This interaction was investigated through LDV measurements at three specific streamwise locations, in front of, above and downstream of an individual roughness element for every packing condition. At each of the three locations velocity measurements were carried out at different points lying on a line normal to the rough bottom wall.

At the beginning of this chapter the steps followed for establishing the flow conditions for both of these experiments are described. Following this, the chapter is divided into two sections. The first section, Section V·A contains details of the experimental procedure and data analysis for the single ball case, while the second section, Section V·B, contains corresponding details for the five packing density cases.

V·2 Basis for the Determination of Flow Conditions

The flow or hydraulic conditions of the experiments carried out in this work were determined by using a stochastic concept that uses the probability of sediment entrainment as the criterion for “incipient” motion. Using this criterion, all experiments were carried out at this incipient motion condition. This is further explained at length below.

The sediment transport rate is traditionally defined based on the number of particles that cross a line within a specified time. Typically “crossing a line” translates to the amount of sediment collected at the sediment trap (with the flume exit defined as the “line”). Traditionally, for the determination of the incipient motion condition, the sediment transport rate, measured under varied flow conditions, is linearly extrapolated to zero and the value of the mean bed shear stress at “zero” transport rate defines the incipient stress (e.g., Shields, 1936; Paintal, 1971). However, several researchers (e.g., Fenton and Abbott, 1977; Vanoni, 1964) have observed that, sometimes, the relatively small amount of material collected at the sediment trap does not correspond well with the greater movement of sediment observed to occur sporadically over the test area. In other words, the number of particles that are “displaced” is greater than that collected at the trap. Thus, incipient conditions based on the

amount of sediment collected at the trap may tend to underestimate how active the sediment bed really is.

An incipient motion criterion based upon sediment displacement is proposed here. A criterion based upon sediment displacement would be the one that takes into account how “active” the sediment bed is. Thus, sediment motion need not cross a specified line to be counted as a valid movement; any observably small sediment motion is considered as a valid motion. Implementation of this method -- effected through video photography and state-of-the-art image processing techniques (see also, Papanicolaou, 1997) -- is explained further below.

Although the number of sediment particle displacements over an area (rather than physical transport across a line) is more descriptive of a mobile sediment bed, the “incipient” flow condition cannot be simply defined by the number of particles displaced per unit area per unit time. This is inadequate since, for the same flow conditions, more displacements per unit time per unit area can be created by simply increasing the concentration of the sediment particles on the bed. Actually the behavior is much more complex, as an increase in sediment concentration beyond a certain point may alter the boundary resistance characteristics as discussed by Morris, 1955. In other words, for a specified flow condition, increasing the sediment concentration may not always lead to more “active” bed. At high sediment concentrations (beyond some limiting value) the sediment movement may be inhibited. For simplicity, the scenario where an increase in sediment concentration leads to a more active bed is considered here. Thus, given the above situation, the fraction of available particles that are displaced per unit time is a better variable than the number of displaced

sediment particles, as it takes into account the concentration or “availability” of entrainable sediment particles.

The fractional rate of sediment displacement can be defined as follows. Consider an area A, that has a total number of roughness elements, N_T , that are available to move, of which N_D number of elements are displaced in the j^{th} time interval, Δt_j , of an extended experiment of duration, T. The fraction of all balls displaced in the specified time interval, thus, is given by N_D/N_T . The average fractional frequency of ball displacement, f_j , within the specified time interval is then,

$$f_j = \frac{N_D}{N_T} \frac{1}{\Delta t_j} \quad [\mathbf{V}\cdot\mathbf{1}]$$

If the fractional frequency measurements are repeated for m time intervals, then, an average fractional frequency rate can be computed as,

$$f_{\text{avg}} = \langle f_j \rangle = \frac{\sum_{j=1}^m f_j}{m} \quad [\mathbf{V}\cdot\mathbf{2}]$$

The frequency of ball motion is the result of the randomly varying turbulent fluid force exerted on the particles. If specific fluid events (for example, turbulent bursts) are believed to initiate ball motion, then the relevant frequency of occurrence of such events would be the number of times the fluid “attempts” to move the ball per unit time over the relevant bed area. However, *not all* such events will lead to sediment particle motion. The probability of sediment motion itself could be described as a “doubly random” process, as it depends on: (1) the chance occurrence of the specific events in the particle’s neighborhood, and (2) the chance that the sediment will move *given that the fluid event has occurred*.

Now, consider a time scale, T_B , that characterizes the frequency (or period) of such flow events. Since, the turbulent bursting process is typically believed to transfer energy between the core and the wall region, it is assumed here that the bursting cycle period is characteristic of the time scale of the events. However, there is a controversy as to what flow variables (outer or inner wall) should be used for determining the time scale of the turbulent bursting process (see, for example, Cantwell, 1981; Bandyopadhyay, 1982). Additionally, such studies are mostly smooth wall investigations. In this work the convection time scale of the large eddies, $T_B = H/U_B$ (which is proportional to the time between bursts according to Nezu and Nakagawa, 1993), is used as the relevant time scale to characterize the frequency of sediment displacement. The probability of entrainment, P_E , is given by,

$$P_E = P_{TE} \underbrace{P_{BM/TE}}_{=1} \quad [\mathbf{V}\cdot\mathbf{3}]$$

where P_{TE} is the probability of occurrence of the specific flow event, and $P_{BM/TE}$, is the probability that the sediment will move *given that the flow event has occurred*. For simplicity, $P_{BM/TE}$ is assumed to be unity. It is perhaps more appropriate to refer to P_E as the nondimensional fractional sediment displacement rate, defined as,

$$P_E = \langle f_j \rangle T_B \quad [\mathbf{V}\cdot\mathbf{4}]$$

The definition and use of P_E in this work is viewed as defined in Equation V-4.

Alternatively, P_E may be interpreted as a probability of entrainment^(†) of a sediment particle.

To summarize, it is assumed that the flow derives the energy for moving the sediment from the core part of the flow, which contains the large eddies. Thus, generally

speaking, the frequency of occurrence of the relevant fluid events should scale with the convection time scale of the large scale eddy structures, given by, H/U_B .

V·3 Nondimensional Fractional Entrainment Rate as an Incipient Motion Criterion

The nondimensional fractional entrainment rate of mobile sediment, P_E , is determined by the sediment characteristics, such as the density, size and shape of the particles, the geometrical arrangement of the bed, and the fluid forces that are exerted on the sediment. In the present tests, 8-mm diameter glass spheres comprise the porous bed (4 layers thick), and the entrainable particles placed on the 5th layer as well. Such an arrangement eliminates particle size, shape and density as variables. However, P_E will still depend on the bed geometry (see Figure V·1) of the 4th and 5th layer roughness elements.

The concept behind the determination of critical conditions for different packing conditions is that the value of P_E is the same for all. That is, the flow condition that yields the appropriate value of P_E defines the incipient flow condition. Once the incipient value of P_E is determined for one packing condition, the same value of P_E applies for incipient conditions for all other packing densities as well. Physically, this is tantamount to saying that particles under different packing conditions experience an *effective* fluid force field that is similar for all the packing conditions such that the probability of entrainment of any randomly chosen particle (on average) is equal to P_E . As a first step, the experimental hydraulic conditions for all tests (single ball and multi-packing density tests) were established

[†] In this work, P_E denotes the chance that a sediment particle will move during a single energetic fluid event.

based on the equal- P_E concept, with the incipient value of P_E established by the 2% packing experiment.

V·4 Establishing the Hydraulic Conditions

The procedure to establish the experimental flow conditions is common to both the single ball and the five sediment bed packing density cases. This procedure was first applied to the five sediment bed packing density cases, and later, simply extended to the single ball case as well. Here, the methodology adopted for establishing the hydraulic conditions is described.

The incipient hydraulic condition was initially defined by choosing a flow condition that was *visually* judged to produce incipient motion of glass balls for the 2% packing density case. Several tests were carried out at 2% packing density, and one that produced sporadic glass ball motion was chosen as the “incipient” condition. Strictly speaking, this flow condition should be viewed as a condition that is capable of initiating glass ball motion at a certain but low rate. By this it is meant that a flow condition that exerted a *lower* mean fluid force on the glass balls could also move them, though such motions would be rarer. The $P_{E,crit}$ computed from the 2% test using Equation V·4 and the video analysis of sediment movement rates, fixed the $P_{E,crit}$ for the other four packing density cases. This value of $P_{E,crit}$ was 2.15×10^{-4} . The flow condition of the single ball test matched that of the 2% packing density case. Thus, the following discussion pertains only to the five packing density tests.

In all of the five packing cases the preliminary experimental procedure included, preparation and tight packing of the 4th layer, and careful distribution of 5th layer balls so

that they represented the correct surface packing density case. Care was taken to distribute the 5th layer glass balls at fairly regular, uniform distances (see, for example, Figure V-2). In all the cases the adjustable speed pump was started at a low discharge rate and was allowed to fill the flume up gradually, so that displacement of glass particles did not occur due to the initial surge of water. Care was taken to maintain good uniform water depth for all the tests.

The following steps were adopted in establishing the correct hydraulic conditions:

1. The isolated ball regime, the 2% case was chosen as the benchmark experiment. Thus, P_E established for the 2 % case was the value that was matched in the other packing density cases so that the incipient conditions were the same. The 2 % case was chosen as the benchmark since it yields more easily to theoretical analysis, and the case of an isolated ball has been studied extensively by several researchers (e.g., Fenton and Abbott, 1972; Coleman, 1966; Ling, 1995, Chen, 1970). Thus, the data obtained in the 2% case could be compared with other existing (see Papanicolaou, 1997) data.
2. For the 2 % case several preliminary tests at a fixed flume slope of 0.2 % but at different water depths were conducted. The goal was to locate the lowest water depth at which sediment motion could be visually observed. Several tests at water depths ranging from 4 to 6 cm were conducted, and the 5 cm water depth was chosen. At this depth, the glass ball motion was *visually* judged to be sporadic and infrequent, while at higher water depths, the motion was more frequent. At the 4 cm depth, the bed was relatively inactive. The 5 cm depth satisfied Bettess' (1984) criterion of $H/d > 3$ (so that the critical stress value is independent of H/d), and provided sufficient depth for the LDV

system measurements as well (the depth requirement for the LDV system is discussed later).

3. Several tests of the 2 % case were run and the bed mobility was captured using a video camera. Specific video frames were digitized using a frame-grabber software package, Adobe Premiere, 4.0, in a Macintosh Quadra 900 computer. The digitized frames were next converted from a 'pict' to a 'tiff' format using Debabilizer 1.5, again in the Macintosh Quadra 900 computer. The 'tiff' frames were imported into the image processing package, Khoros 1.0.5, in UNIX environment. The Khoros image analysis software enabled comparison of consecutive frames (time difference between "consecutive" frames ranged from 30 sec to a minute), while keeping track of the balls and their coordinates in each frame, and accounted for any possible ball movement that occurred between any two frames. Movement was detected by a change in the coordinate value of a ball. Several frames were compared likewise, and from the number of sediment particles that moved between two successive frames, the frequency of ball motion was computed (refer to Equation V-1). For more details about image processing and visual information analysis, reader is referred to Papanicolaou's (1997) work.
4. P_E was computed using Equation V-4 and the frequency information was obtained from step 3 above. T_B was estimated with $6H/U_B$ (see Nezu and Nakagawa, 1993). Here, U_B , the flow bulk mean velocity, was calculated from the measured flow rate and the water depth, H , measured at the test location.
5. In the variable packing density tests, for those cases with density greater than 2% the 5th layer sediment was placed upon the 4th layer at the appropriate packing density. The

flow condition to achieve the previously established P_E was obtained by trial and error.

The correct hydraulic conditions that produced the desired P_E value were found by systematically changing the flume slope and depth, establishing uniform flow depth conditions, and computing P_E through image analysis for all of the trial runs. Before each trial run, the 4th layer bed was packed, and the 5th layer erodible balls were carefully redistributed so that experimental initial conditions were nearly the same for all the trial runs.

6. Once a P_E value that was close to the reference value was found, the test was repeated. The hydraulic conditions were fine tuned so that the closest possible P_E value was obtained. The flow conditions that gave the closest P_E value determined the experimental flow conditions for the new packing case.
7. Similar steps (steps 4 to 6) were repeated for each of the packing cases, and their corresponding hydraulic conditions were established.
8. For the 70 % case P_E (maximum density packing) was computed manually. Manual computation was possible as particles that were removed from the fully-packed 5th layer left easily-identifiable gaps, revealing the 4th layer balls that were underneath. The number of 5th layer balls that were removed from such gaps within the test area within a specified time was counted. (Allowing too many 5th layer balls to leave from a single patch will result in local erosion, and yield false results. Care was taken to terminate the test so that such local erosions were avoided.) The 70 % case test was repeated several times with each test lasting about a minute.

The hydraulic conditions that pertain to each of the five sediment bed packing density cases and the single ball test are presented in Table V.1. The terms in Table V.1 are described in Section V.B.1 of this chapter. Specific experimental arrangement for the single ball test are detailed next. The first part, Section V.A, covers all aspects of the single ball experiment. This includes the test methodology that includes the LDV and video parts, a discussion of the data acquisition process, and post-processing.

V.A Single Ball Experiment

The purpose of the single ball experiment was to establish the correspondence between specific turbulent velocity events and the initiation of sediment motion. The experiment proposed here employed a three-component LDV system (for instantaneous velocity measurements) in conjunction with a video camera. The experimental setup was such that the camera simultaneously monitored the sediment (here, it is a glass ball) motion as well as the LDV data record. For the latter a simple electronic counter was used to display the LDV data count.

The single ball experimental work is divided into the following five aspects:

(1) rough wall arrangement and the placement of the single ball, (2) the alignment of the LDV system (appropriate to the multi density packing cases, as well) and proper placing of the LDV measurement volume with respect to the single exposed ball, (3) arrangement of the video camera and mirror setup, (4) establishing the relevant experimental flow conditions, and (5) data post-processing. The fourth aspect, determining the experimental flow condition, was described in Sections V.3 and V.4. The flow condition of the single ball

test matched that for the 2% sediment bed packing density test. Some aspects of the single ball experiment data post-processing are explained in Chapter VI. All other details are described at length here.

V·A·1 Preparation of the Rough Wall

Good packing of the porous bed was found to be very important. A stable undisturbed porous bed provided a strong supporting base for the single isolated 5th layer ball. The steps consisted of packing the 4-layer thick bed with colorless glass balls, and leveling with a flat wooden piece. The upstream gravel area was also packed well, such that the rough bed level was uniform throughout the length of the flume. For the single ball experiment even a tightly packed fourth layer tended to shift during the course of the experiment. Such a shift altered the resistance characteristics of the porous bed, and affected the ball entrainment process (see Figure IV·2). This problem was overcome as follows.

In the single ball experiment a large number of displacements of the single ball were recorded along with the LDV data. It was important that the bed resistance characteristics for all of these movements remained the same. In order to maintain the same angle of repose, bed resistance, and the ball's position relative to the LDV measurement point, the porous bed immediately beneath the single ball was glued together into a single cohesive, yet porous block. The glued block was $9.6 \times 6.4 \text{ cm}^2$. This glued block of balls remained firm and undisturbed during the course of the experiment, and allowed seepage flow to proceed, as well.

Placement of the single ball with respect to the underlying 4th layer balls was very important. There are at least two fundamentally different 4th layer ball arrangements that will affect the rate of entrainment of the 5th layer ball, as shown in Figure V.1. Both of the arrangements shown in Figure V.1 were tested. For the arrangement where the ball motion was less likely (more resistance of the 4th layer particles) the single mobile ball moved every 3 to 5 minutes. In the other situation, the ball moved every 30 seconds. The second situation that produced more frequent ball motion was chosen here, as it presented the lower incipient condition. Appropriate positioning of the single ball was done after completing the LDV and camera work. The LDV work is addressed next.

V·A·2 LDV Work

For carrying out the LDV alignment, the pump discharge was reduced and a slow-moving, deeper fluid stream was formed by placing a solid plate at the end of the flume. At such a low flow rate, the surface waves were reduced, thus, providing a clearer view of the laser beams, leading to better alignment results.

The first step in the LDV preparatory work was the alignment of the LDV system so that the six beams overlapped at the measurement volume. The major alignment procedure involved placement of optics as per the recommended layout followed by an alignment procedure that involved proper positioning of the two optical axes as outlined in the TSI manual (1985). For reasons of brevity only an outline of the major alignment procedure is provided here.

1. The laser was positioned such that the beam was centered on the alignment block (a specially manufactured aluminum block, with precisely located holes). Using the alignment block ensured the correct height of the laser beam (4.25 in. above the LDV optical table). The parallelism of the laser beam with the optical table was checked by positioning the alignment block as far away as possible from the laser front end. At this point the laser power was optimized by adjusting the laser mirrors so that maximum beam power was reached for a TEM₀₀ beam mode (see Drain, 1980, for different laser beam modes).
2. A beam collimator was positioned next. The collimator enabled locating the beam waist at the crossing point and was adjusted at the end of the alignment, and only if the beam waist was visually judged not to be at the crossing point. As with every piece of optics, the height of the laser beam was verified, and its power measured after the collimator.
3. A polarization rotator, that enabled laser beam power adjustment, was positioned next, followed by a color-splitting prism. Care was taken to ensure that the laser beam entered the prism at the Brewster angle (light reflected at the Brewster angle is perfectly polarized, and its cross section remains circular) and that the path length in each of its sections was nearly equal. The laser beam is split into its constituent colors by the prism. The three most powerful colors (green, 514.5 nm[†] ; blue, 488 nm; and violet, 476.5 nm), were chosen to effect LDV measurements.

[†] 1 nm = 10⁻⁹ m

4. The blue and green wavelength beams formed the primary optical axis, and the violet, the secondary. The heights of all the beams above the optical table and their relative spacings were observed using the alignment blocks, and were fine tuned as necessary.
5. A polarization rotator for the blue beam was positioned, followed by a beam splitter. A beam displacer was then employed to center the green beam, which was then polarized and split, similar to the blue beam. However, the planes containing the blue and the green beams were mutually perpendicular.
6. The Bragg cell frequency shifters for the blue and the green beams were positioned next. The shifted beam of each color was tuned for maximum power. Stray beams emanating from the frequency shifters were blocked by a pair of beam stops.
7. The violet photo collection system was positioned next.
8. The violet axis was then positioned based on the angle between the two optical axes. An angle of 30° was chosen for this work.
9. The violet beam, similar to the blue and the green beams, was polarized, split, and frequency shifted. Collection optics for the blue and green were positioned in the violet optical train.
10. Care was taken to maintain the path length of the primary (green and blue) and secondary (violet) optical axes to be nearly equal.
11. Proper crossing of the six beams was facilitated by using three, beam-steering modules. The steering modules were always used on the unshifted beams (if used on the shifted beams the power loss of the already-weak shifted beams could become excessive). The beam overlap was established by using a 50 micron diameter pinhole (to be discussed).

12. Care was taken to center the six beams on the two front lenses (such centering maximizes scattered light collection) and on the front glass of the optical window.
13. The next step was to align the photo multiplier tubes (PMT's) so that they focused on the crossing point. This was achieved by moving the traverse table, so that the six beams clipped the edge of the pinhole. The clipped pinhole edge served as a scattering source, and the PMT's were aligned based on the scattered pinhole image. More details of the pinhole alignment is provided in Laser Velocimetry Systems (1985).

The minor alignment procedure (step 13) consisted of fine tuning the beams (by steering) and aligning the PMT's so that the scattered light was collected only from the measurement volume.

To obtain good signals the following points were adhered to:

- a) The beam mode was verified to be TEM_{00} , as deviations from this mode resulted in unacceptable beam alignment, and optical component performance.
- b) The power in the frequency-shifted beams was maximized so that the power in the shifted beam was nearly equal to its unshifted counterpart.
- c) The six beams were aligned properly so that they were all positioned relative each other correctly. This was confirmed by using the alignment block.
- d) The PMT's were properly focused so that scattered light collection occurred only at the LDV measurement volume.
- e) The waist of the laser beams was located at the crossing point. This was achieved by adjusting the collimator.

Before each set of measurements, both major and minor alignments were carried out. This was necessitated by lack of temperature control in the laboratory, which resulted in the laser beams tending to drift due to thermal expansion problems.

The following alignment procedure was followed to achieve good beam overlap (crossing):

- 1) A 50 micron diameter pin hole was used to ensure proper crossing of the six beams in water. The water box (see Figure IV·7) was filled with water so that the six beams entered the flume water without adverse refraction effects. To ensure minimum disturbance to the 4th layer balls, a flat steel plate (8 in. x 12 in. long x 1/7 in. thick) was placed on top of the 4th layer. The alignment pin hole and a black aluminum block (so that the laser beams were more easily visible) were placed on top of this plate. By moving the LDV traverse table relative to the pinhole the crossing point (measurement volume) was positioned on the pinhole such that the six individual laser beams passed through the pinhole and struck the black aluminum block.
- 2) The precise crossing point was located when all of the six beams appeared and disappeared at the same time when traversed in the x and z directions.
- 3) With the pin hole undisturbed, the LDV table was moved such that the beam crossing point clipped the pin hole's metallic edge. The PMT's were focused on the scattered light coming from the metallic edge. Each of the three PMT's was focused so that the two spots associated with the appropriate beam pair overlapped.
- 4) The pinhole was then removed from the flume.

- 5) Initial signal quality was visually checked on the oscilloscope. The shape of the histogram in the FIND software served as an additional guide of signal quality, filter bias effects, and provided data rate information as well.
- 6) Once good signals were confirmed, the position of the laser beam with respect to the top of the 4th layer was located by traversing the LDV table until the signal from the green (514.5 nm) channel on the oscilloscope just started to fade away. Since the thickness of the steel plate located atop the 4th layer was known, the distance of the LDV crossing region from the top of the 4th layer could be easily calculated. At the end of this step, the steel plate, and other foreign materials were removed from the flume.
- 7) The next step was to locate the LDV measurement volume at an appropriate location upstream of the single mobile ball. Based on Naden's (1987) work, the fluid velocity measurement point was located $0.57d$ from the top of the 4th layer, where the effective drag acts (refer to Chapter II and Table II-1 for a discussion). The single exposed ball was placed at an appropriate location as discussed in Section V-A-1. The LDV measurement volume was positioned upstream of the ball at a distance of $318\ \mu\text{m}$ from the ball's surface. The ellipsoidal LDV volume is estimated to be $80\ \mu\text{m} \times 320\ \mu\text{m}$, which makes the shortest distance between the ball's surface and the LDV measurement volume to be $278\ \mu\text{m}$ (see Figure VI-2).

V·A·3 Camera and Mirror Arrangement

The next step was to position the camera, the simple electronic counter and the mirror such that the camera monitored the ball motion as well as recorded the LDV data count.

1. The video camera was set up as shown in Figure IV·6. Care was taken to locate the single exposed ball at about mid-screen of the camera and the camera was zoomed in such that it covered an area with 15 ball diameters (12 cm) to a side. This arrangement permitted filming the course of the ball motion for a distance of about 7 ball diameters. The top of the camera screen was occupied by the mirror.
2. The mirror and the counter were positioned such that the LDV data count could be read clearly when viewed through the camera.
3. Next, the test flow conditions were established. For the single ball test, the flow condition was that for the 2% sediment bed packing density case. After achieving the test flow conditions, the camera was started, followed by the LDV data acquisition system. Data acquisition was automatically carried out by the LDV data collection system.
4. There is only one mobile glass ball which must be replaced, at the same precise location on the bed, after each displacement episode. This is a tedious process involving manual repositioning of the ball with a long slender “grabber.” LDV data acquisition was not suspended during this process. Care was exercised in placing the ball back exactly at the same point on the bed and relative to the LDV measurement volume. The exact placement location was dictated by the LDV crossing point. Additionally, the 4th layer

balls immediately underneath the test ball were painted blue for easy placement location identification. Though the bed underneath the entrainable ball was glued, thus, presenting a firm, yet porous surface, care was taken not to disturb the 4th layer balls elsewhere in the bed as well. The data collection continued until the next ball motion occurred. The single ball was again replaced and data collection continued. This procedure was repeated for 120 such entrainment events.

5. At the completion of the measurements the LDV laser beam geometry was measured. This was required in order to determine the LDV fringe spacings and the geometric orientation of the measured velocity components. For these measurements the steel plate, pinhole and the aluminum block were again placed back in the flume water, and the laser beams were again aligned through the pinhole as outlined before. For the beam geometry measurements, the pinhole location was designated as the origin (0,0,0). The LDV table was traversed in the y-direction (spanwise) by the maximum allowable distance. Typically this distance was about one inch and was restricted by the maximum allowable extension of the rubber bellows (see Figure IV.7) of the optical water box. Then, by moving the traverse table, each of the six laser beams was located, and the corresponding coordinate values were noted. The readings were repeated to confirm the coordinate values. These coordinate values were used to calculate the equation of the line (for each beam) describing each laser beam, and subsequently the geometric arrangement of the LDV beam system.

The next step was to post-process the experimental data so that the measured velocity components were transformed to the orthogonal flume coordinate system (see Figures II-7a and 7b). The data post-processing described next applies to both the single ball as well as the multi packing density tests.

V·A·4 LDV Data Post-Processing

This section details conversion of the ‘raw’ experimental data obtained with the commercial software to an ASCII form and further analysis using different statistical techniques. The data post-processing consisted of the following major steps:

1. Conversion of the ‘raw’ LDV data to an ASCII form was effected through a FORTRAN program, Rtoascii.exe, developed by TSI, Inc. Since the original program could handle only single files, modifications were effected to run it in batch mode. This was achieved through the FORTRAN program. Thus, for batch processing, this program was used, which automatically accessed Rtoascii.exe for every file in the batch. The result of this operation was a file (or sequence of files) in ASCII containing information which was used to subsequently calculate individual velocity components for each seed particle passing through the LDV measurement volume.
2. The beam coordinate measurements detailed in step 9, Section V·A·8, were then used to compute the coordinate transformation matrix elements using a program written for TK Solver software (Ldageor). The input to this program were the coordinate measurements of the six beams. The output from Ldageor included the angle between the three pairs of beams (θ_v , θ_g , and θ_b , where subscripts v, g, and b denote the violet,

green and blue beams, respectively), three unit vectors perpendicular to the planes containing the fringes, elements of the 3x3 transformation matrix, and the angle between the bisectors of the two optical axes. The angle between the beams, θ_v , θ_g , and θ_b , were used to compute the fringe spacing, f_s , using equation in Appendix A1.

3. The ASCII files do not contain the measured velocities, rather these files contain the LDV counter number (whether the channel being recorded is green, blue, or violet), the number of fringes (N_f) crossed (here it is 8), the transit times (X_b) in nanoseconds (ns) to cross the prescribed number of fringes, and the time between validated data (TBD), in micro seconds (μs) for each of the measured LDV seed particle.

A separate program, Menu3d.for, was written to read the ASCII file(s) and to transform the transit time information to frequency (in terms of fringes crossed per second), given by,

$$f_{fb} = N_f / X_b \quad [\text{V}\cdot\text{5}]$$

where the subscript b stands for violet, green or blue beams, and f_{fb} , the frequency that corresponds to a specific pair of beams. The frequency, f_{fb} , was further corrected for any Bragg cell frequency shift, f_{sb} , as

$$f_{cb} = f_{fb} - f_{sb} \quad [\text{V}\cdot\text{6}]$$

where f_{cb} is the Doppler frequency proportional to the particle's velocity. The velocity component was calculated from f_{cb} as,

$$V_b = \lambda_s f_{cb} \quad [\text{V}\cdot\text{7}]$$

where λ_s is the fringe spacing, discussed in Appendix A1. Equations V.5 to V.7 are applicable to the violet, green and blue beams. V_b was then transformed to the velocity components in the flume coordinate system using the transformation matrix. The result of the operation (Menu3d) is the three velocity components for each of the measured seed particles in the flume coordinates. The instantaneous velocities were then used to compute flow statistics such as mean velocities, root-mean-square (rms) values, and various Reynolds stress components.

V·B Sediment Bed Packing Density Experiments

The objective of these experiments was to investigate the nature of fluid-solid interaction under flow conditions that begin to produce sediment motion under five different sediment bed packing densities. Determination of the flow conditions were described in Section V.4. This section details the general methodology, LDV work, location of the measurement points, and data post-processing.

Detailed flow velocity measurements close to the roughness elements were carried out using the 3-D LDV system. The determination of hydraulic conditions described Section V.4 required 5th layer particle mobility. However if flow velocity is to be measured close to the roughness elements, mobility alters the local flow structure and hence, affects the velocity measurements. As a practical matter a glass ball can roll and block the laser beams, preventing collection of any data. The beam blockage possibility exists for measurements below the top of the 5th layer (but above the 4th layer). Also, the LDV measurements take several hours for completion and the bed morphology would change significantly in this

time. Given sufficient time, an incompletely packed 5th layer would rearrange itself to form cluster microforms, while, in the 70 % case, significant local erosion of the 5th layer balls would occur. As mentioned before, significant clustering has the undesirable effect of changing the bottom boundary condition, thus, altering the experimental conditions.

To avoid the cluster microform formation and to effect detailed velocity measurements close to the roughness elements, it was important to *immobilize* the bed. This was achieved by using lead balls, in place of the 5th layer glass balls. The lead balls, approximately the same diameter, but much heavier (due to higher density), will not move when exposed to flow conditions that correspond to the incipient condition of the glass balls. LDV measurements were carried out with the lead balls in position. The following section describes the experimental flow conditions, followed by the LDV data collection procedure, and data analysis for the five packing cases.

V·B·1 Experimental Flow Conditions

The flow conditions for each of the five sediment bed packing density cases and the single ball experiment are presented in Table V·1. In all of the tests care was taken to reduce the side wall effects by limiting the aspect ratio of the channel flow, W/H , to be greater than 6 (Nakagawa and Nezu, 1986), and the H/d ratio to be greater than 3 (Bettess, 1984).

For the five packing cases the depth average velocity, U_B , ranged from 0.4 to 1.2 m/sec. U_B was calculated from measurement of the volumetric flow rate, via a U-tube

manometer (water, for low flow rates and mercury, for high flow rates) attached to the venturi as,

$$\begin{aligned}\dot{Q} &= 0.00306\sqrt{\Delta H} \quad \Delta H \text{ in cm, for the water manometer} \\ \dot{Q} &= 0.0109\sqrt{\Delta H} \quad \Delta H \text{ in cm, for the mercury manometer}\end{aligned} \quad [\text{V}\cdot\mathbf{8}]$$

where \dot{Q} is the volumetric flow rate in m^3/sec , and ΔH is the differential head between the two legs of the U-tube manometer. Thus,

$$U_B = \frac{\dot{Q}}{H W} \quad [\text{V}\cdot\mathbf{9}]$$

where H is the water depth above the 4th layer (5th layer for 70% packing) and W , the flume width, equal to 60 cm.

The friction velocity, shown in Table V-1 was calculated (for uniform flows) with,

$$u_* = \sqrt{gHs} \quad [\text{V}\cdot\mathbf{10}]$$

where g is the acceleration due to gravity, H , the water depth (above the top of the porous bed), and s , the flume slope expressed as gradient. It is common in hydraulics to normalize the wall shear, τ_w (where, $t_w \equiv \tau_w = \rho g H s$) as,

$$\tau_* = \frac{\tau_w}{(\rho_s - \rho)gd} = \frac{Hs}{Rd} \quad [\text{V}\cdot\mathbf{11}]$$

Here τ_* is the normalized wall shear, ρ_s and ρ , the sediment and fluid (here it is water) density, respectively, d , the sediment size (ball diameter), and R , the immersed weight per unit volume, is $(\rho_s - \rho) / \rho$.

The Reynolds number, shown in Table V-1, is defined as,

$$\text{Re} = \frac{H}{\nu} U_B \quad [\text{V}\cdot\mathbf{12}]$$

where ν is the kinematic viscosity of water.

For rectangular channels the Froude number is defined as,

$$Fr = \frac{U_B}{\sqrt{gH}} \quad [\text{V}\cdot\mathbf{13}]$$

where $Fr < 1$ is termed subcritical flow, $Fr = 1$, critical, and $Fr > 1$, supercritical flow. The first three packing cases (2, 20 and 35 %) are subcritical flows, the 50 % case is nearly critical, and the 70 % case is supercritical.

In all of the packing density case runs, the bed morphology was not allowed to change significantly from its original form. Significant bed morphology changes lead to a sediment clustering effect. Clustering occurs when the distributed particles cluster together to form disjointed “islands” of particles. Significant clustering alters the fluid-solid interaction, and presents a different boundary resistance and condition. Another reason for avoiding bed morphology changes during any given test, is that, in the high packing density cases, significant clustering tended to saturate the video image and individual particle edges were obliterated, thus preventing accurate image analysis.

V·B·2 LDV Procedure for Packing Density Experiments

The procedure followed for collecting velocity measurements using the three-component LDV system had several common features with that for the single ball test. The LDV experimental procedure can be split into two parts, viz., the preparatory work, and the experimental work, which includes post-processing of the data files. The preparation of the 4th layer roughness for these tests was exactly the same as that for the single ball test; so

was the LDV alignment procedure, described in Section V·A·2. Here features unique to the sediment bed packing density tests are described.

The major steps involved for the five packing density tests are:

1. Preparation of the well-packed, 4-layers thick, rough bed of colorless glass spheres .
2. The next step was preparation of the LDV system ready for data collection. LDV alignment procedure detailed in Section V·A·2 was followed. This included major and minor alignment procedure, and overlapping of the six laser beams in the measurement volume using the pinhole.
3. Sediment particles (lead balls) that corresponded to a specific packing density test were distributed evenly on the 5th layer. Then, the test flow conditions, provided in Table V·1, were reached. The test flow conditions were determined from the mobile bed study, using image processing techniques, described in Section V·4.
4. Next step involved setting the coordinates of the LDV data files. The lowest and the highest points above the roughness layer that the laser beams could reach and measure were determined as follows. The lowest point was determined by the height at which the sediment elements obstructed the laser beams. The highest point was limited by the interference of the laser beams with the free surface of the water in the flume. The lowest and highest points essentially fixed the coordinates of the first and last data files in a traverse normal to the sediment bed. One lead ball was strategically located such that the LDV measurement volume was directly above it (LDV system was moved appropriately to fine-tune the final position).

5. The LDV measurement volume was positioned at the coordinates of the first file and the sequence of measurement positions was entered into the traverse table control program, FIND. The LDV traverse table was then switched to computer-control mode.
6. Data acquisition was automatic, with the computer repositioning the LDV table systematically according to the entered coordinates. LDV seed feeding, however, was periodically required, and was done manually. All the data files, typically contained 3k data points (3072 data points) for each measurement location, for obtaining good flow averages.
7. Three sets of measurements were taken for each packing case as discussed at the end Chapter II. The measurement locations were situated at a distance of 1 ball diameter directly upstream, and downstream of the ball, and the third was located directly above the ball as shown in Figure V-3. At each of the three locations about 40 to 50 points in the direction normal to the bed were selected for LDV data acquisition (each data file had 3072 data points). Completion of the last data file signaled the end of the data acquisition part of the experiment.
8. As described in Section V-A-2, at the completion of the LDV measurements the LDV geometry was measured.

As in the single ball experiment, the next step was to post-process the experimental data so that the measured fringe count and transit times were converted to velocities and then finally to velocity components in the orthogonal flume coordinate system (see Figures

II.7a and 7b for the flume coordinate system). This was carried out as described in Section V.A.4. From the instantaneous velocity values in flume coordinates, the mean values of the streamwise, normal and spanwise velocities, their standard deviations, and the Reynolds shear terms, were computed. All of the mean quantities were velocity bias corrected as outlined in Appendix A2. The instantaneous velocity values were used in computing the quadrant contribution to the Reynolds shear production, probability density distributions of the normal stress components such as u^2 , and w^2 , details of which are included in Chapter VI.

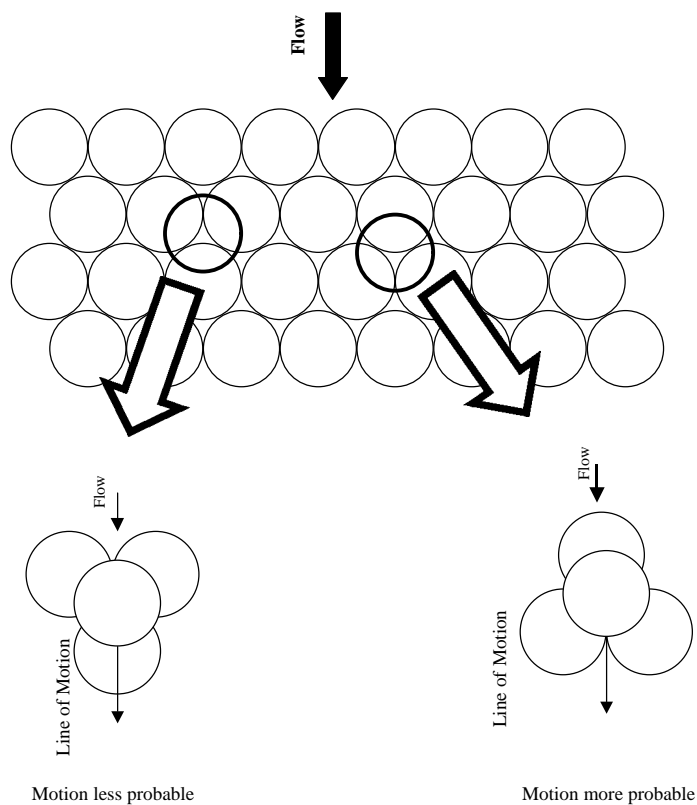
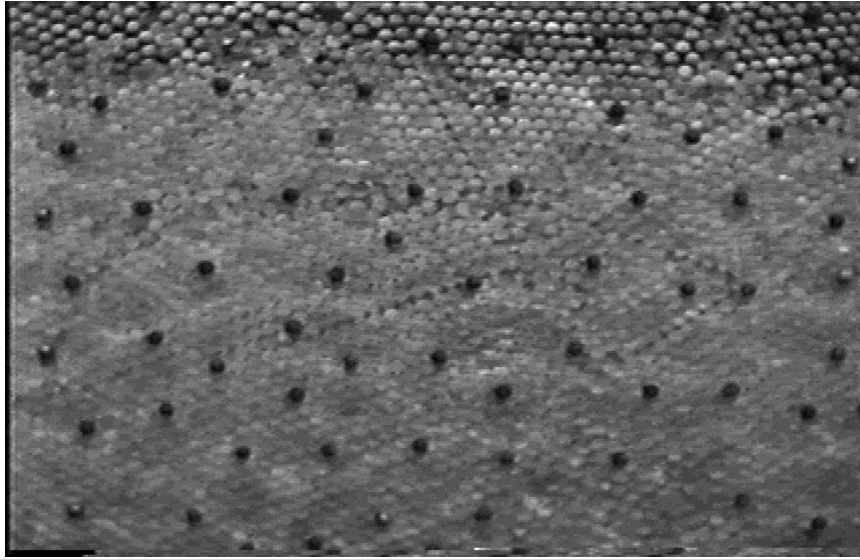


Figure V.1. Two fundamentally different ball entrainment situations arising purely from geometry.

(a)



(b)

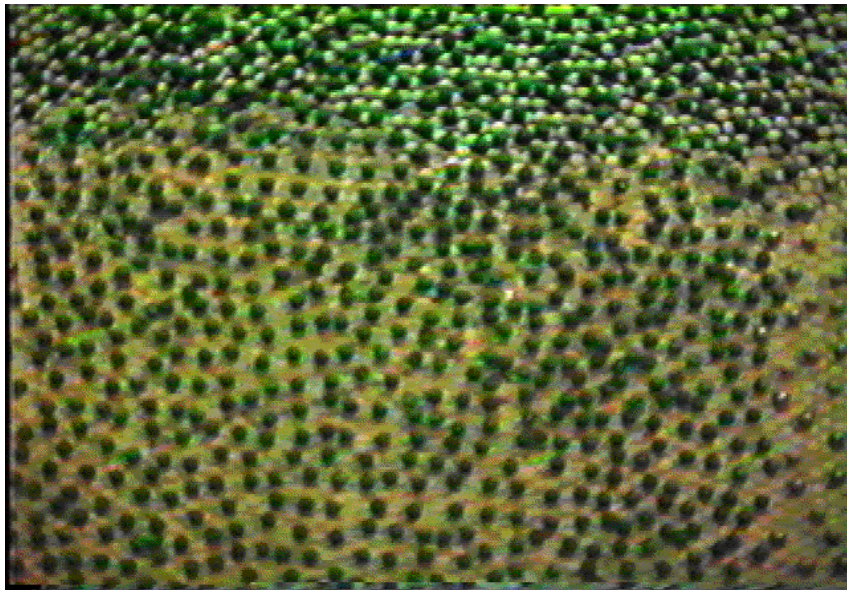


Figure V.2. Top view of ball distribution for (a) the 2% case, and (b) the 20% case.

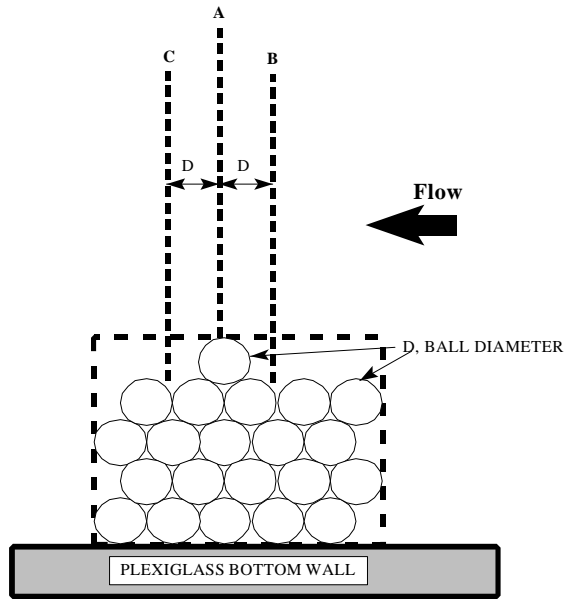


Figure V.3. LDV measurement locations for the five sediment bed packing density cases.

Table V.1. Summary of hydraulic conditions for the five packing cases.

Packing %	Slopes, %	Depth H, cm	U_B m/sec	\dot{Q} m ³ /sec	W/H W = 61 cm	H/d d = 8 mm	u_* m/sec	τ_*	Re x 10 ⁻⁴	Fr
2	0.2	5	0.4	0.012	12	6.3	0.0313	0.008	8	0.57
20	0.2	6.8	0.53	0.022	9	8.5	0.036	0.011	14	0.65
35	0.8	5.7	0.71	0.025	11	7.1	0.067	0.037	16	0.95
50	1	5.7	0.76	0.026	11	7.1	0.075	0.048	17	1.01
70	1.2	7.6	1.2	0.054	8	9.5	0.093	0.074	36	1.37

Chapter VI

Analysis and Results

VI-1 Introduction

In this chapter, the results of this work are presented. As a first step, the analysis of the forces experienced by a single ball placed atop a porous bed and exposed to a fluid stream is described. This analysis has been carried out before by several researchers (e.g., Chen, 1970; Coleman, 1967) and the intent of re-deriving the equation is to elucidate the forces acting on the isolated sphere, the influence of the geometry of the supporting 4th layer, and more importantly, show the formulation of a new variable that directly results from the moment-balance equation. The results are divided into two sections; first, the single ball case is discussed, followed by the five sediment bed packing density cases.

VI-2 Moment Balance of a Single Ball

The problem considered here is that of a single, exposed ball placed atop a porous bed of identical spheres. As stated before, the predominant fluid force experienced by the ball is form drag. In this configuration the lift force is small in comparison to drag, due to the ball's large frontal exposure to flow (the lift force may not be negligible, however,

since pressure differences between the top and bottom surfaces of the sphere may be present due to the acceleration of the fluid over the surface).

For the following discussion refer to Figure VI-1. The dominant forces acting on the ball are:

1. The immersed weight of the ball, W_b , assumed to act through the center of gravity of the ball, is given by,

$$W_b = m_b g = \frac{\pi}{6} (\rho_p - \rho) d^3 g \quad [\text{VI}\cdot\text{1}]$$

where m_b is the immersed mass of the ball, ρ_p , its density, g , the local gravitational acceleration, ρ , the fluid density, and d , the ball diameter.

2. The instantaneous drag force, F_D , that the fluid exerts on the ball is modeled as:

$$F_D = \frac{1}{2} C_D \frac{\pi}{4} d^2 \rho U^2 \quad [\text{VI}\cdot\text{2}]$$

where C_D is the coefficient of drag, and U , the instantaneous streamwise velocity.

3. The instantaneous lift force, F_L , that the fluid exerts on the ball is modeled as:

$$F_L = \frac{1}{2} C_L \frac{\pi}{4} d^2 \rho W^2 \quad [\text{VI}\cdot\text{3}]$$

where C_L is the coefficient of lift, and W , the instantaneous normal velocity.

Formulation of the lift force by the normal velocity is rather unconventional and has been adopted by other researchers before (Yalin, 1977; Naden, 1987).

In Figure VI-1, F_D is shown to act through the center of gravity of the ball. In general, this has not been found to be true (e.g., Einstein and El-Samni, 1949; Naden,

1987; Bridge and Bennett, 1992). The effective drag is often assumed to act at a distance of $0.7d$ from the reference level (see Naden, 1987, for example, and refer to Table II-1), whose location is typically *not* known. The reference level is defined as the distance at which the loglaw profile of $\langle U \rangle$ becomes zero (see, for example, Tennekes and Lumley, 1992). Thus, it is assumed that the loglaw applies all the way to the top of the roughness elements, which is contrary, for example, to Raupach et al.'s (1991) observation of a non-universal roughness sublayer. Despite its shortcomings, defining a reference level simplifies applying the moment balance equation. It should be mentioned that the choice of the reference level in no way affects the character of the distribution of flow variables, although their magnitudes may be affected.

Several researchers have recommended different reference-level distances measured from the top of the rough bed. For example, Einstein and El-Samni (1949) recommended $0.2d$; Sumer and Deigaard (1981), $0.25d$; and Jackson (1981), $0.30d$. In this work, the reference level is taken to be at $0.2d$ below the 4th layer and F_D was assumed to act $0.7d$ (Einstein and El-Samni, 1949) from the reference level. It is emphasized that the reference level location is used only in the moment equation and in the formulation of a new variable (to be discussed) that results from the moment equation.

For the fully exposed single ball, rolling is the primary or preferred mode of motion initiation. The minimum condition for rolling motion is determined by taking the moment about the point c_2 , and the rolling occurs about line $x-x$, both shown in Figure VI-1. The minimum moment condition (see Coleman, 1967) is considered, as it determines the lower bound of the incipient motion criterion. The balance of moments yields:

$$F_D l_3 + F_L \cos(\beta) l_2 \geq W_b \cos(\beta) l_2 f_h \quad [\text{VI}\cdot\text{4}]$$

where l_3 and l_2 are shown in Figure VI.1, and β is the angle the bed makes with the horizontal plane. The term f_h accounts for the hydrodynamic mass effect, which will be discussed shortly. In the above equation, since β is small, the term $W_b \sin(\beta)$ has been neglected. From the geometry of the figure l_3 and l_2 are deduced to be,

$$l_2 = \frac{d}{4\sqrt{3}} \quad \text{and} \quad l_3 = \frac{d}{\sqrt{6}} \quad [\text{VI}\cdot\text{5}]$$

Note that the values of l_2 and l_3 shown above are for the minimum moment condition (Coleman, 1967). When Equations VI.1 to VI.5 are combined, the result is,

$$A_1 U^2 + A_2 W^2 \geq C f_h \quad [\text{VI}\cdot\text{6}]$$

where the constants, A_1 , A_2 , and C are defined as,

$$A_1 = 0.125 C_D \rho \pi d^3 \frac{1}{\sqrt{6}} \quad [\text{VI}\cdot\text{7}]$$

$$A_2 = 0.125 C_L \rho \pi d^3 \frac{\cos(\beta)}{4\sqrt{3}}$$

$$C = \frac{1}{24\sqrt{3}} \pi (\rho_p - \rho) g d^4 \cos(\beta) \quad [\text{VI}\cdot\text{8}]$$

Here, C denotes theoretical minimum moment required to just move the ball. When the ball moves, it must push a finite mass of fluid out of the way. If the body is accelerated (the ball starts from rest when its motion begins), the surrounding fluid is accelerated as well. Thus, the ball feels as if it is heavier by an amount called hydrodynamic mass, m_h . For spherical particles (based on potential theory) m_h equals one-half of its displaced mass (see White, 1986),

$$m_h = \frac{\pi}{12} \rho d^3 \quad [\text{VI}\cdot\text{9}]$$

Thus, $m_{\text{eff}} = m_h + m_b \quad [\text{VI}\cdot\text{10}]$

where m_{eff} is the effective mass. Thus, f_h becomes

$$f_h = \frac{\rho_p - 0.5\rho}{\rho_p - \rho} \quad [\text{VI}\cdot\text{11}]$$

It can be readily seen that for fluid densities approaching small values (for example, air), f_h approaches 1, while for the case at hand, it is 1.325. The equality in Equation VI-6 describes the threshold moment value. Any moment that is greater than the threshold value can cause ball motion.

Equation VI-6 is used as the basic moment-balance equation for the single ball case, as well as for the 2, 20, 35 and 50 per cent surface packing cases. The moment balance equation for the packing density cases is addressed by Papanicolaou (1997). The constants A_1 and A_2 will change from one packing to the next, essentially due to the changes in C_D and C_L values resulting from Reynolds number changes. The above equation holds even for the 50 % case because, the balls are not in physical contact with each other and are free to move. Only the fully-packed 70 % case differs because the physical contact of the balls precludes any rocking motion and forces the initial motion to be a vertical lift off.

In the 70 % case, there is negligible deflection of the flow by the fully-packed bed, as the flow simply skims the rough surface. The initial ball motion is caused by the lift force, F_L , that counters the immersed weight, W_b , of the ball. There are no moments nor

any rolling. Large lift is generated due to the pressure difference between the ball top and bottom. Thus, F_L here is modeled as,

$$F_L = \frac{1}{2} C_L \frac{\pi}{4} d^2 \rho U^2 \quad [\text{VI}\cdot\text{12}]$$

Equation VI-12 applies *only* to the 70% case. Because of the geometry of the bed, the moment balance equation for the 70% case becomes equivalent to the balance of forces. Thus,

$$F_L \geq f_h W_b \cos(\beta) \quad [\text{VI}\cdot\text{13}]$$

on substituting Equations VI-1 and VI-12 to the above equation,

$$U^2 \geq \frac{g d}{0.75 \rho C_L} f_h (\rho_p - \rho) \cos(\beta) \quad [\text{VI}\cdot\text{14}]$$

The equality in the above equation denotes the threshold value. Note that the right hand side of Equation VI-14 is a constant (a steady state C_L value is used here¹). The critical value of moment that just overcomes the sediment's resistance to motion (the right hand side of Equations VI-6 and VI-13) will be considered later in the results section of the single ball experiment.

VI-3 Results

The results section is divided into two parts. The first part covers the single ball case and the second, the five sediment bed packing cases. The main objective of the single ball case was to identify and investigate the characteristics of the velocity events that occur (as measured by the LDV system) prior to the ball motion. This was accomplished

by considering the correlation between ball motion and velocity events that preceded ball motion. The sediment bed packing cases investigate the nature of solid-fluid interaction (without sediment motion) and attempt to explore the extent of the roughness sublayer as delineated by different flow variables, such as mean velocities, rms quantities, and the Reynolds shear stress component, $\langle uw \rangle$.

VI-4 Single Ball Experiment

The main objective of the single ball experiment is to investigate the correlation between fluid velocity events and ball motion. As a prelude to results, the experimental setup, procedure, and data acquisition are revisited in the following sections.

The experimental setup for the single ball case is shown in Figure IV-6. The single exposed glass ball was placed atop the porous 4th layer consisting of identical spheres. The final location of the glass ball with respect to the LDV measurement volume was appropriately chosen, and will be discussed shortly. The 4th layer geometry was such that the single exposed ball had a higher probability to move (refer to Figure V-1).

The height of the LDV measurement volume from top of the 4th layer was $0.57d$ (4.4 mm, see Figure VI-2). This distance was experimentally determined by Einstein and El-Samni (1949) as the distance at which the effective drag acts on the ball. The streamwise distance of the LDV measurement volume from the surface of the erodible single ball is important. A short transit time from the LDV volume to the ball surface will likely yield a lower uncertainty in the experimental results. From a practical point of view,

¹ Unsteady lift coefficients have been found to be significantly higher than the steady state values. Reader is directed to an article in the Mechanical Engineering Magazine, vol. 119, No. 3, 1997, page 144.

this location (in the streamwise direction) was determined by the shortest location from the ball surface that yielded good LDV signals. The distance of the LDV measurement volume from the surface of the ball was 318 μm . Figure VI-2 shows the location of the LDV measurement volume with respect to the single ball and other relevant distances.

Completion of the preparatory work (preparation of the rough wall, LDV and camera) described in Chapter V, signaled the commencement of data acquisition. The video camera was started first, followed by the LDV system. In the single ball experiment the LDV measurement volume remained fixed at the location identified in Figure VI-2. The sequence of the experimental events is described below.

When ball motion occurred, the ball typically rolled out of the original position indicated in Figure VI-2, while the LDV data acquisition continued unabated (in fact, during the entire course of the experiment, the LDV data acquisition was never stopped). Using a long slender “grabber” the ball was repositioned back at the precise original position. In the elapsed time between ball movement and ball replacement, the LDV system continued to make velocity measurements. These measurements are irrelevant to the purposes of the single ball experiment, and were discarded during data post-processing. This process of ball rolling and repositioning was repeated 120 times during a time period of two hours.

The first step of the data analysis for the single ball case involved viewing the video record to identify the frames in which ball motion occurred. In these frames, the LDV data count that occurred just prior to ball motion was noted. Then, the time difference between the occurrence of the first LDV measurement and the ball motion was

computed by counting the number of frames between the two. A similar procedure was repeated for all of the ball motions (about 120) captured by the video. The useful LDV data correspond to those that were acquired with the ball in “original” position, as indicated in Figure VI-2. These LDV measurements (16962) were extracted from the entire LDV data record ($15 \times 3072 = 46080$ data points) for further analysis. Thus, the fraction of useful data from the total acquired is $16962/46080$ or 37 per cent. The remaining 63 per cent that occurred with the ball out of position were discarded.

The final, useful data record of 16962 points, appropriately extracted from the total data points of 46080 and sequentially joined, provided the basic data for the single ball analysis. Again, these data were acquired with the glass ball in the original position with the LDV measurement volume upstream of the ball. The entire LDV data record could now be plotted in time. Since the LDV data record was formed by patching select groups of data, a continuous time record was obtained by forming the cumulative-time-between-data (CTBD) of the 16962 data points. On the same time scale, the ball motions were also spotted. An example of such a time series (schematic) is shown in Figure VI-3. The correlation between ball motion and LDV velocity measurements can be established by using a statistical procedure that is commonly used in photon correlation (e.g., Mayo and Smart, 1980), as explained next.

VI-4-1 Correlation Between Ball Motion and Turbulence Events

The basic principle behind establishing the correlation between ball motion (BM) and the fluid event (TE) is considered first. The objective of the single ball experiment is

to measure correlation between ball motion and LDV velocity measurements. The main difficulty in establishing a correlation between ball motion (BM) and fluid velocity (i.e., turbulence events, TE) arises because BM is a “binary” signal. That is, it has two states: either the ball has moved (yes) or has not moved (no). Establishing a statistical correlation between a “yes-or-no” signal and a continuous TE signal (though LDV measures only discretely) is uncommon. A situation somewhat analogous to that discussed above is encountered in photon correlation (see, Mayo and Smart, 1980; Mayo, 1978). This special statistical procedure is employed here as well. All of the following discussions are based on Figure VI-3.

VI-4-2 Correlation Between Ball Motion and Upstream Velocity

Consider two random processes occurring in time, x and y . Both x and y are not continuous signals but consist of random individual digital “pulses.” The two processes are random in time but correlated with each other. The time records of both signals can be divided into subintervals of duration Δt , the slit-window width. The number of subintervals is $N = T/\Delta t$, where T is the total time of observation. T is the same for both x and y .

Assume that within the j^{th} subinterval (where j can run from 1 to N) x_j and y_j pulses occur in the two random variables. The cross “correlation” between the number of events in x and y is a function of the lag time, $\tau = m\Delta t$, and can be estimated from

$$\rho_{xy}(m \Delta t) = \sum_{j=1}^N x_j y_{j+m} \quad \text{[VI-15]}$$

where m is the lag number. In the present case x represents the ball motion and x_j is either 1 or 0 for all relevant Δt and τ . y_{j+m} represents the number of velocity measurements in the slit window width Δt , at a time lag of τ , prior to ball motion. Therefore, in the present case, Equation VI-15 can be rewritten as,

$$\rho(m\Delta t) = \sum_{j=1}^N (BM_j) TE_{j+m} \quad \text{[VI-16]}$$

where ρ is termed loosely as the “correlation” between BM and TE. In Equation VI-16 ρ is the same as ρ_{xy} shown in Equation VI-15. As mentioned before, the value of BM_j is binary. If TE_{j+m} is just the number of events that occurred with the prescribed slit window, Δt , then ρ reduces to the number of events that are included in Δt , for various values of the lag number. However, if TE_{j+m} is defined so that only the number of turbulent events of specific magnitude are included (for example, $U > 0.2$ m/s), then ρ would indicate the *number* of such ‘special’ or ‘filtered’ events.

It should be realized that for LDV data, with nearly a Poisson process of data arrival, with unequal time intervals between data, there is in principle no limit on the size of Δt . However, in practice, since the data record is of finite length, maximum size of Δt is limited by the length of record, while minimum Δt value is limited by the scatter in the resulting correlation function due to fewer events occurring in the slit window as Δt becomes very small.

The correlation, ρ , between the ball motion and measured velocity events was computed as discussed before in this section and is shown in Figures VI-4 to VI-6 as a function of the lag time, τ . The three different Δt values (40000, 100000 and 250000 μs)

were investigated. The relative magnitudes of the three chosen Δt values, relevant flow structures, and those of the experimental equipment are important. Such a comparison helps to justify the results obtained from the study. Table VI-1 presents relevant time scale of the flow as measured by the LDV system (burst period, lifetime of a burst, convection time of a fluid parcel from the LDV measurement point to ball, and convection time of an eddy of size z_{LDV} to completely sweep by; where z_{LDV} is the height of the LDV measurement volume above the 4th layer), data acquisition equipment (average time-between LDV data, and video framing speed), and mean time between successive ball motions.

The preferred value was determined by an estimation of the “signal-to-noise ratio (SNR)” associated with $\rho(\Delta t, \tau)$. If the maximum value of ρ is treated as the “signal” and the mean background ρ -value (for large τ 's) as the “noise,” then the SNR is computed from $\rho_{\max}/\rho_{\text{mean}}$. Table VI-2 shows the maximum, the background ρ and the SNR values for the three Δt values. Based on SNR the preferred value of Δt is 40,000 μs .

The sharp peak values of ρ reported in Table VI-2 are all at $\tau = 0$ (common to all the three Δt values) shows that the *number* of velocity measurements that occurred within 40000 μs prior to ball motion are highly correlated with ball motion. That is, the data rate prior to ball motion is strongly correlated to the movement of the ball, in fact the data rate was observed to become more than four times that of the mean value for the entire data set. Time series of few of the LDV velocity realizations plotted in time with corresponding ball motions is shown in Figure VI-7. For illustration the slit window width is also shown in Figure VI-7, and it is seen that a 40000 μs wide slit window width usually

includes one LDV data point. This is true for the entire data set, which suggests that the 90 LDV measurements that occur within the 40000 μs of the 120 ball motions are well-spread throughout the data set, and not lumped locally or associated only with just few of the 120 ball motions. This lends further credibility to the fact that the increase in data rate just prior to ball motion is not a chance occurrence.

The three Δt values investigated, viz., 40000, 100000, and 250000 μs are now compared with relevant time scales provided in Table VI-1. A value of 40000 μs was chosen, as it was approximately the smallest resolvable slit-window width for the current experiment (1 frame, or 1/30 sec corresponds to 33000 μs), and is also approximately of the order of the time it takes for an eddy of the height of the LDV measurement volume from the top of the 4th layer to completely sweep by at the speed of the mean velocity (34400 μs). The maximum value of 250000 μs was determined by the mean time between LDV data arrival (227000 μs). An intermediate value of 100000 μs was chosen mainly to examine the effect of Δt in the current analysis. The camera framing speed (33000 μs) is faster than the time between bursts⁽²⁾ (0.125 sec or 125000 μs) and lifetime of a burst⁽²⁾ (0.52 sec or 520000 μs), which means that the camera will record the LDV count that results from the given burst structure (if LDV data occurs). The bottom line is that the bursts are not occurring too rapidly for the camera framing speed to completely miss them. Occurrence of a burst does not guarantee a valid LDV measurement as it depends on the LDV seed distribution in water, which is a yet another random process. However, the time between LDV data gives a good estimate of how often a valid LDV data is

² It is cautioned that due to lack of rough wall data, smooth wall results have been used.

obtained (0.227 sec or 227000 μ s), which is of the same order as the time between bursts, and their lifetime. Again, the camera framing speed needs to be faster than the LDV data arrival speed, as too fast an LDV data rate will lead to the camera not recording all the LDV data counts. In addition, the image of the LDV data count will appear blurry in the video record, leading to possible misreading of the LDV data count during post-processing.

The increase in data rate observed just prior to ball movement is consistent with the velocity bias effect in LDV measurements. Faster moving fluid parcels are inherently measured more frequently by an LDV system. This is due to the fact that the arrival of the measurable seeds to the LDV measurement volume is not independent of the flow velocity that brings it to the measurement volume (see, Edwards, 1987). In the present situation this simply means that the velocities associated with the measured fluid events prior to ball motion must have higher velocities than fluid events that cause no ball motion. How else can the data rate simply increase four folds? And if the data rate increased four folds what are the characteristics of these fluid events? The last question will be explored (nature of fluid events, i.e., their mean velocities, rms values, etc.) shortly.

Tests to validate the remarkable results of the correlation analysis were conducted. The first question was whether the FORTRAN program developed for computing ρ performed properly. This was verified by computing the value of ρ for $\tau = 0$ through tedious hand calculations. The computer result agreed exactly with that given by hand calculation. Next, the entire LDV data record was shifted (artificially) in time by 4

seconds. The purpose was to test if the correlation, ρ would now occur at $\tau = 4$ sec, which it did.

The next test involved using a completely uncorrelated LDV data as the velocity record, and correlating it with the actual ball motion. The result showed no correlation at $\tau = 0$; moreover, the background ρ -value for this uncorrelated data set ($\rho = 24$) nearly matched the background value of the actual data set ($\rho = 22$). Thus, the conclusion is that the computer programs developed for the single ball analysis perform correctly, and that the result obtained is real.

To summarize, in the single ball experiment, the number of LDV velocity measurements increase four folds just prior to ball motion. Consistent with velocity bias effect, the mean velocity, and the associated rms values of fluid events measured by the LDV system are *expected* to be higher than their background levels. Tests on correlation between ball motion and “false” data yielded absolutely no correlation at any τ value, indicating that the observed correlation in the present case is real. The next section analyzes the fluid events that fall within the slit window of 40000 μ s, at various τ values.

VI-4-3 Characterization of Velocity Events Prior to Ball Motion

In the previous section it was clearly established that the number of fluid events measured by the LDV system simply increased four times before the ball motion. Here, the nature of these events are analyzed. It would be interesting to consider, for example, the mean velocity of fluid velocity events that precede ball motion, as a function of τ . Fluid events at large τ values occurred much before the ball motion, and hence are

expected to be irrelevant to the ball motion itself. Thus, the fluid velocities of these background events are expected to approach the corresponding values of the 16962 data points (or at least be scattered about them).

The general approach is to extract fluid velocity events that fall within a specified Δt value (here, it is 40000 μs) at various τ values, with $\tau = 0$ coinciding with beginning of ball motion. These LDV-measured velocity events at different τ values, but included in Δt , are called “local” events, as indicated in Figure VI-3. For every ball motion there is a batch of velocity events included in Δt , and located by τ (refer to Figure VI-3). For the 120 ball motions, 120 such batches assembled from the entire data set (referred to as the “global” set) of 16962 data points, form one set of velocity events. Various such sets, for different τ values, are considered here for further analysis. The range of τ values considered here extends from 0 to 2 seconds, expressed as an integral multiple of Δt . That is, τ varies from 0 to 2 seconds in steps of 40000 μs .

The end result of the analysis of the local velocity events is to capture some special features in velocity measurements just prior to ball motion. For example, the correlation between ball motion and number of LDV measurements reaches its peak value at $\tau = 0$. Consistent with the velocity bias effect in LDV measurements, it is reasonable to expect the streamwise mean velocity of all the local fluid velocity events ($\langle U_{\text{local}} \rangle$) that occur close to ball motion (at $\tau = 0$), and included in the slit window width, Δt of 40000 μs , to be greater than its global counterpart ($\langle U \rangle$). Similar trend may be expected of the local streamwise rms component (u'_{local}) as well (compared with the global u' value).

Figure VI-8 shows the variation of $\langle U_{\text{local}} \rangle$ with τ . The local streamwise mean velocity increases by about 40% at $t = 0$, entirely consistent with that predicted by the velocity bias effect. The normal component, $\langle W_{\text{local}} \rangle$ shown in Figure VI-9 does not show such a trend, and in fact, appears to be uncorrelated with ball motion. The streamwise rms quantity (u'_{local}), shown in Figure VI-10 increases by 23% compared to the global u'_{local} value, though the u' data scatter is much more than that seen in $\langle U_{\text{local}} \rangle$. The scatter in u'_{local} is largely due to the reduction in the number of data points that are used to compute u'_{local} . Table VI-3 summarizes the local and global values of different mean statistics constructed from the single ball data. The errors (from 95% confidence interval) presented in Table VI-3 clearly show that increases in the local $\langle U \rangle$, and u' values cannot be explained by statistical variability, and that they are significantly different from corresponding background values.

It is interesting to note that the procedure followed here to compute the rms values of the local events is somewhat analogous to the Variable-Interval-Time-Average or VITA method introduced by Blackwelder and Kaplan in 1976. The VITA method is one popular, single-point burst detection schemes. Occurrence of turbulent burst episodes are usually accompanied by sharp rise in local rms values, and VITA attempts to find the episodes by detecting the rise in rms values measured over short intervals of time (of the order of bursting time). The only motive behind comparing the present analysis with the VITA method was to point out that the approach is somewhat common, but beyond that the objectives of the two are completely different.

In the preceding sections, it was shown that an increase in data rate, local $\langle U \rangle$ and u' values occur just prior to ball motion. The next step is construct a methodology that would explain the role played by fluid velocity events that precede ball motion and help establish a connection between fluid velocity events and ball motion. An attempt is made to base the methodology on a stochastic concept (described in Chapters I and II), so that the chaotic nature of instantaneous velocities are included in describing ball motion.

The basic premise of the stochastic approach is that the instantaneous fluid quantities (specifically, velocities) are responsible in initiating sediment (glass ball) motion. A reasonable way to include the effects of instantaneous velocities in ball motion would be consider their probability distribution.

For the flow at hand there are several variables, whose probability distribution could be considered. However, it was reasoned that the choice of the relevant variable should be based on a basic physical equation such as force or moment balance, so that subsequent modeling of forces involved leads to physically plausible results. Based on numerous visual observations in this work, and Coleman's (1967) work, it was concluded that the glass ball's preferred motion is rolling. Thus, the balance of moments for a single, exposed ball placed atop a porous bed composed of identical spheres, is very important. This balance of moments for the case at hand was considered at the beginning of this chapter. Here the formulation of a new variable and its probability density function are considered.

Consider Equations VI-6 and VI-14. If it is assumed that Equations VI-6 and VI-14 are valid at every instant, then the velocities in these equations are the instantaneous

values and the probability density functions of the appropriate velocity components are relevant. As mentioned earlier, the purpose of introducing the instantaneous velocities as the relevant flow variables for the initiation of ball motion rather than steady, mean quantities goes back to the basic premise behind the stochastic approach. The idea is to relate the probability of occurrence of such instantaneous flow events with the probability of sediment (ball) entrainment. Therefore, the probability density function of the relevant flow variable is required in order to compute the probability of occurrence of such events through integration.

The probability density functions of individual velocity components are typically modeled well by a Gaussian distribution (except very close to the solid boundary in smooth wall flows, where the distribution is skewed). It can be shown that the square of a normally-distributed variable follows a gamma distribution. Thus, if U follows a Gaussian distribution, then U^2 follows a gamma distribution, and to an excellent approximation so does W^2 . From Equations VI-6 and VI-14 it is apparent that the square of the velocities is more relevant than the magnitudes of the velocity itself. Thus, the density function of a gamma distribution is considered:

$$p(x) = \frac{1}{\sqrt{2\pi}} x^{-0.5} e^{-\frac{x}{2}} \quad \text{[VI-17]}$$

The probability density function of U^2 is given by Equation VI-15, with $x = U^2$.

Now, reconsider Equation VI-6. The instantaneous values of U^2 and W^2 are expected to be well-modeled by a gamma distribution. However, their linear combination

shown in Equation VI-6 need not follow a gamma distribution as U and W are *not* independent. To resolve this problem, a new variable, φ ,

$$\varphi \equiv A_1 U^2 + A_2 W^2 \quad \text{[VI-18]}$$

is defined. From Equation VI-6 and the definition of φ , it is clear that sediment motion is theoretically possible when $\varphi \geq Cf_h$. The distribution of the new variable, φ , can be computed from experimental measurements. In constructing the distribution of φ it is convenient to normalize φ with respect to its ensemble mean, $\langle \varphi \rangle$, and use the normalized variable, ϕ , defined as,

$$\phi \equiv \frac{\varphi}{\langle \varphi \rangle} \quad \text{[VI-19]}$$

when forming the probability density function.

The next question is if some identifiable trend could be seen in the probability density of *local* ϕ events (*local* refers to the fluid velocity events that preceded ball motion and included in the 40000 μs slit window). For this the probability of occurrence of the variable ϕ is considered. The ϕ variable models the moment experienced by the single ball. The purpose of considering ϕ is to be able to link the probability of occurrence of “high” ϕ events with that of ball motion. The first step for this process is to model the probability density distribution of ϕ , $p(\phi)$, with a function.

From the experimental data, the probability of ϕ was created as follows. The minimum and maximum ϕ values were identified from the experimental data. This defined the range of ϕ . The ϕ range was then divided into bins of equal width. The number of ϕ events in each bin (histogram) was then computed from the experimental data, from which

$p(\phi)$ was estimated. Figure VI-12 shows the probability density distribution of ϕ for the global data. Now that $p(\phi)$ distribution for the global data has been generated, the question is whether the local velocity measurements have a $p(\phi)$ distribution that is different from the global distribution.

Creation of $p(\phi)$ for the local events similar to that for the global events was carried out and is presented in Figure VI-12. It was observed that for a given ϕ value, the probability of occurrence (estimated from experimental data) was higher than for the global data. To test if the increase in $p(\phi)$ was caused “artificially” due to an insufficient number of data (“only” 90), the following test was carried out.

Using a random number generating function, 90 random numbers were generated. Experimental data that corresponded to these random numbers were extracted and the $p(\phi)$ associated with these 90 events was computed (refer to Figure VI-13). This random number generation test was repeated several times to include any statistical variability associated with the process. Though quite a bit of scatter is seen in Figure VI-13 among various data, at $\phi > 1.5$, the $p(\phi)$ distribution of the local data appears to be clearly different and higher. This suggests that the relatively rarer high ϕ -events occur more frequently just prior to ball motion. The next step is to connect $p(\phi)$ with the probability of ball entrainment, P_E .

VI-4-4 Computing the Critical Condition

As stated in earlier chapters, the hypothesis is that the probability of occurrence of the relevant flow events determines the ball entrainment process. In this work the relevant

flow events are the velocity events. Information about the probability density functions of the instantaneous velocities and quantities, such as ϕ , was employed to compute the probability of occurrence of the relevant velocity events. This information was then used in conjunction with the ball entrainment probability, P_E , to estimate the critical condition.

Consider a probability density distribution shown in Figure VI-14 for an arbitrary variable η . Let η_{crit} denote the critical value, then the probability that an event greater than η_{crit} will occur is given by,

$$P = \int_{\eta_{crit}}^{\infty} p(\eta) d\eta \quad [\text{VI}\cdot\text{20}]$$

By the hypothesis stated before, P must be equal to P_E (for a simplified situation, see Chapter V, Equation V-3). Thus,

$$P_E = \int_{\eta_{crit}}^{\infty} p(\eta) d\eta \quad [\text{VI}\cdot\text{21}]$$

In the above equation, P_E was computed from the video part of the analysis, and $p(\eta)$, estimated from the LDV measurement. The integral shown in Equation VI-21 was evaluated numerically by using Mathematica for assumed values of η_{crit} , until it was satisfied. However, from the numerical integration point of view, a simpler procedure is possible when Equation VI-21 is rearranged:

$$\int_0^{\infty} p(\eta) d\eta = \int_0^{\eta_{crit}} p(\eta) d\eta + \underbrace{\int_{\eta_{crit}}^{\infty} p(\eta) d\eta}_{P_E} = 1 \quad [\text{VI}\cdot\text{22}]$$

Therefore,

$$P_E = 1 - \int_0^{\eta_{crit}} p(\eta) d\eta \quad \text{[VI-23]}$$

The above equation was solved using Mathematica to evaluate η_{crit} .

Replacing η with ϕ in Equation VI-23, one can estimate the value of ϕ_{crit} , if the functional form of $p(\phi)$ is known. A gamma function (see Equation VI-17) fits the experimental $p(\phi)$ distribution quite well. The gamma function was integrated using Mathematica to check if the value of ϕ_{crit} would be greater than the minimum theoretical moment, Cf_h (refer to Equation VI-6), required to initiate ball motion. The probability of ball entrainment, P_E (equal to 4.17×10^{-3}) was computed by knowing the average frequency of ball motion (every 30 seconds), and the time scale of large eddies ($H/U_B = 0.125$ sec). Solution to Equation VI-21 yielded a $\phi_{crit} = 1.7C f_h$. Interestingly, above a ϕ value of about 1.7, the $p(\phi)$ of the local data stands out (refer to Figure VI-12).

VI-4-5 Summary

The following are the important features of the single ball experiment:

1. Simultaneous use of video camera and 3-D LDV system to correlate ball motion and fluid velocity events measured upstream of a single isolated ball placed atop a porous bed composed of identical spheres.
2. Digital correlation technique, commonly called the photon correlation, implemented to the problem at hand
3. The correlation between ball motion and fluid events peak just prior to ball motion.

4. The number of fluid velocity events measured by the LDV system increase four folds just prior to ball motion.
5. The mean velocity, and the rms value of the fluid velocity events that occur just prior to ball motion are higher than the corresponding background values.
6. The normal velocity and its rms value do not appear to show any such trend.
7. A new variable, ϕ , that describes the moment of the ball, is formulated as the flow variable relevant to ball motion.
8. The probability distribution of ϕ , $p(\phi)$, of the local fluid velocity events appear to stand out from the background level for $\phi > 1.5$.
9. The value of ϕ_{crit} estimated from the probability of entrainment of the single ball, P_E , is 1.7 times the theoretical value required to move the ball.

Correlation of ball motion with bursts (identified by using the quadrant method) was not possible due to the nature of the Reynolds stress distribution with quadrants I and III events dominating, instead the usual quadrants II and IV. The global $\langle uw \rangle$ value is a positive number (i.e., momentum exchange is from the bed to the core region), mainly due to the increased momentum exchange caused by the deflection of the ball.

The experimental steps for the five sediment bed packing density tests are described next. The important differences between the single ball and the five sediment bed packing density tests are that in the latter, *no specific correlation* between sediment motion and velocity measurements were attempted to be established, and LDV measurements were carried out around roughness particles (lead balls) with *no bed mobility*.

VI-5 Sediment bed Packing Density Tests

The objective of the sediment bed packing density tests was to investigate the nature of fluid-sediment interaction through single point velocity measurements. Five packing density tests were carried out. Some of the salient features of the sediment bed packing density tests are repeated here.

The sediment packing densities in the five tests were designed to encompass three distinct rough wall flow types: the isolated, the wake-interference, and the skimming flow regimes (Morris, 1955). The flow condition of each of the packing density tests was such that the probability of sediment motion, P_E , was the same for all. The flow conditions for each of the five packing density tests obtained by imposing the equal- P_E criterion is shown in Table V-1. Determination of these flow conditions required a mobile 5th layer.

However, in order to obtain single point velocity measurements without any interference (such as a mobile glass ball rolling and blocking the laser beam) the mobile bed of glass balls needed to be immobilized. This was achieved by replacing the glass balls with lead balls of the same diameter. Detailed velocity measurements were carried out at several locations normal to the rough bed and at three streamwise locations relative to an individual ball in the packed bed. The LDV measurement locations are shown in Figure V-3, and are labeled A (directly above the top of the ball), B (located one ball diameter upstream from the center of the ball), and C (located one ball diameter downstream from the center of the ball). For the 70% packing density case alone, the number of streamwise locations was reduced to two, and are termed D (above the top of the ball) and E (in the cavity between the balls, one diameter upstream from the center of the ball). Several

single point measurements (called a data file) were carried out in each of the three locations. Each of the data files contains 3072 data points. Mean velocities, rms quantities, and other flow properties were computed from these 3072 data points.

The computed mean velocity, rms, and Reynolds shear stress profiles are used to describe the fluid-solid interaction. The fluid-solid interaction will be considered from two aspects:

1. In a given packing density case, how do the flow characteristics vary as the flow progresses toward a specific lead ball and crosses it?
2. How do the same flow characteristics compare with their counterparts in other packing density cases?

To be able to compare flow characteristics between two different packing density cases (hence, two different Reynolds number), appropriate normalization of the flow variables must be effected. All of the flow properties considered here are normalized with the friction velocity, u_* , calculated with \sqrt{gHs} . Here g is the local acceleration due to gravity, H is the water depth above the 4th layer (5th layer for the 70% case), and s is the slope of the flume. In fully-developed, uniform flows u_* can also be estimated from the linear stress profile as:

$$\underbrace{v \frac{\partial \langle U \rangle}{\partial z}}_{\approx 0} = \langle uw \rangle = u_*^2 \left(1 - \frac{z}{H} \right) \quad [\text{VI-24}]$$

where v is the kinematic viscosity of water. In rough wall flows, the uncertainty in u_* from Equation VI-24 computation is due to two reasons: (1) the location where $z = 0$ is

not known, and (2) the applicability of the above equation itself is questionable in the highly disturbed, non-homogeneous roughness sublayer. However, in the universal layer above the bed Equation VI-24 can be used to estimate u_* . Unfortunately, experimental limitations in the present tests restricted the number of measurements that could be obtained in the universal layer. The u_* determined from this method (by assuming that $z = 0.2d$ below the top of the 4th layer) generally tended to be less than that predicted with \sqrt{gHs} . Also, the experimentally obtained values of $\langle uw \rangle$ for curve fitting Equation VI-24 yielded both positive and negative values, especially in measurements above and downstream the ball. A similar effect has been observed by Fontaine and Deutsch (1996) for flow behind an obstacle mounted on a plane wall. They referred to the effect as the suppression of Reynolds shear stress. The crux of the above discussion is that the experimentally computed Reynolds shear stress measurements was found to be location-dependent, especially in the low packing density cases and hence, was not used in estimating u_* ; \sqrt{gHs} was employed instead.

VI-5.1 Comparison of Different Flow Regimes

Figures VI-15 to VI-39 show normalized profiles of mean velocities, rms quantities, and the Reynolds stress. All of the normalization was done with u_* . From a fluid-solid interaction point of view, the plots are quite enlightening. The first observation is that different variables show varying degrees of sensitivity to packing density. The streamwise velocity statistics, the mean and the rms velocities, seem to be more insensitive than the other variables, the normal mean and rms velocities, and the Reynolds stress.

The flow behavior changes from the 2% to 70% case are rather remarkable in all the quantities. Clearly, at 2% packing, the flow “sees” individual balls. This can be seen clearly when the “undisturbed” trend seen in location B is compared with the profiles of locations A and C. Thus, the disturbance created by particles placed upstream of location A, seemed to have died by the time flow reaches location B. However, at location A the flow is deflected up (positive normal direction) by the lead ball, and the wake behind the ball extends at least for one ball diameter, as revealed by the profiles in location C. The average distance between balls in the 2% case is about 6 ball diameters. Thus, it is reasonable to assume that the flow recovers before it traverses a distance of 6 ball diameters.

In the next packing case, 20% packing density, the flow variables reveal less effect due to *individual* balls, when compared to the 2% case. By this it is meant that the lead balls placed on the 5th layer are beginning to behave more “collectively” rather than individually. The collective (or grouped) behavior continues to increase as the packing density is increased further.

The distinct features of each of the three regimes (Morris, 1955) defined based on the packing density are brought forth most clearly by the Reynolds stress profile. Due to the deflection caused by the ball, and the creation of downstream wake, the Reynolds stress becomes positive at location A in all of the cases, except the 70%. In the 2% case the Reynolds stress profile is similar somewhat at locations A and C. This similarity between A and C decreases for the 20% case. In the 35% case, Reynolds stress profile at C resembles that at B, rather than that at A. The reason is that the C location is

immediately upstream of the next downstream ball. The flow differences that existed at low packing conditions at the “upstream” and “downstream” locations tend to vanish. In other words, if the downstream flow behavior at the 2% packing density is interpreted as that due to the ball’s presence, then at higher packing conditions, the effect of the ball’s presence is greatly minimized.

VI-5-2 Roughness Sublayer

From Figures VI-15 to VI-39, the roughness sublayer extent could be estimated in terms of z/d . This estimation is largely based on visual judgment, as a quantitative approach to defining the roughness sublayer does not seem to exist. The roughness sublayer extent is a function of the sediment bed packing density, and flow Reynolds number. Since both vary in the tests conducted in this work, the effect of packing density on roughness sublayer extent (with Re constant) or the effect of Re on roughness sublayer extent for a given packing condition cannot be evaluated. However, for the given flow situation, the roughness sublayer extent can still be judged (with no attempt at comparing the results of different packing density cases).

The roughness sublayer extent for different types of roughnesses (wheat field, vegetation canopies, sand deserts, spheres, cubes, etc.) are reported by Raupach et al (1991). They conclude that the roughness sublayer extends from $2h$ to $5h$, where h is the height of the roughness element. Raupach et al take the reference plane (where $z = 0$) as the ground on which the roughness element is located; h , then, is measured from the

reference plane. Figure VI-40 shows Raupach et al.'s reference plane and the expected range of roughness sublayer extent.

For the roughwall at hand has multiple layers of balls. The value of h for such a case is not clearly defined. Here, h is taken as the ball diameter, d . Also, the reference plane is taken as the top of the 4th layer balls, as they provide the support for the 5th layer balls. Based on these values of h and reference plane location, the roughness sublayer delineated by different flow variables at different packing densities, was determined. The results are summarized in Table VI-4.

Next, individual profile variations about a ball are considered. The purpose is to provide a qualitative description of the profiles shown in Figure VI-15 to VI-39. For the following discussion, the behavior of individual variables at the five different packing densities and at the three locations, A, B and C (two for the 70% case) are considered.

VI-5-3 Streamwise Velocity Profiles

The mean streamwise velocity profiles, normalized with u_* , for the five packing density cases are considered here. Figure VI-15 shows $\langle U \rangle / u_*$ for the 2% case. This case, based on Morris' (1955) criterion, belongs to the isolated ball regime. It can be seen that at location B, the flow streamwise component has not yet been affected by the presence of the ball located upstream. However, once the flow reaches the top of the ball a velocity gradient is clearly observed, with the flow speed slowing down as the solid surface of the ball is approached. At the downstream section of the ball, the flow slows

down considerably, forming a fluid layer that has nearly zero streamwise velocity at a z/d value of 0.6.

At 20% packing density, there are simply more balls and the flow is the wake-interference regime. Behavior very similar to the 2% case is seen here too (Figure VI-16). At location B, the flow sees no effect of the ball upstream and at location A, a sharp velocity gradient is seen. Location C produces a mean velocity distribution that has somewhat of a V-shape. The V shape exists only behind the ball, and beyond z/d value of 0.9 (top of the 5th layer) the profile merges with those measured at locations A and B. It is curious that the minimum U-velocity value measured downstream of the ball again occurs at an approximate z/d value of 0.6. However, the velocity gradient present behind the ball is much more severe than the 2% case.

The velocity profile shown in Figure VI-17 for the 35% case is literally the same at the three locations, A, B and C. Even though the location of the very first LDV measurement, 0.0075 inch (191 μm) above the top of the ball, was the same as that for the 2% case, the velocity gradient was much steeper (due to higher Reynolds number) here in comparison to the 2% case. That is one of the reasons the velocity gradients captured in the 2% and 20% case was not captured here. At locations B and C, the effect due to the presence of individual roughnesses seem to be so localized that they were not captured by the LDV measurements of the U-velocity.

In the 50% packing density case the first LDV measurement point was at 0.005 inch (127 μm) from top of the ball. This distance is closer than in the 35% case, and the U-velocity gradient above the ball surface becomes noticeable (see Figure VI-18). As with

the 35% case, all of the three profiles overlap through most of the flow depth. In the 70% case, even the small differences between the three velocity profiles noticed in the 50% case, become much less pronounced. The two profiles for the 70% case, shown in Figure VI-19, literally overlap almost perfectly throughout the entire flow depth.

VI-5-4 Normal Velocity Profiles

As with the streamwise component, the normal velocity is normalized with u_* as well. Based on Figure VI-20 for the 2% case, it appears that the normal velocity component exhibits more scatter than the streamwise component. However, the y-axis range extends from -1 to 2; hence, the differences may be magnified. As before, at location B, the presence of the upstream ball is not seen. However, at location A, the velocity measurements do show upward deflection of the flow, as the normal velocity increases here. Downstream of the ball the normal velocity reaches the maximum value approximately at the ball centerline, while right at the top of the ball, it reaches its minimum. The minimum value may be suggestive of flow toward the lower pressure region of the downstream wake (almost like an expansion wave). Compared to the streamwise component, the normal values at the three locations do not quite overlap as well. Thus, based on the normal values, one would be tempted to conclude that the roughness sublayer extent has not yet been reached.

Similar behavior is seen for the 20% case as well. It is interesting to note that the maximum normal velocity for location A occurs again at a z/d value of 1, and the values for the 2% and 20% cases are approximately equal. For the downstream location, C, the

behavior of the 20% case again resembles that for the 2% case. But the velocities measured at locations A, B and C do come together better than they do for the 2% case at similar z/d values.

The 35% case normal velocity profile shown in Figure VI-22 ranges from -0.5 to 0. Due to such a small range the differences among the velocity profiles measured at locations A, B, and C appear to be more spread out than in other cases. However, it is curious that all the three have the similar trends. The differences in flow velocity that previously arose because of individual balls seem to be getting washed down now, as “downstream” of a ball now is the “upstream” of its neighbor. In other words, the flow disturbances created by a ball do not die out completely before the flow encounters the next ball.

The 50% case normal velocity profile shown in Figure VI-23 shows a steep velocity gradient for location A. This behavior is captured essentially because LDV velocity measurements could be made closer to the ball surface than in the other packing cases. The observed steep velocity gradient occurs in a distance of less than 100 μm . The behavior of the velocity profile at locations B and C appear to be different from the 35% case. This may be due to the effect of local geometry (effect of surrounding balls). In the 70% case, the difference of the normal velocity profile measured over the two locations seem to have similar trend, though the individual values are quite apart. It is also not clear why the normal mean velocity value shows an increasing trend.

VI-5-5 Root-Mean-Square Velocity Profiles

In the 2% case the U-velocity rms values (u') at location B seem to be unaffected by the presence of the ball located one ball diameter downstream (see Figure VI-25). At z/d values greater than 1.4, u' values at locations A, B and C start overlapping and reach u'/u_* values of 2. Downstream of the ball, u' reaches its minimum and maximum values at approximate z/d values of 0.6 (where $\langle U \rangle$ reaches its minimum as well) and 0.9, respectively.

The high values of u' seen in the 20% case, shown in Figure VI-26, may be due to some local roughness effect, as a similar effect was not observed in any other case. Here again u'/u_* values (though decreasing as z/d increases) are higher than the usually-reported values of 2. The 35% case (Figure VI-27) u'/u_* values at locations A, B and C literally overlap throughout, and show a trend that is similar to that observed over the smooth wall (see, Nezu and Nakagawa, 1993). The 50% case shows a trend similar to the 35% case in the sense that u'/u_* reach similar values in both cases for $z/d > 3$. In the 70% case even near the roughness layer, the effect of individual roughness cannot be seen.

The normal velocity component rms profiles are shown in Figures VI-30 to VI-34. In the 2% case w'/u_* reduces steeply at location A, as the surface of the ball is approached. Similar behavior is noticed in 20%, 35% and 50% cases at location A. Direct comparison between the above four packing cases and the 70% case should be done carefully, as in the four cases, z/d equal to 0 corresponds to the top of the 4th layer, while for the 70% case z/d equal to 0 corresponds to the 5th layer top. Thus, the increase of w'/u_* seen in the 70% case occurs far away from the roughness surface. LDV

measurements could not be located any closer than $0.5d$ from the ball surface, due to unacceptable level of noise detected in the signals. For locations behind the ball (i.e., C), and even for above the ball (A), w'/u_* increases in all the cases, except the 50% case. Again, the 50% case measurement might have been affected by local roughness influence. In all cases, at distances far away from the roughness layer w'/u_* approaches a value of 1, which corresponds to the smooth wall value (see Nezu and Nakagawa, 1993).

VI-5-6 Profile of the Reynolds Shear Stress

The Reynolds shear stress term ($\langle uw \rangle$) shows more striking and characteristic features than any other flow property discussed thus far. Reynolds shear stress at location B shows little influence of the presence of the downstream ball. However, at locations A and C, the Reynolds shear stress decreases (i.e., becomes positive; this will be obvious if $-\langle uw \rangle$ is plotted instead of $\langle uw \rangle$). At location A, the decrease of the term occurs close to the ball surface and probably caused by the flow deflection caused by the ball's presence. This upward flow deflection induces a forced U-momentum transfer in the positive W direction (upward). At farther distances from the ball, the term becomes negative and settles back to its value at location B. Downstream of the ball the term decreases in the wake, reaches its peak value right at the top of the 5th layer ($z/d \sim 0.9$), and merges with other measurements at a z/d value of 1.2.

Similar decrease in the Reynolds shear term was reported by Fontaine and Deutsch (1996). They measured this effect behind a protrusion, 16.4 wall units⁽³⁾ long, located on

³ 1 wall unit = v/u_* , where u_* is the friction velocity and v is the fluid kinematic viscosity.

the smooth bottom wall of an acrylic pipe. The main motive behind their work was to investigate the effect of disturbances in the near-wall region on burst generation in a turbulent boundary layer.

It is interesting to note that a similar phenomenon occurs here where the particles are much bigger (about 232 wall units⁽⁴⁾ for the 2% case). Fontaine and Deutsch (1996) discuss the formation of a pair of counter rotating vortices that form at the edge of the protrusion that are sporadically shed and convected downstream. Schlichting (1979) measured two counter rotating vortices $10d$ ($d = 4$ mm) downstream of a row of spheres placed on a smooth wall in a turbulent boundary layer. In this work, the measurements at location C suggest a zone of fluid stagnation, and re-circulation, but the formation of vortices themselves was not verified.

The Reynolds shear stress shows a decreasing trend in the 20% case at locations C and A. However, in the 35% and 50% cases, similar trends are not seen probably because of local roughness effects. It is interesting that at large z/d values the Reynolds shear stress term decreases similar to that observed in smooth wall flows (see Nezu and Nakagawa, 1993). The 70% case Reynolds shear term profile is similar to the smooth wall profile. Effects of roughness, if any, were not detected by the LDV measurements.

In summary, the profiles described here show that in the 2% case the flow seems to “feel” the presence of individual balls more than in any other packing case. The downstream distance through which such disturbance exists was not measured in this work. However, based on measurements made at location B, it is possible to surmise that

⁴ 1 wall unit for the 2% case is $34.5 \mu\text{m}$, where $u_* = 0.0313$ m/sec, and $\nu = 1.081 \times 10^{-6}$ m²/sec.

such disturbances do not propagate for more than 6 ball diameters (mean distance between balls in the 2% case). Based on this observation, Morris' (1955) and Lee and Soliman's (1977) categorization of the 2% case as the isolated regime appears to be correct.

Moreover, downstream of the ball, evidence of a re-circulation region exists, with the fluid layer in line with the center of the ball nearly stagnant. Suppression of the Reynolds shear stress term observed by Fontaine and Deutsch (1996) for small wall-mounted protrusions, is observed here as well. As packing density is increased influence of individual balls seem to loose importance in terms of affecting the flow characteristics. This behavior becomes stronger for the 35% and 50% cases when compared to the 20% case. In the 20%, and 35% cases, the LDV measurement volume could not be traversed close enough to the balls to measure local flow disturbances, if any. The 70% case flow behavior is similar to that of a fully-developed, smooth wall flow.

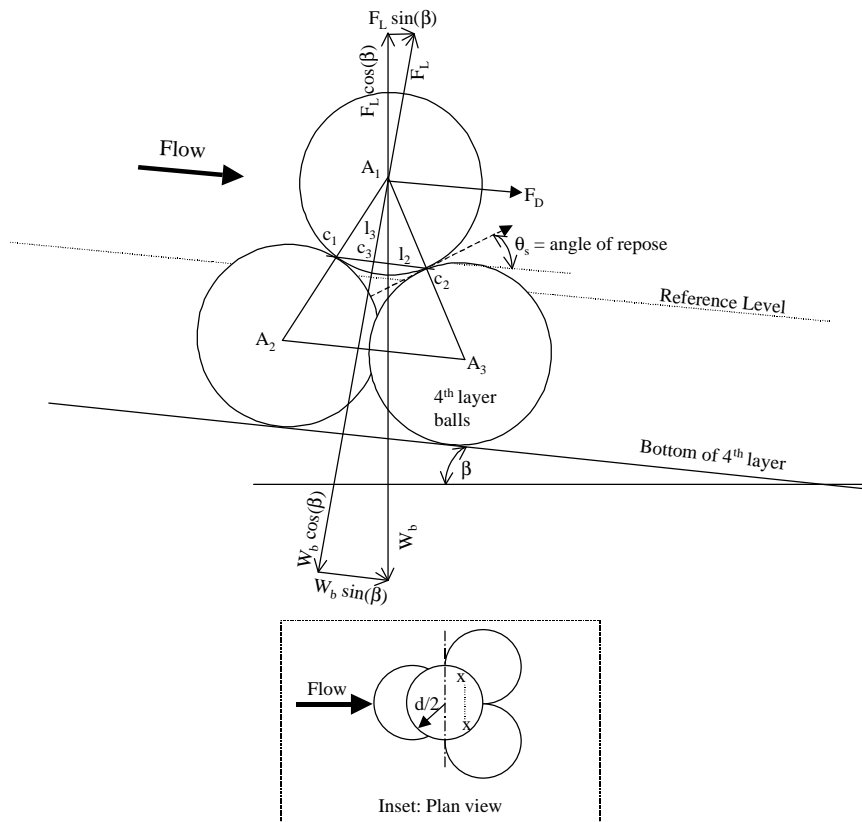


Figure VI.1. Forces exerted on a single, exposed ball placed atop identical spheres.

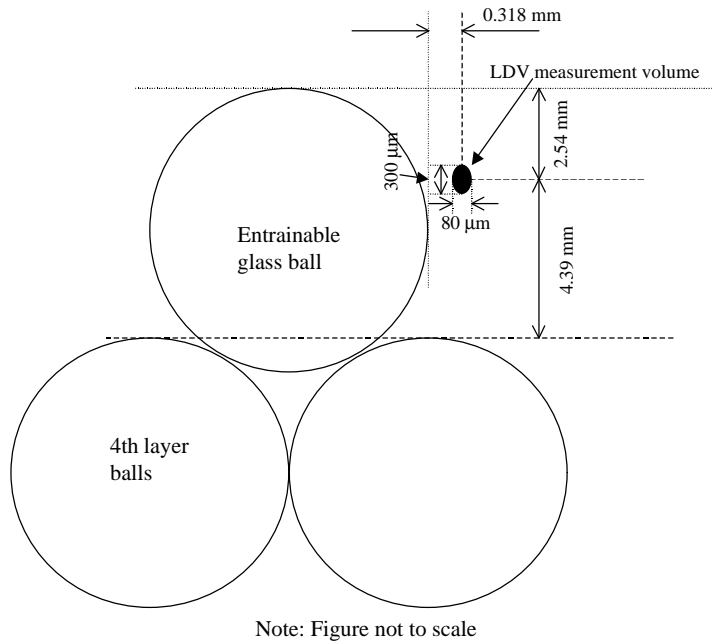


Figure VI-2. LDV measurement location for the single ball experiment.

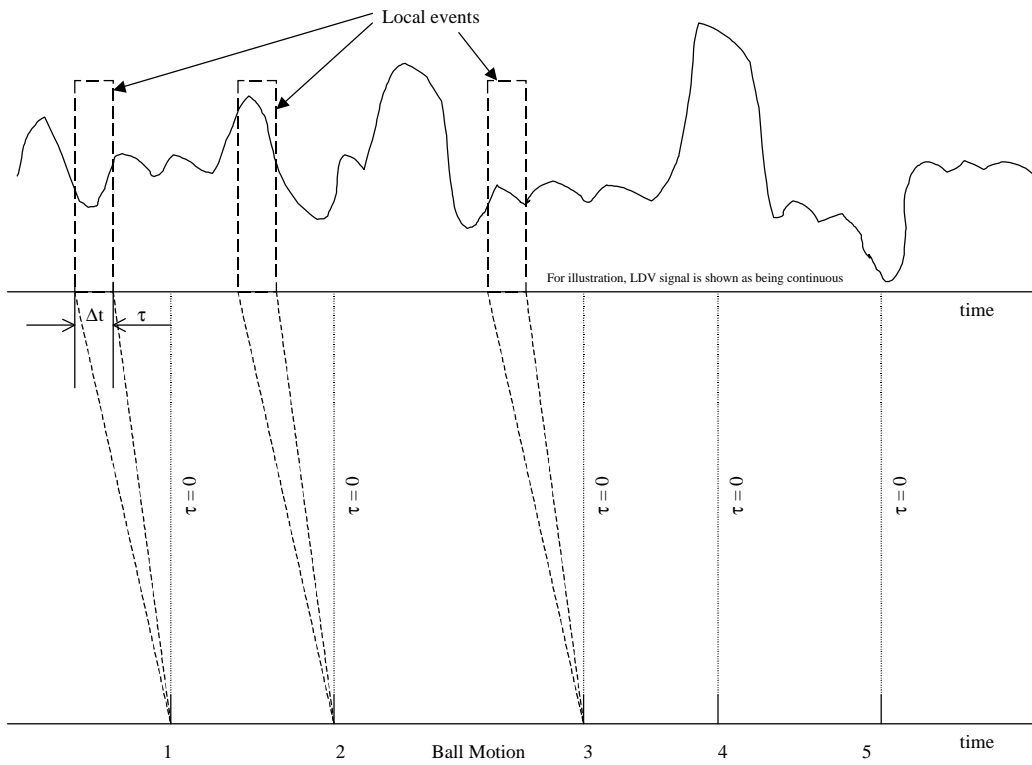


Figure VI.3. Time series representation of the LDV velocity signals and ball motions.

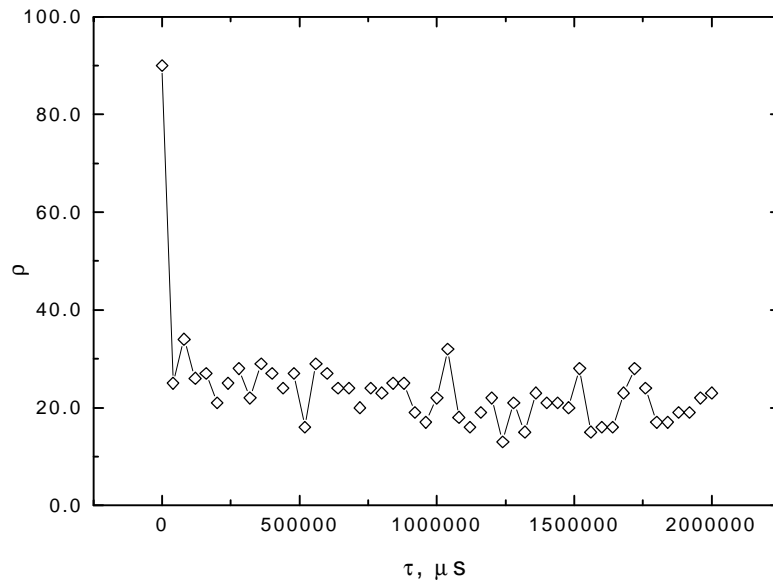


Figure VI.4. Variation of ρ with τ for $\Delta t = 40000 \mu\text{s}$.

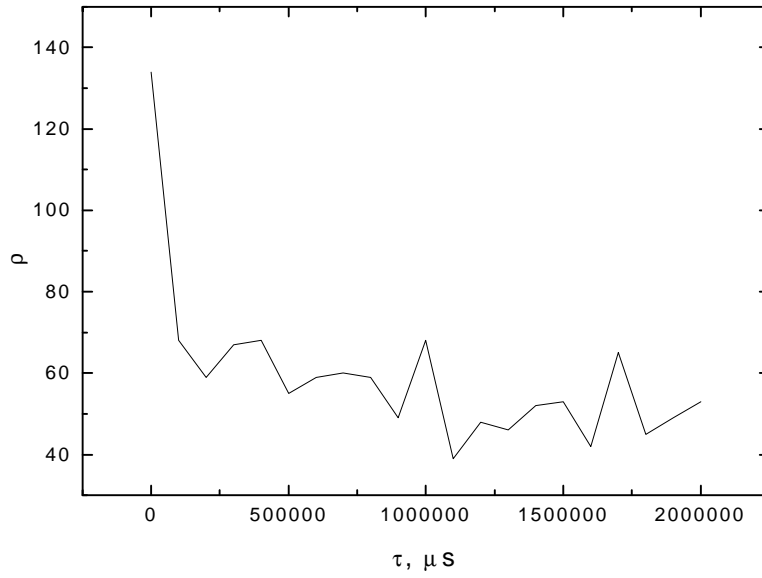


Figure VI.5. Variation of ρ with τ for $\Delta t = 100000 \mu\text{s}$.

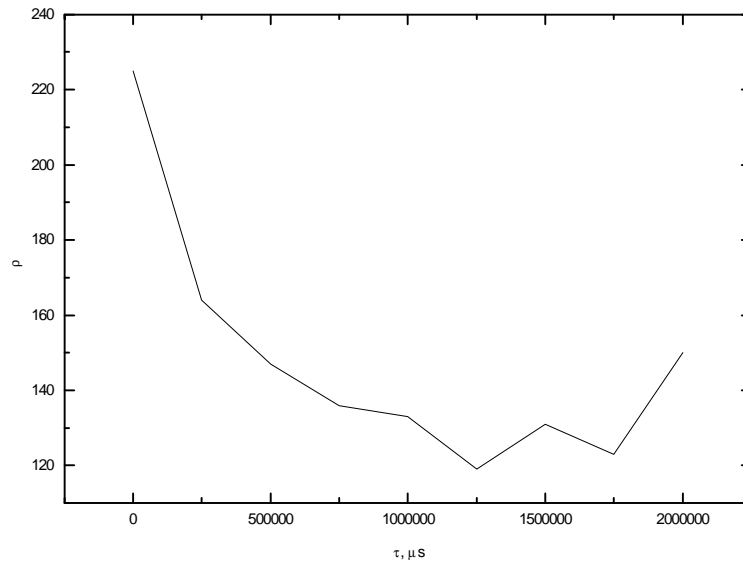


Figure VI-6. Variation of ρ with τ for $\Delta t = 250000 \mu\text{s}$.

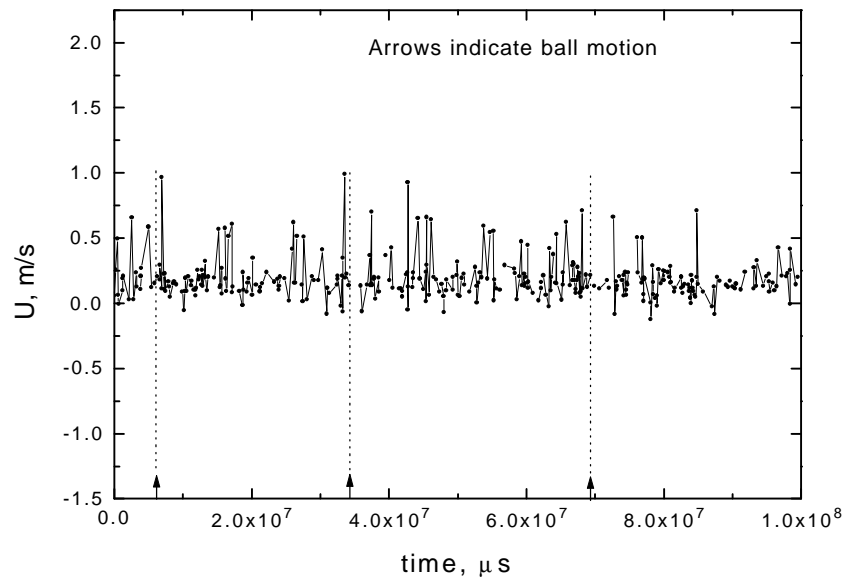


Figure VI.7. Time series representation of ball motion and velocity.

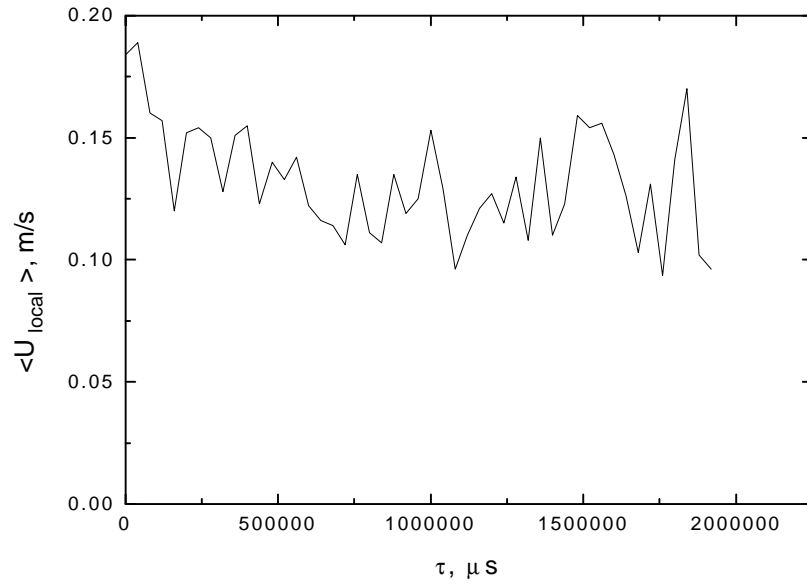


Figure VI-8. Variation of local streamwise mean velocity with τ , $\Delta t = 40000 \mu\text{s}$.

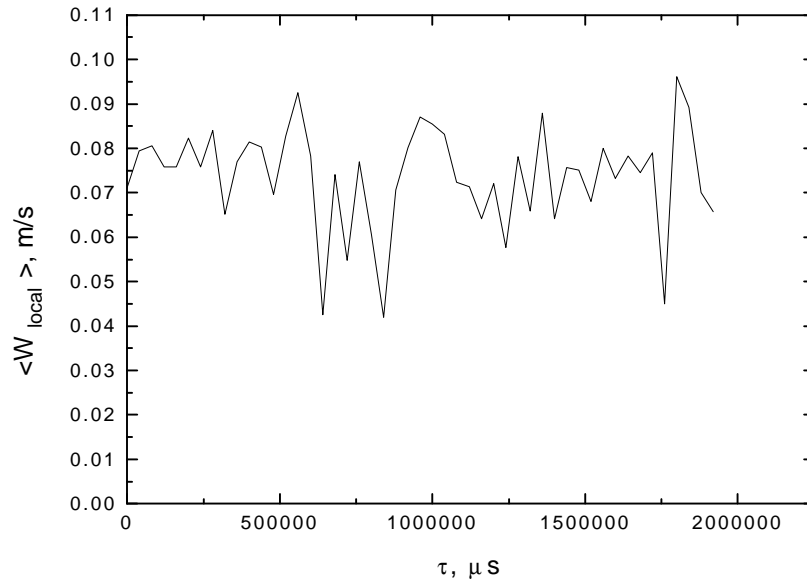


Figure VI-9. Variation of local normal mean velocity with τ , $\Delta t = 40000 \mu\text{s}$.

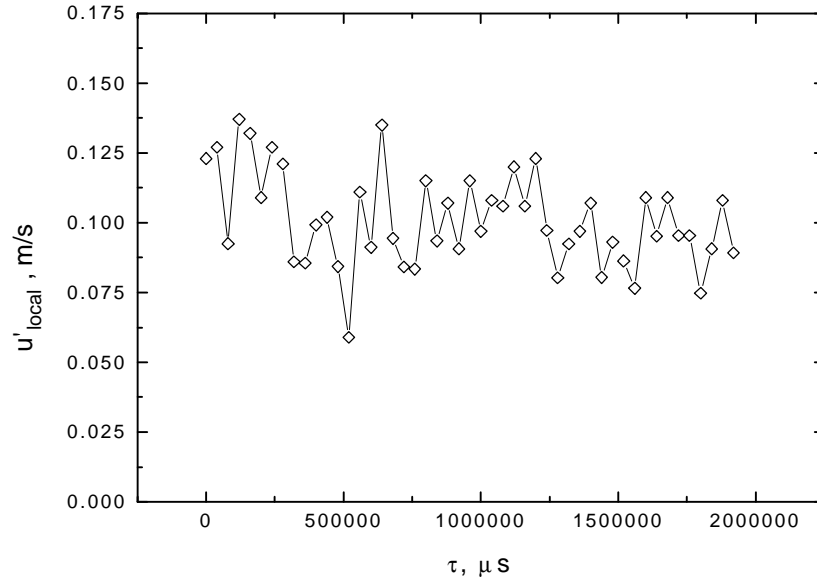


Figure VI-10. Variation of local streamwise rms velocity with τ , $\Delta t = 40000 \mu\text{s}$.

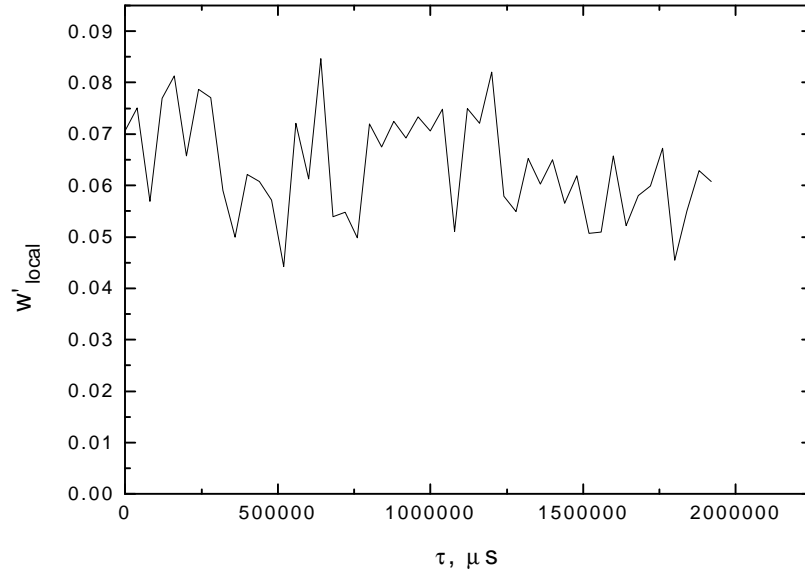


Figure VI-11. Variation of local normal rms velocity with τ , $\Delta t = 40000 \mu s$.

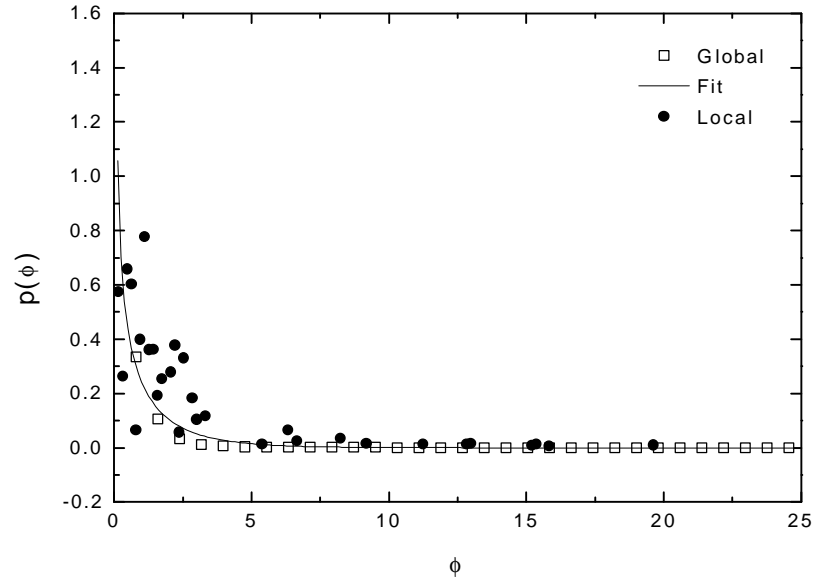


Figure VI-12. Probability density function of ϕ for the global and local data.

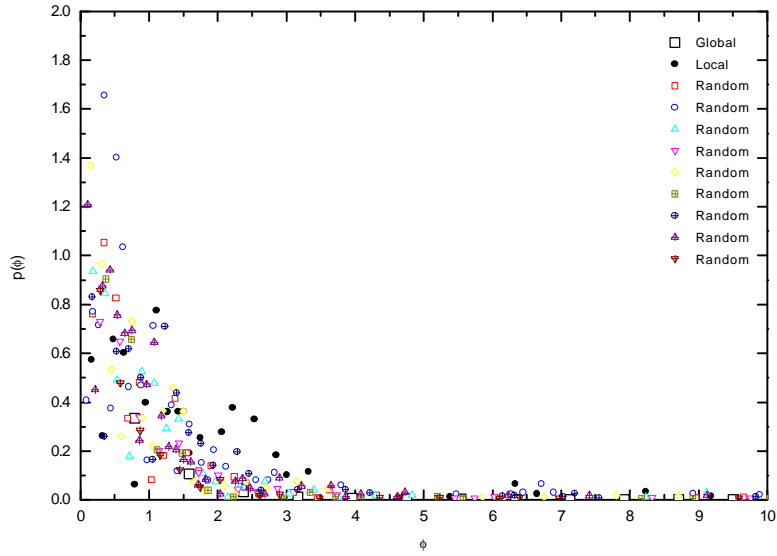


Figure VI-13. Probability density function of ϕ for the global, local, and randomly selected data.

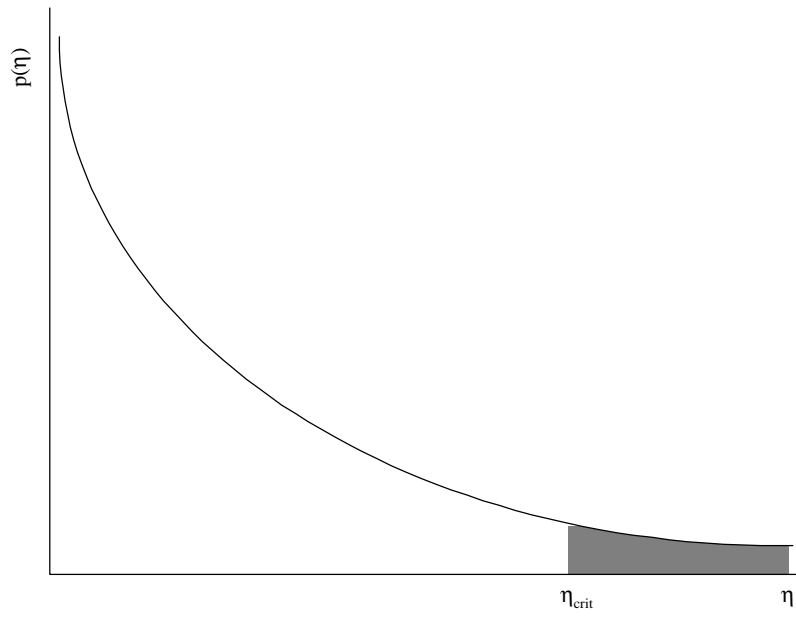


Figure VI-14. Schematic of probability density function for an arbitrary variable, η .

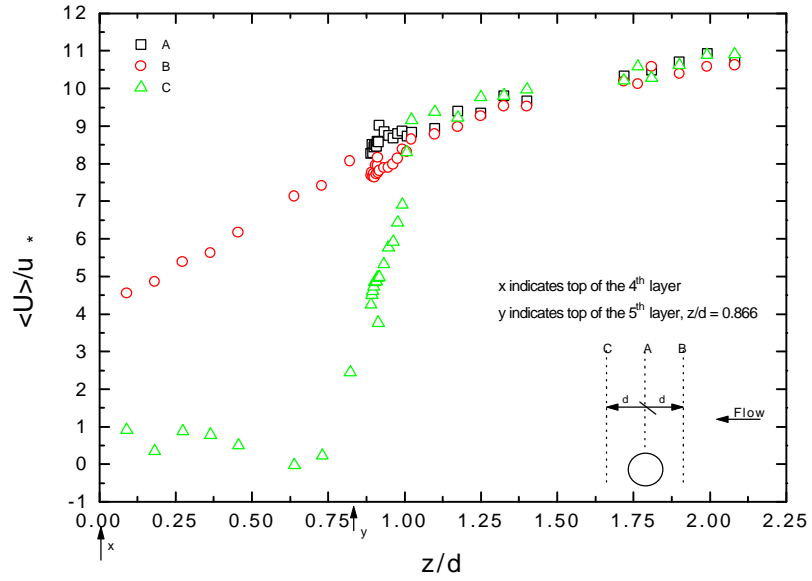


Figure VI-15. Variation of streamwise mean velocity for the 2% sediment bed packing density case.

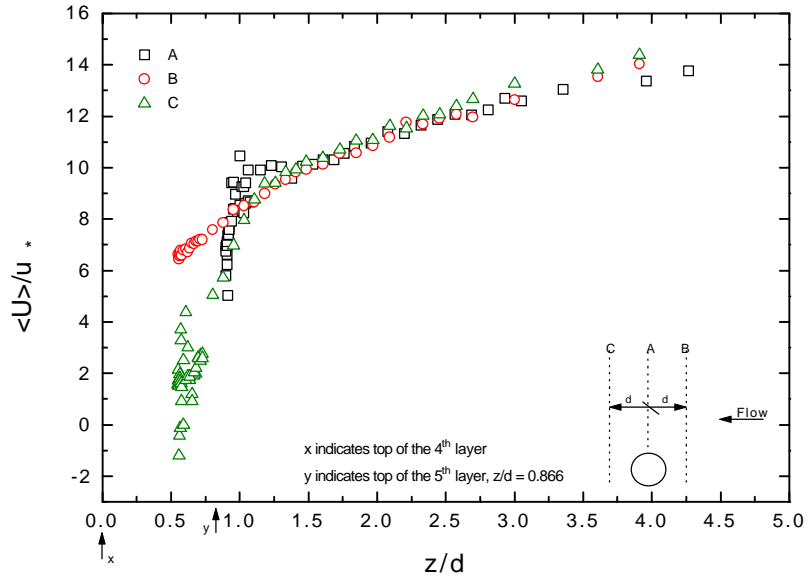


Figure VI-16. Variation of streamwise mean velocity for the 20% sediment bed packing density case.

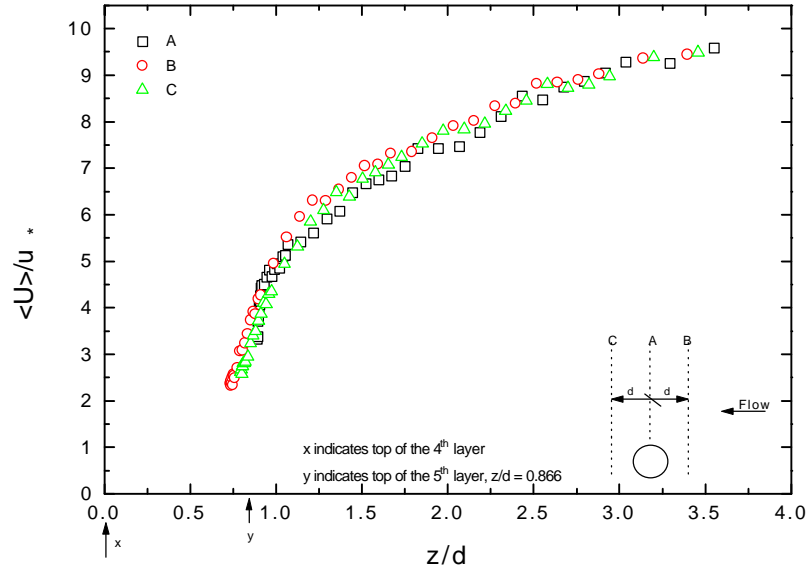


Figure VI-17. Variation of streamwise mean velocity for the 35% sediment bed packing density case.

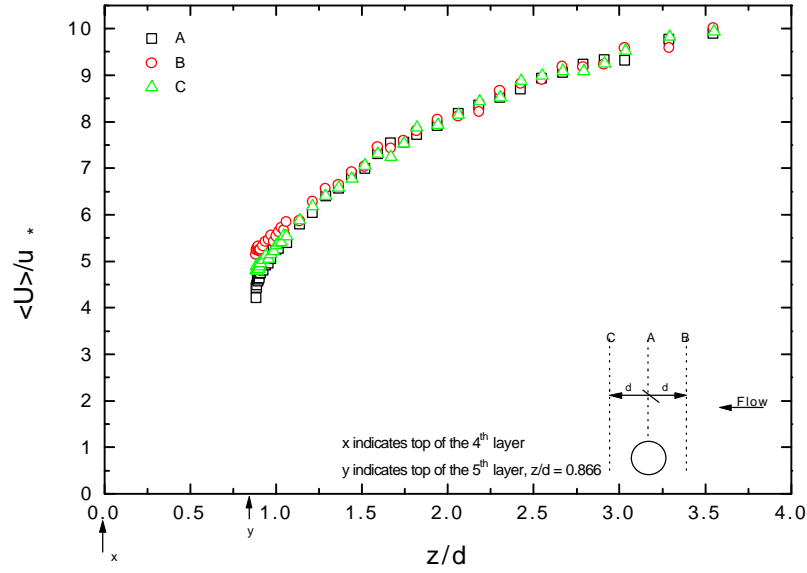


Figure VI-18. Variation of streamwise mean velocity for the 50% sediment bed packing density case.

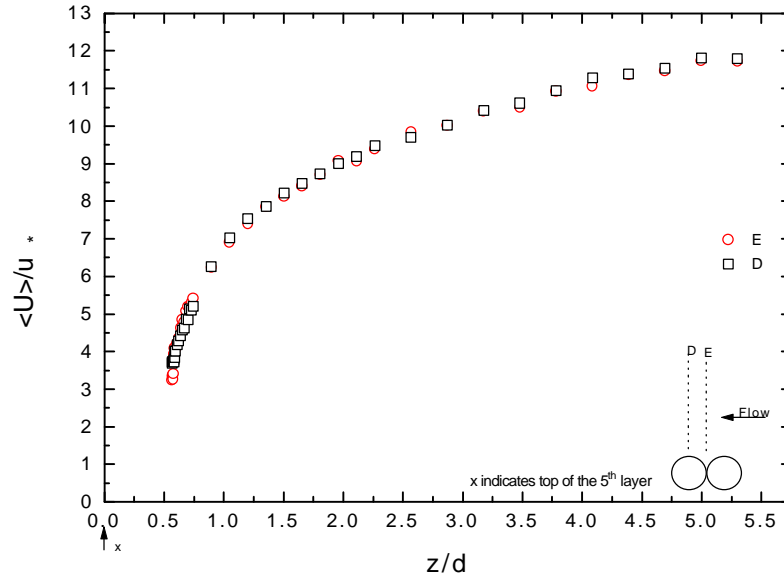


Figure VI-19. Variation of streamwise mean velocity for the 70% sediment bed packing density case.

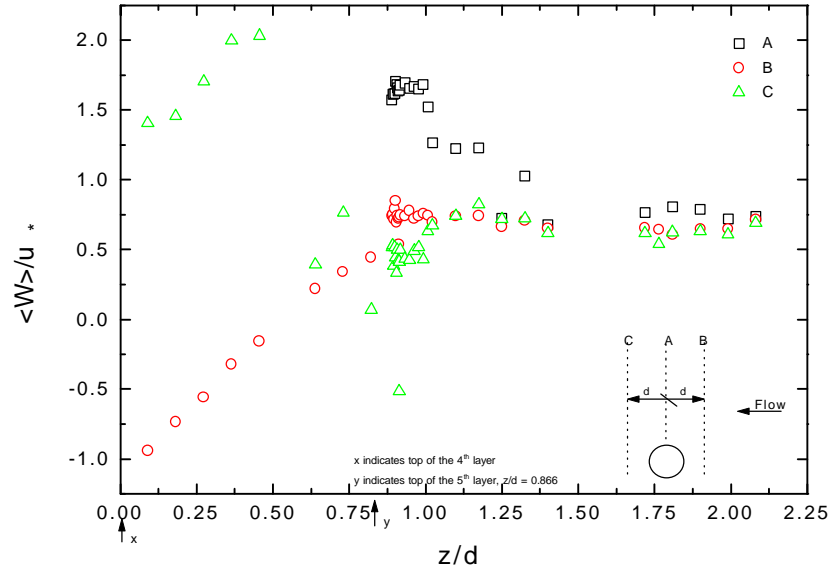


Figure VI-20. Variation of normal mean velocity for the 2% sediment bed packing density case.

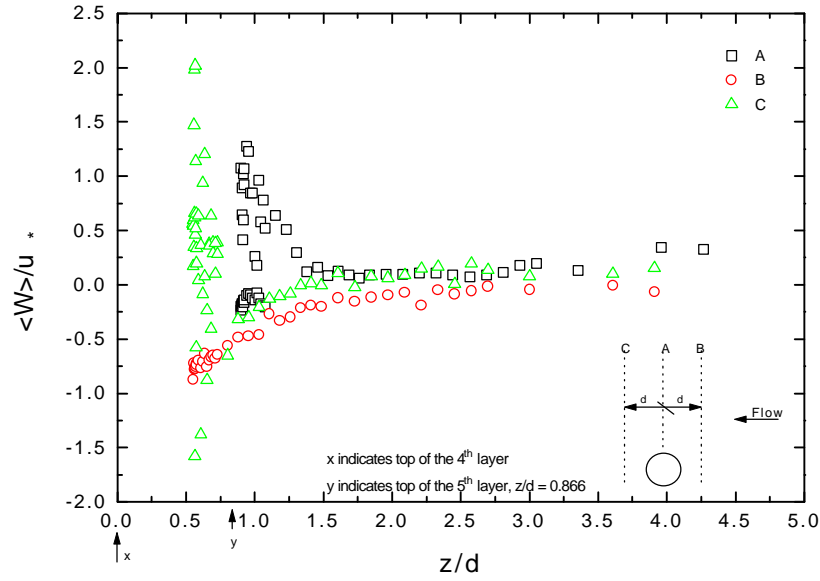


Figure VI-21. Variation of normal mean velocity for the 20% sediment bed packing density case.

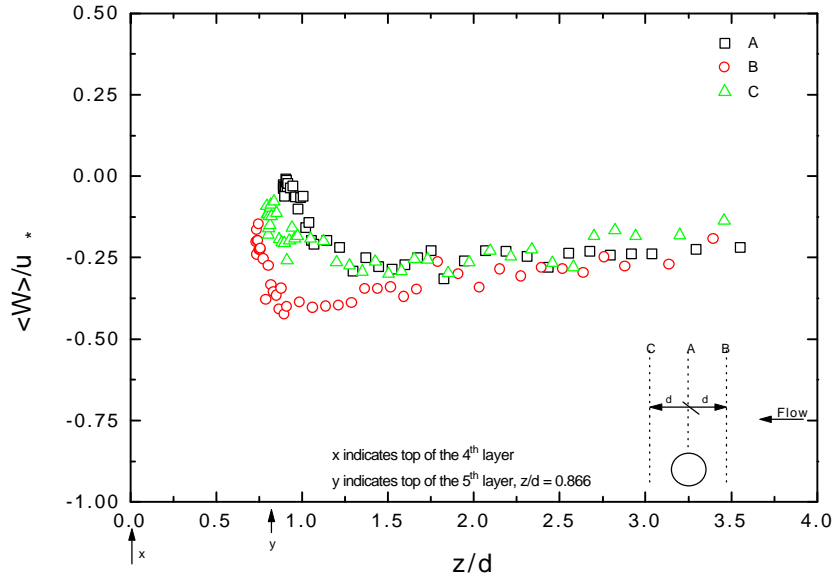


Figure VI.22. Variation of normal mean velocity for the 35% sediment bed packing density case.

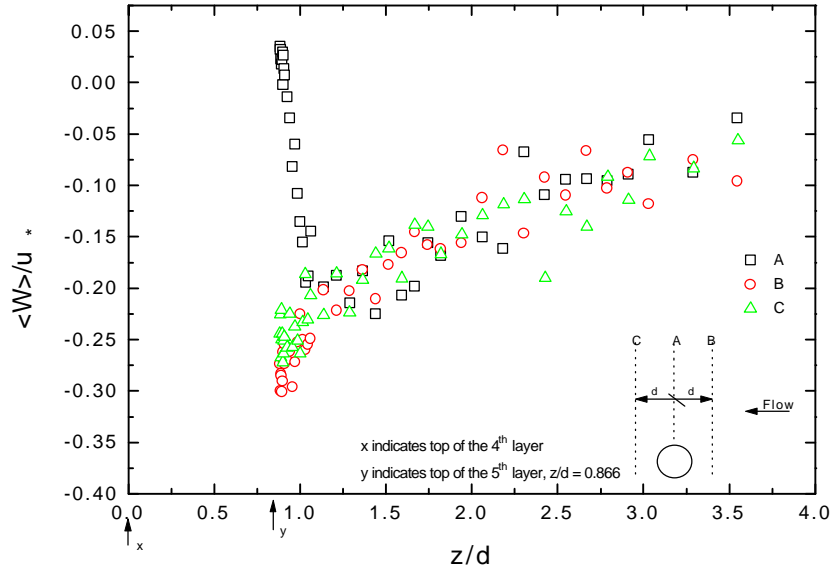


Figure VI.23. Variation of normal mean velocity for the 50% sediment bed packing density case.

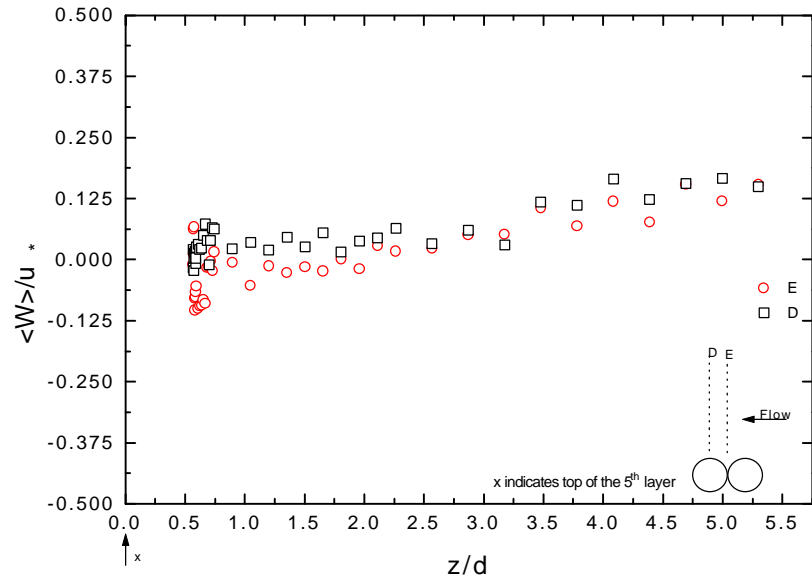


Figure VI.24. Variation of normal mean velocity for the 70% sediment bed packing density case.

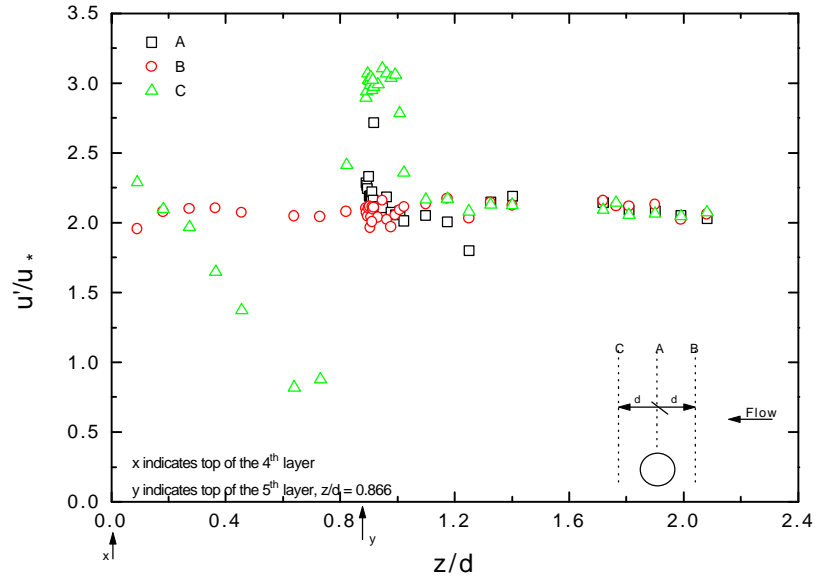


Figure VI-25. Variation of streamwise rms velocity for the 2% sediment bed packing density case.

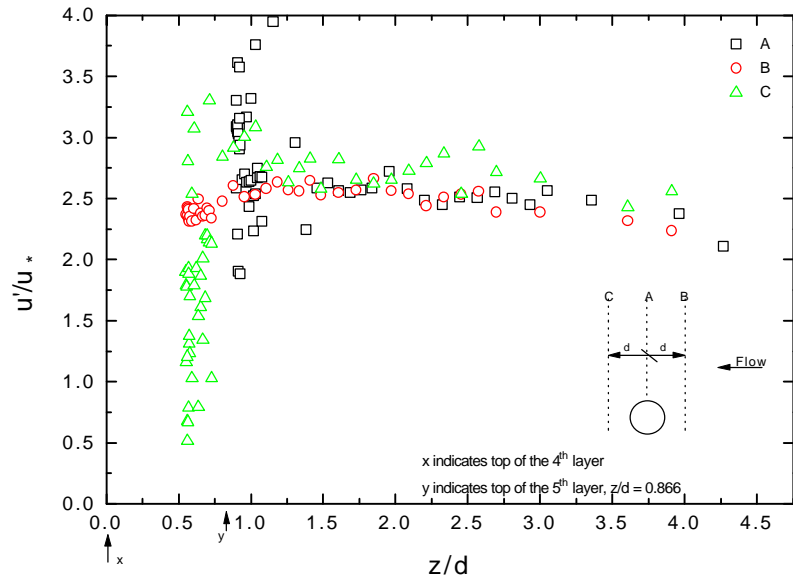


Figure VI-26. Variation of streamwise rms velocity for the 20% sediment bed packing density case.

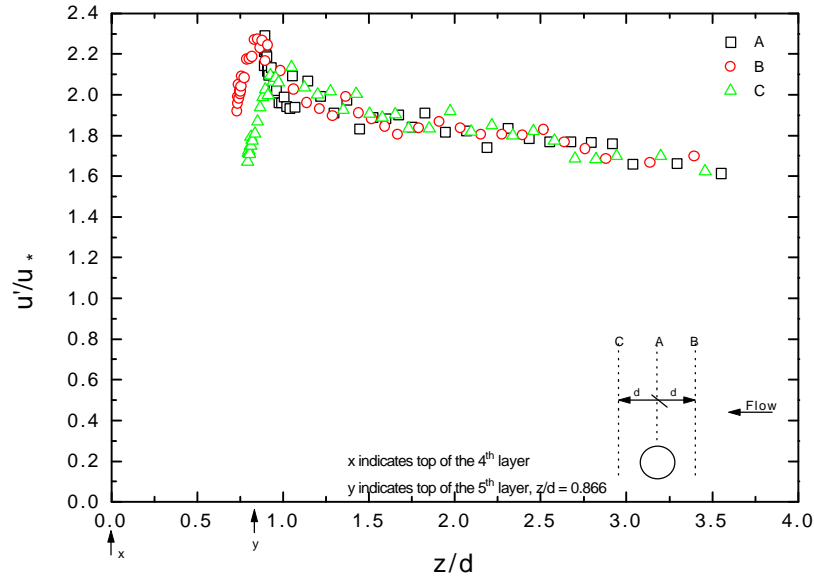


Figure VI-27. Variation of streamwise rms velocity for the 35% sediment bed packing density case.

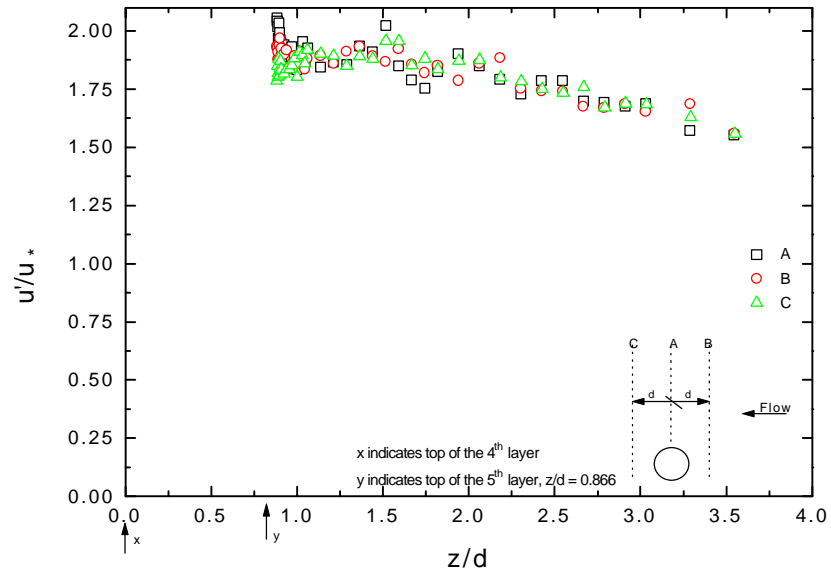


Figure VI-28. Variation of streamwise rms velocity for the 50% sediment bed packing density case.

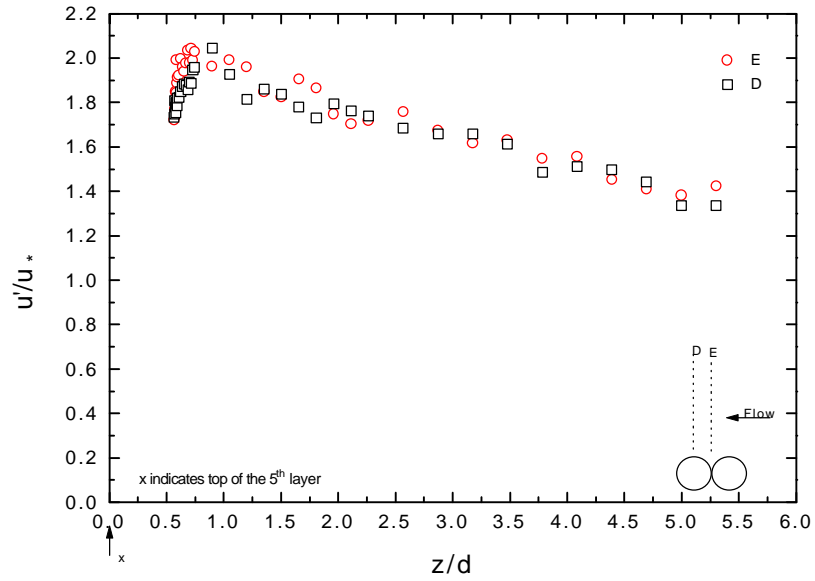


Figure VI-29. Variation of streamwise rms velocity for the 70% sediment bed packing density case.

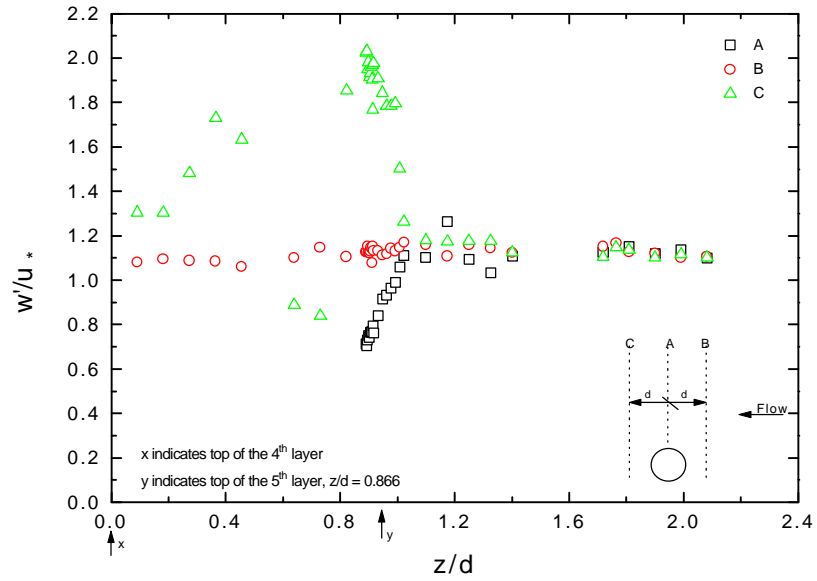


Figure VI-30. Variation of normal rms velocity for the 2% sediment bed packing density case.

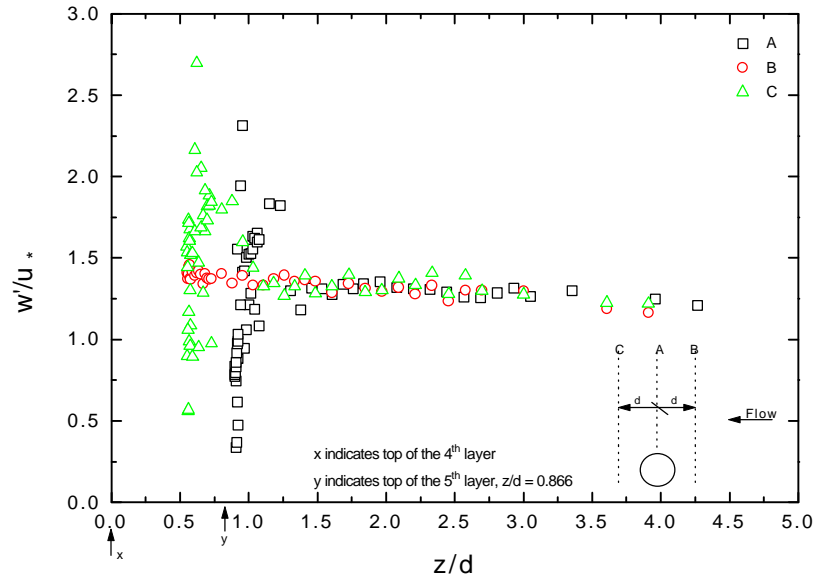


Figure VI-31. Variation of normal rms velocity for the 20% sediment bed packing density case.

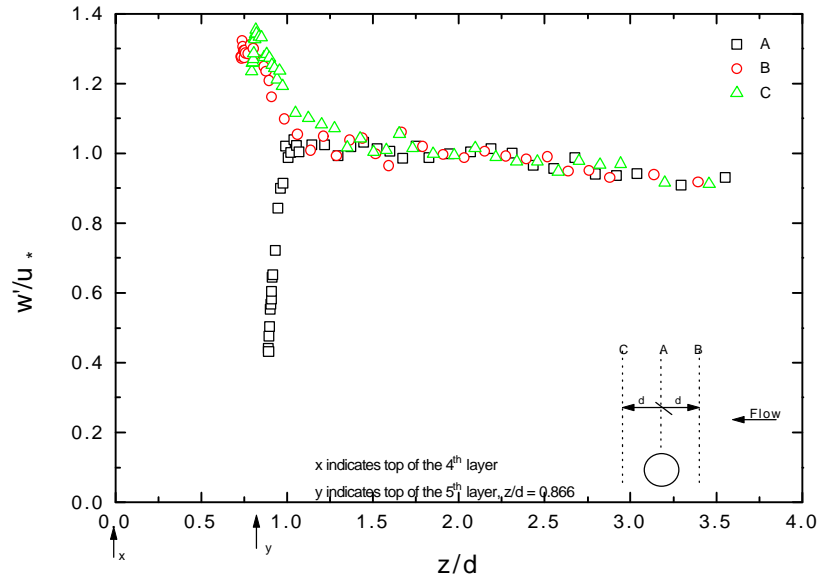


Figure VI-32. Variation of normal rms velocity for the 35% sediment bed packing density case.

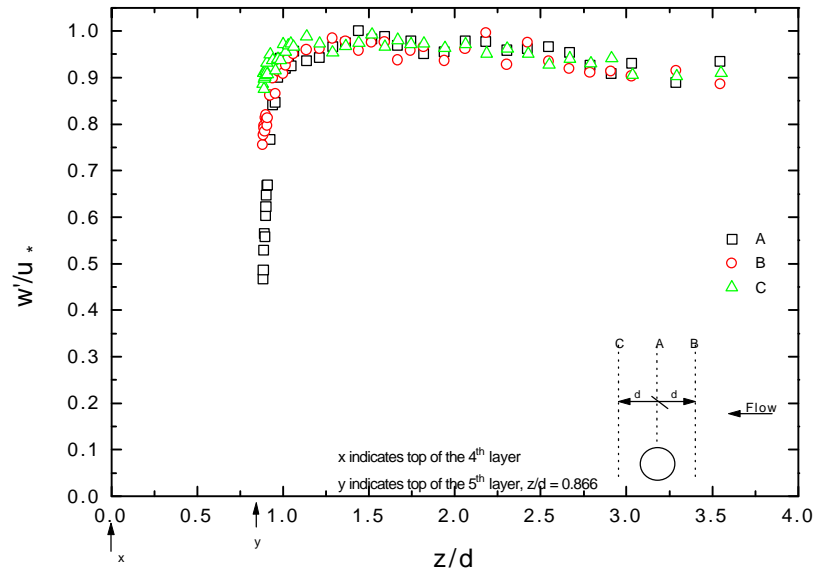


Figure VI-33. Variation of normal rms velocity for the 50% sediment bed packing density case.

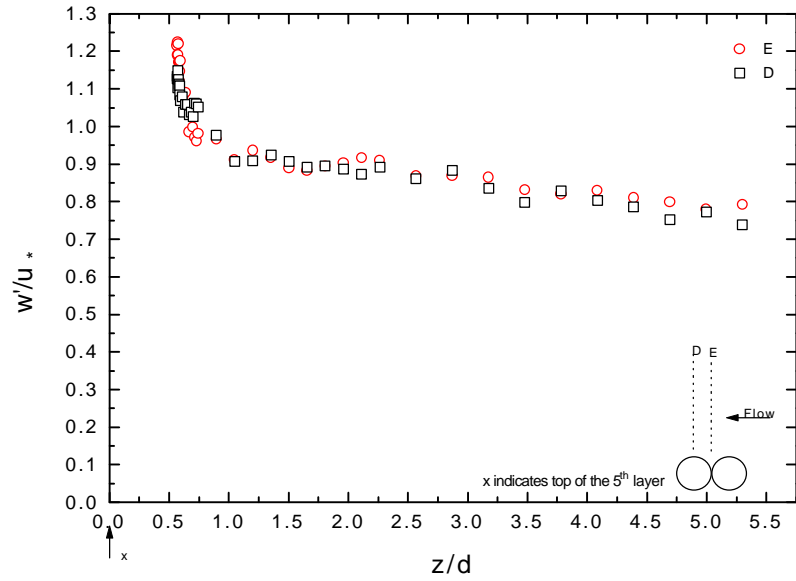


Figure VI-34. Variation of normal rms velocity for the 70% sediment bed packing density case.

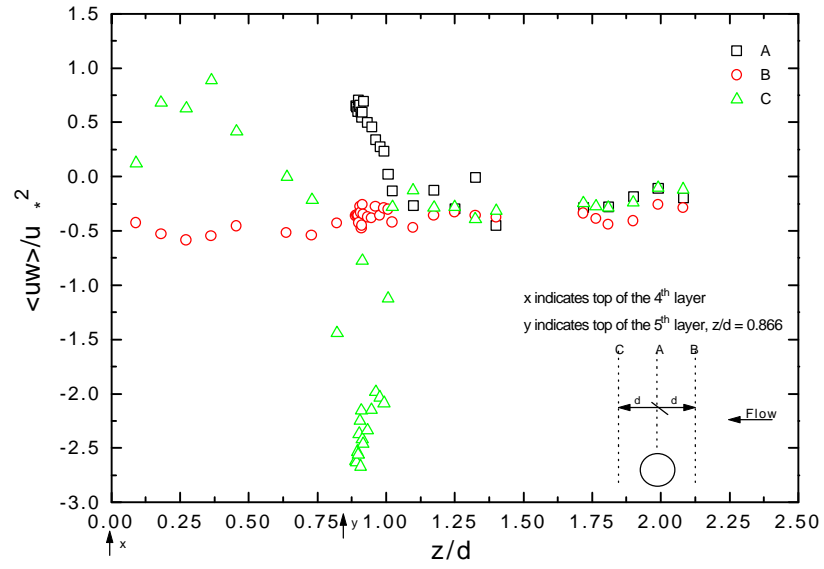


Figure VI-35. Variation of the Reynolds shear stress for the 2% sediment bed packing density case.

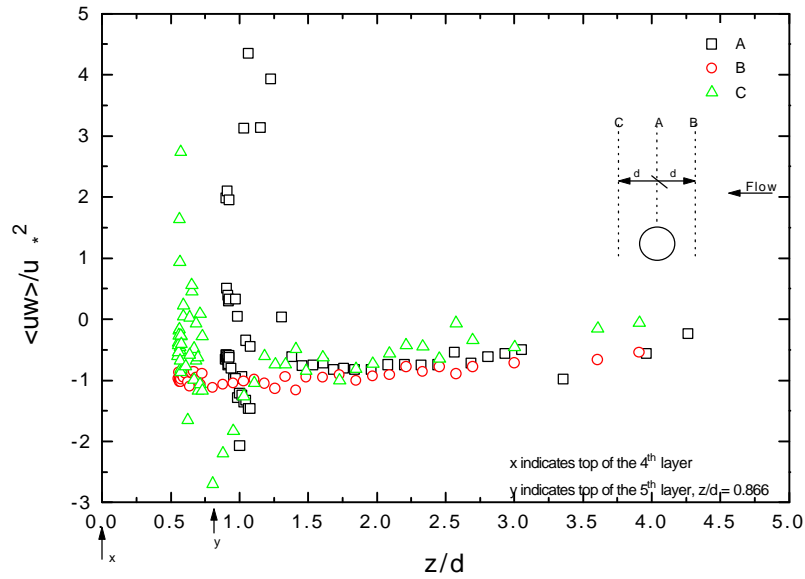


Figure VI-36. Variation of the Reynolds shear stress for the 20% sediment bed packing density case.

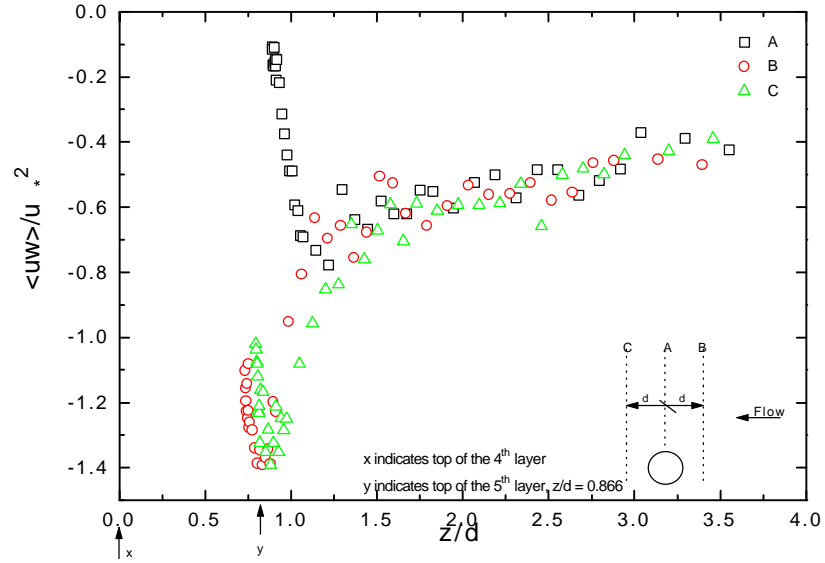


Figure VI-37. Variation of the Reynolds shear stress for the 35% sediment bed packing density case.

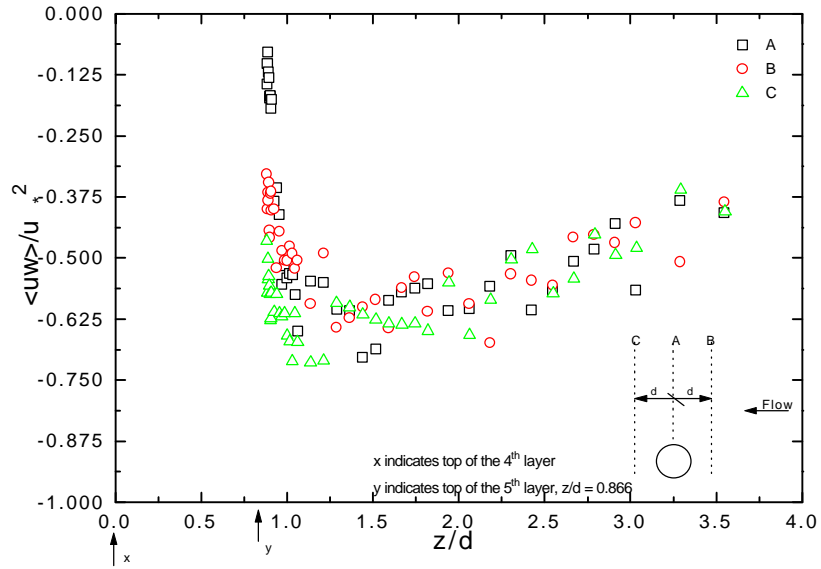


Figure VI-38. Variation of the Reynolds shear stress for the 50% sediment bed packing density case.

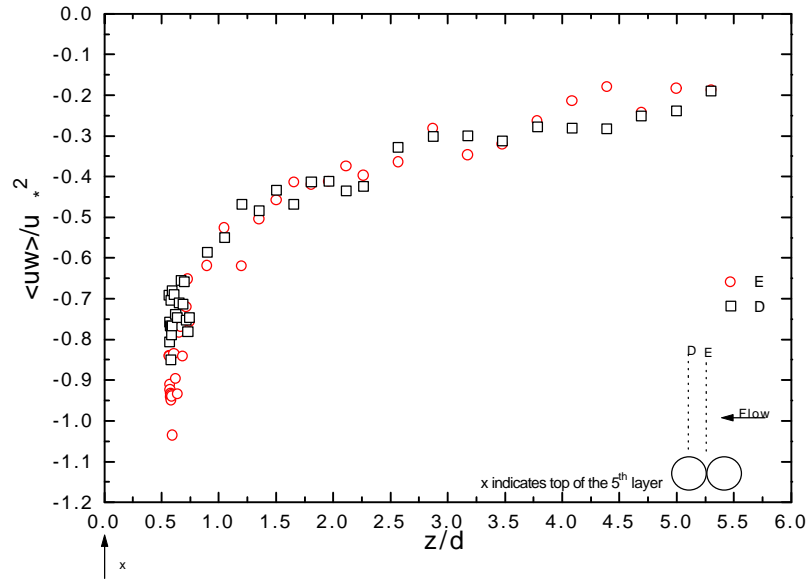


Figure VI-39. Variation of the Reynolds shear stress for the 70% sediment bed packing density case.

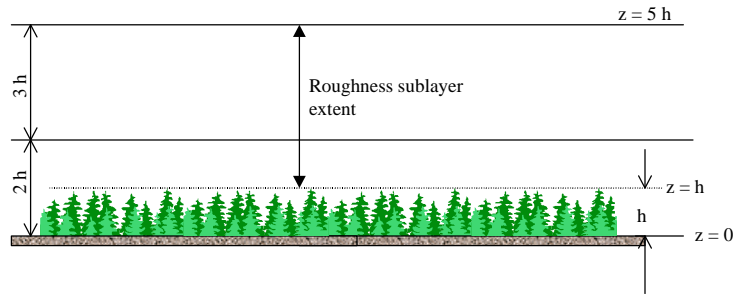


Figure VI-40. Schematic of the roughness sublayer.

Table VI.1. Relevant time scales for the single ball experiment.

No.	Description	Time, sec
1	Mean time between LDV data	0.227
2	Video framing speed	1/30
3	Mean time between successive ball movements	30
4	Time scale of large eddies, H/U_B	0.125
5	Mean time between bursts ⁽¹⁾ , $6H/U_B$	0.75
6	Lifetime of bursts ⁽²⁾ , $t_+ = tu_*^2/\nu$; here $u_* = 0.0313$ m/s, $\nu = 1.018 \times 10^{-6}$ m ² /s, $t_+ = 500$	0.52
7	Convection time from LDV measurement point to ball $0.318^{(3)} \times 10^{-3} / 0.128^{(4)}$	2480×10^{-6}
8	Convection time of an eddy 4.4 mm high and moving at the mean velocity speed. $4.4 \times 10^{-3}/0.128^{(4)}$	34.4×10^{-3}

¹ Nezu and Nakagawa, 1993

² Smith and Metzler, 1983

³ Refer to Figure VI.1

⁴ From LDV measurements

Table VI.2. Tabulation of SNR values at different Δt values.

Single Ball Data			
$\Delta t, \mu s$	ρ_{max}	ρ_{bkg}	$SNR = \frac{r_{max}}{r_{bkg}}$
40,000	90	22	4
100,000	134	55	2.4
250,000	225	138	1.6

Table VI.3. Flow statistics and error estimates of the global and local data.

Description	Global G	Local, $\tau = 0$ $\Delta t = 40,000 \mu s$ L	% change $(L - G) / G \times 100$	Error	Comments
$\langle U \rangle$, m/s	0.128	0.184	40	$\pm 0.0254^{(1)}$	Significant
$\langle W \rangle$, m/s	0.08	0.071	-11	$\pm 0.0147^{(1)}$	Not significant
u' , m/s	0.1	0.123	23	$\pm 0.0193^{(2)}$	Significant
w' , m/s	0.064	0.071	9.8	$\pm 0.01^{(2)}$	Not significant
$\langle uw \rangle$, m^2/s^2	0.0045	0.008	78	± 0.003	Marginal

Note: All errors tested at 95% level.

¹ Z-test applied, Gaussian distribution assumed.

² Chi-Square distribution applied.

Table VI.4. Extent of roughness sublayer based on different variables for each packing configuration.

Packing, %	Roughness sublayer extent in terms of z/d based on				
	$\langle U \rangle$	$\langle W \rangle$	u'	w'	$\langle uw \rangle$
2	1.2	1.4	1.3	1.4	1.75
20	1.4	1.75	I ⁽¹⁾	1.6	1.8
35	I ⁽¹⁾	1.5	1.25	1.5	2
50	I ⁽¹⁾	1.2	1.1	1	1.25
70 ⁽²⁾	Less than 0.4	Less than 0.4	Less than 0.4	Less than 0.4	Less than 0.4

¹ I = Indistinguishable

² Measured from the top of the 5th layer.

Chapter VII

Conclusions and Recommendations

Two investigations were carried out as part of this work. The first part, referred to as the single ball experiment, investigated the role of turbulence in initiating motion of a sediment particle (glass ball) placed in a turbulent, open channel flow with a rough, porous bottom wall. The porous bed comprised balls identical to the test glass ball. A video camera and a 3-D LDV system were used in tandem.

The second part, called the sediment bed packing density experiment, investigated the nature of fluid-solid interaction under different sediment bed packing density conditions of a rough, *immobile* bed (composed of lead balls of the same size as the glass balls used in the first part). The summary of results from both parts is presented below.

VII.1 Single Ball Experiment

The single ball experiment provided some very interesting and significant insights into the interaction between sediment motion and velocity events, which occur just prior to the motion.

Establishing correlation between the random, discontinuous LDV velocity signals, and the binary signal from sediment motion (either the sediment has moved or it has not)

was accomplished through the digital correlation techniques commonly applied in photon correlation (Mayo and Smart, 1980).

The correlation results obtained from the above technique demonstrate that the number of LDV velocity measurements per unit time (data rate) *increases four folds* just prior to the sediment motion. Consistent with a velocity bias effect (characteristic of any LDV system), the mean velocity, and the associated rms values of fluid events measured by the LDV system just before sediment motion are *expected* to be higher than their background levels. To examine this expectation the following analyses were carried out.

Analyses of fluid velocity events that precede sediment motion indicate that the *local* streamwise mean and rms velocities, indeed, are significantly higher than the corresponding background values. This suggests that a fluid parcel that has a higher-than-average velocity impinges on the sediment. However, neither the size nor the lifetime of such a fluid parcel could be determined from this study. Nevertheless, based on the experimental evidence, for the single exposed sediment particle, one can conclude that form drag is the most dominant of all forces, while the role of lift force is negligible. In support of this, the mean and rms velocities in the normal direction appear to be uncorrelated with sediment motion.

Reynolds shear stress and associated bursting activities have long been considered to be important in initiating sediment motion. The experimental evidence from this work does not suggest that the Reynolds shear stress is correlated with sediment motion, at least in the isolated regime. This does not preclude the fact that the momentum transfer events (sweeps or ejections) may have played a role in increasing the mean velocity, which ultimately led to sediment motion. In other words, it is hypothesized that a

sweeping event (that transfers momentum from the core part of the flow to the bed part) occurring upstream (upstream of the LDV measurement point) of the sediment location led to a local increase of momentum of a fluid parcel. In the vicinity of the sediment, this local increase of momentum manifested itself as an increase of the mean velocity of the fluid parcel. Impingement of such a fluid parcel on the sediment ultimately led to the sediment particle's motion.

To successfully model incipient sediment motion by including the stochastic nature of the fluid, it is important to include the fluid events that not only correlate well with sediment motion, but also provide physically plausible results. For a single exposed sediment, placed atop a porous bed composed of identical spheres, the preferred mode of motion is rolling (as rolling requires less force than sliding). Thus, the moment of *instantaneous* fluid forces acting on the sediment is relevant to sediment incipient motion and is considered below.

From the moment equation applied to the single, exposed sediment placed atop a bed of identical spheres, a new, normalized variable, ϕ , that describes the (instantaneous) moment of forces acting on the sediment, was formulated. The variable, ϕ , has significant physical meaning to the motion of the single sediment particle; it denotes the instantaneous moment (of forces) acting on the sediment. If ϕ is the relevant variable for sediment motion, then it should correlate stronger with sediment motion than any other variable, which was clearly observed to be true here. The correlation between sediment motion and ϕ (for $\phi > \phi_{\text{crit}}$, where ϕ_{crit} is the *theoretical* moment value required to initiate sediment motion) was significantly stronger than the correlation of sediment motion with any other flow variable.

As a first step to model incipient motion of sediment with instantaneous fluid velocity events, the probability density function of ϕ , $p(\phi)$, was considered. The measured distribution of $p(\phi)$ indicated that the fluid velocity events, where ϕ was greater than ϕ_{crit} , occurred much more frequently just prior to sediment motion than when there was no sediment motion. By applying the stochastic concept, developed as a part of this work, the value of ϕ was estimated to be $1.7 \phi_{crit}$. Thus, the variable ϕ , not only correlated well with sediment motion but also, provided the basis for physical plausibility through the moment balance equation.

Correlation of sediment motion with bursts (identified by using a detection scheme, such as the quadrant method) was not possible due to the nature of the Reynolds stress distribution with quadrants I and III events dominating.

VII-2 Sediment Bed Packing Density Experiment

The three regimes identified by Morris (1955) guided the selection of the sediment bed packing density values for this part of the work. Five sediment bed packing densities were considered, viz., 2%, 20%, 35%, 50% and the 70%. The 70% packing case indicates a completely packed sediment bed, where addition of more lead balls is not possible. The 2% case belongs to the isolated ball regime, the 20% and 35% belong to the wake-interference regime, and the 50% and the 70% belong to the skimming flow regime.

Detailed LDV velocity measurements were obtained around a specific lead ball at three streamwise locations for each of the five packing density cases. The profile

measurements obtained at the three locations were then compared to identify the effects on the flow characteristics at these packing densities.

The profiles described here show that in the 2% case the flow is locally more distorted in the vicinity of individual balls than in the other four packing cases. In other words, measurements around the lead ball in the 2% packing case clearly indicate acceleration of the fluid above the ball, and formation of a re-circulation region downstream of the ball. The downstream distance through which such disturbance (wake created by the ball) exists was not measured in this work. However, based on measurements made at location B (one diameter upstream of the ball), it is possible to surmise that such disturbances do not propagate for more than 6 ball diameters (mean distance between balls in the 2% case). Thus, the 2% case appears to behave like an isolated ball case, as the effect of any sediment does not reach its neighbors.

As packing density is increased influence of individual balls seem to loose importance in terms of affecting the flow characteristics. This behavior becomes stronger for the 35% and 50% cases when compared to the 20% case. In the 20%, and 35% cases, the LDV measurement volume could not be traversed close enough to the balls to measure local flow disturbances, if any. In the 70% case the differences introduced by individual balls appear to be completely obliterated.

From a sediment transport point of view, the different packing density cases provided some important insights. The instantaneous moment variable, ϕ , was again used to model sediment motion. Based on the experimental measurements in the 2% case form drag played a more significant role than the lift force. The magnitude of the lift force, however, clearly increased with increasing packing density. Though correlation

between velocity events and sediment motion were not made in the five packing cases, the increase in the magnitude of the lift force with packing density suggests that in the 70% case, sediment motion is initiated by the lift force. Since ϕ is the normalized net moment due to both the lift and the drag forces, it is physically meaningful to use $p(\phi)$ distribution to model sediment transport (see Papanicolaou, 1997, for details and results pertaining to sediment transport).

VII-3 Recommendations

Several possibilities exist to expand on the present work. The following are some of the suggestions, and for some these, significant background material is already available.

1. The next series of single ball tests should include flow visualization, in addition to LDV and video photography. Such an arrangement will help identify individual flow structures and their interaction with the mobile sediment (ball). Also, the vortex shedding downstream of the sediment, may produce a frequency, which interacts with downstream sediment, consequently inducing vibrations, and possibly motion of the sediment itself. Flow visualization with glass balls (the sediment particles used in the present experiments) may be difficult as high Reynolds number is required to dislodge the ball. Lighter materials, such as PVC or Viton may be used, so that the flow condition becomes less severe, which would permit better flow visualization.
2. Similar to the fully exposed ball, a ball can be placed in 70% packing, with the LDV measurement volume positioned right above the entrainable ball. To ensure that only the ball that is underneath the LDV measurement volume moves, its neighboring balls

may be lead spheres of identical size. Again, a ball lighter than glass (but heavier than water) will be better. This experiment would reveal the role of fluid lift forces in initiating ball motion.

3. The LDV data rate in the present experiments was too low. A higher LDV data rate, high enough to be time-resolved, may be useful in extracting the flow frequency information through fast Fourier transform.
4. Effect of bed geometry in the single ball case could be investigated. The less probable scenario shown in Figure V-1 may serve to support some of the findings of this study.

References

- Alfredsson, P. H., and A. V. Johansson (1984). "On the Detection of Turbulence-Generating Events." Journal of Fluid Mechanics, Vol. 139, pp. 325-345.
- Antonia, R. A. (1981). "Conditional Sampling in Turbulence Measurement." Annual Review of Fluid mechanics, Vol. 13, pp. 131-156.
- Antonia, R. A., and R. E. Luxton (1971). "The Response of a Turbulent Boundary Layer to a Step Change in Surface Roughness, Part 1. Smooth to Rough." Journal of Fluid Mechanics, vol. 48, part 4, pp. 721-761.
- Antonia, R. A., and R. E. Luxton (1972). "The Response of a Turbulent Boundary Layer to a Step Change in Surface Roughness, Part 2. Rough-to-Smooth." Journal of Fluid Mechanics, vol. 53, part 4, pp. 737-757.
- Balakrishnan, M., and C. L. Dancy (1994). "An Investigation of Turbulence in Open-Channel Flow via Three-Component Laser Doppler Anemometry." ASCE Conference, August 1-6, Buffalo, NY.
- Bandyopadhyay, P.R., and Watson, R.D. (1988). Structure of Rough-Wall Turbulent Boundary Layers. Physics of Fluids, vol. 31 (7), July, pp. 1877-1883.
- Bandyopadhyay, P. R. (1982). "Period between bursting in turbulent boundary layers." Physics of Fluids, Vol. 25, No. 10, pp. 1751-1754.
- Benedict, L. H., and R. D. Gould (1996). "Towards better uncertainty estimates for turbulence statistics." Experiments in Fluids, Vol. 22, pp. 129-136.
- Bettess, R. (1984). "Initiation of Sediment Transport in Gravel Streams." Proceedings of the Institution of the Civil Engineers, Part 2, March, pp. 79-88.
- Billi, P. (1988). "A Note on Cluster Bedform Behavior in a Gravel-Bed River." Catena, Vol. 15, pp. 473-481.
- Blackwelder, R. F., and J. H. Haritonidis (1983). "Scaling of the Bursting Frequency in Turbulent Boundary Layers." Journal of Fluid Mechanics, Vol. 132, pp. 87-103.

- Blackwelder, R. F., and R. E. Kaplan (1976). "On the Wall Structure of the Turbulent Boundary Layer." Journal of Fluid Mechanics, Vol. 76, pp. 89-112.
- Brayshaw, A. C., L. E. Frostick, and I. Reid (1983). "The Hydrodynamics of Particle Clusters and Sediment Entrainment in Coarse Alluvial Channels." Sedimentology, Vol. 30, pp. 137-143.
- Bridge, J. S., and Bennett, S. J. (1992). "A Model for the Entrainment and Transport of Sediment Grains of Mixed Sizes, Shapes, and Densities." Water Resources Research, Vol. 28, No. 2, pp. 337-363.
- Cantwell, B. J. (1981). "Organized Motion in Turbulent Flow." Annual Review of Fluid Mechanics, Vol. 13, pp. 457-515.
- Chen, Charng, Ning (1970). "Removal of a spherical particle from a flat bed." Doctoral Dissertation, School of Civil Engineering, Georgia Institute of Technology, Atlanta, Georgia.
- Chepil, W. S. (1959). "Equilibrium of solid grains at the threshold of movement by wind." Proc. Soil Sci. Soc. Am., Vol. 23, pp. 422-428.
- Christiansen, B. A. (1977). On the stochastic nature of scour initiation. International Association for Hydraulic Research, pp. 65-72.
- Clifford, N. J., J. McClatchey, and J. R. French (1991). "Measurements of Turbulence in the Benthic Boundary Layer Over a Gravel Bed and Comparison Between Acoustic Measurements and Predictions of the Bedload Transport of Marine Gravels." Sedimentology, Vol. 38, pp. 161-171.
- Cline, C., and S. Deutsch (1993). "On Elevated RMS Level in Wall-Bounded Turbulent Flows When Measured by Laser Doppler Velocimeter." Experiments in Fluids, Vol. 15, pp. 130-132.
- Coleman, N. L. (1967). "A Theoretical and Experimental Study of Drag and Lift Forces Acting on a Sphere Resting on Hypothetical Stream Bed." Paper Presented at the 12th Congress, International Association for Hydraulics Research, Fort Collins, Colorado.
- Corino, E.R., and Brodkey, S.R. (1969). A Visual Investigation of the Wall Region in Turbulent Flow. Journal of Fluid Mechanics, vol. 37, part I, pp. 1-30.
- Corrisin, S. (1973). "Comment on Statistical Characteristics of Reynolds Stress in a Turbulent Boundary Layer." Physics of Fluids, Vol. 16, p 341.
- Diplas, P., and G. Parker (1992). "Deposition and Removal of Fines in Gravel-Bed Streams," Dynamics of Gravel-Bed Rivers. Edited by P. Billi, R. D. Hey, C. R. Thorne, and P. Tacconi.

- Drain, L. E. (1980). The Laser Doppler Technique. John Wiley & Sons, Chichester.
- Drake, T. G., R. L. Shreve, W. E. Dietrich, P. J. Whiting, and L. B. Leopold (1988). "Bedload Transport of Fine Gravel Observed by Motion-Picture Photography." Journal of Fluid Mechanics, Vol. 192, pp. 193-217.
- Durst, F., A. Melling, and J. H. Whitelaw (1981). Principles and practice of laser-Doppler anemometry." II Edition, Academic Press.
- Edwards, R. V. (1987). Report of the Special Panel on Statistical Particle Bias Problems in Laser Anemometry." Journal of Fluids Engineering, Vol. 109, pp. 89-93.
- Egiazaroff, I. V. (1965). "Calculation of Non-Uniform Sediment Concentration." Journal of Hydraulic Division, ASCE, Vol. 91, pp. 225-247.
- Einstein, H. A., and E. A. El-Samni (1949). "Hydrodynamic Forces on a Rough Wall." Review of Modern Physics, Vol. 21, pp. 520-524.
- Fenton, J. D., and J. E. Abbott (1977). "Initial Movement of Grains on a Stream Bed: The Effect of Relative Protrusion." Proceedings of the Royal Society of London, Series A, Vol. 352, pp. 523-537.
- Fontaine, A. A., and S. Deutsch (1996). "Three-component, time-resolved velocity statistics in the wall region of a turbulent pipe flow." Experiments in Fluids, Vol. 18, pp. 168-173.
- Fontaine, A. A., and S. Deutsch (1996). "Structure of near wall turbulence downstream of a wall mounted protrusion: an interesting Reynolds stress suppression phenomena." Experiments in Fluids, Vol. 20, pp. 365-376.
- Gessler, J. (1965). "The Beginning of Bedload Movement of Mixtures Investigated as Natural Armoring Channels." Ph.D. Thesis at the Swiss Federal Institute of Technology.
- Grass, A. J. (1971). "Structural Features of Turbulent Flow Over Smooth and Rough Boundaries." Journal of Fluid Mechanics, Vol. 50, Part 2, pp. 233-255.
- Grass, A. J. (1983). The Influence of Boundary Layer Turbulence on the Mechanics of Sediment Transport. Edited by B. M. Sumer, and A. Muller, pp. 3-17, A. A. Balkema, Rotterdam, Netherlands.
- Grass, A. J., R. J. Stuart, and M. Mansour-Tehrani (1991). "Vortical Structures and Coherent Motion in Turbulent Flow Over Smooth and Rough Boundaries." Journal of Fluid Mechanics, Vol. 336, pp. 35-65.
- Grass, A.J., Stuart, R.J., and Mansour-Tehrani, M. (1993). Common Vortical Structure of Turbulent Flows over Smooth and Rough Boundaries. American Institute of Aeronautics and Astronautics Journal, Vol. 31, No. 5, pp. 837-847.

Gupta, A. K., and R. E. Kaplan (1972). "Statistical Characteristics of Reynolds Stress in a Turbulent Boundary Layer." Physics of Fluids, Vol. 15, No. 6, June, pp. 981-985.

Gyr, A. (1983). "Towards a Better Definition of the Three Types of Sediment Transport, Journal of Hydraulic Research, Vol. 21, pp. 1-15.

He, M., and Q. Han (1982). "Stochastic Model of Incipient Sediment Motion." Journal of Hydraulic Division, ASCE, Vol. 108, No. HY2, February, pp. 211-224.

Hussain, A. K. M. F. (1983). "Coherent Structures -- Reality and Myth." Physics of Fluids, vol. 26(10), October, pp. 2816-2850.

Ikedo, S. (1982). "Incipient motion of sand particles on side slopes." Journal of the Hydraulic Division, ASCE, Vol. 108, pp. 95-114.

Jackson, P. S. (1981). "On the displacement height in the logarithmic velocity profile." Journal of Fluid Mechanics, Vol. 111, pp. 15-25.

Kalinske, A. A. (1947). "Movement of Sediment as Bed Load in Rivers." Transactions, American Geophysical Union, Vol. 28, No. 4, pp. 615-620.

Kline, S. J., W. C. Reynolds, F. A. Schraub, and P. W. Runstadler (1967). "The Structure of Turbulent Boundary Layers." Journal of Fluid Mechanics, Vol. 30, pp. 741-773.

Komar, P. D., and Z. Li (1986). "Pivoting Analyses of the Selective Entrainment of Sediments by Shape and Size with Application to Gravel Threshold." Sedimentology, Vol. 33, pp. 425-436.

Komori, S., Ueda, H., Ogino, F., and Mizushima, T. (1982). Turbulence Structure and Transport Mechanisms at the Free-Surface in an Open Channel Flow. International Journal of Heat & Mass Transfer, Vol. 25, No. 4, pp. 513-521.

Krogstad, P. A., R. A. Antonia, and L. W. B. Browne (1992). "Comparison Between Rough and Smooth Wall Turbulent Boundary Layers." Journal of Fluid Mechanics, Vol. 245, pp. 599-617.

Kuhnle, R. A. (1995). "Incipient Motion of Sand-Gravel Sediment Mixtures." Journal of Hydraulic Engineering, Vol. 119, No. 12, pp. 448-449.

Lane, E. W., and A. A. Kalinske (1939). "The relation of suspended to bed material in rivers." EOS Transactions, AGU, Vol. 20, 637-641.

Lapin, L. L. (1990). Probability and statistics for modern engineering. II Edition, PWS-KENT Publishing Company, Boston, Massachusetts.

Laser Velocimetry Systems (1986), TSI Incorporated, St. Paul, Minnesota.

Lavelle, J. W., and H. O. Mofjeld (1987). "Do Critical Stresses for Incipient Motion and Erosion Really Exist?" Journal of Hydraulic Engineering, Vol. 113, No 3, March, pp. 370-385.

Lee, B. E., and B. F. Soliman (1977). "An Investigation of the Forces on Three Dimensional Bluff Bodies in Rough Wall Turbulent Boundary Layers." Fluids Engineering, Transactions of the ASME, September, pp. 503-510.

Lindsay, C. A., and Brian Owsenek (1993). "The design of a three-component LDA system for application for an open channel flow." ASME Summer Meeting of the FED, Vol. 153, pp. 11-14.

Ling, C.H. (1995). "Criteria for the Incipient Motion of Spherical Sediment Particles". Journal of Hydraulic Engineering, ASCE, Vol.. 121(6), pp.. 472-478.

Lu, S. S., and W. W. Willmarth (1973). "Measurement of the Structure of the Reynolds Stress in a Turbulent Boundary Layer." Journal of Fluid Mechanics, Vol. 60, Part III, pp. 481-511.

Luchic, T. S., and W. G. Tiederman (1987). "Timescale and Structure of Ejections and Bursts in Turbulent Flows." Journal of Fluid Mechanics, Vol. 174, pp. 529-552.

Mantz, P. A. (1980). "Low Sediment Transport Rates Over Flat Beds." Journal of the Hydraulic Division, ASCE, Vol. 106, No. HY7, July, pp. 1173-1190.

Marshall, K. (1971). "Drag Measurements in Roughness Arrays of Varying Density and Distribution." Agricultural Meteorology, vol. 8, pp. 269-292.

Mayo, W. T. (1978). "Spectrum measurements with laser velocimeters." Proceedings of the Dynamic Flow Conference, DK-2740, Skovlunde, Denmark.

Mayo, W. T., and A. E. Smart (1980). "Tutorial: Digital correlation data processing." Proceedings from the 4th International Conference, Joint Institute for Aeronautics and Acoustics, Stanford University, Stanford, California, August 24-27.

McLaughlin, D. K., and W. G. Tiederman, Jr. (1973). "Biasing correction for Individual Realization of Laser Anemometer Measurements in Turbulent Flow." Physics of Fluids, Vol. 16, No. 12, pp. 2082-2088.

Menon, Rajan, and Wing T. Lai (1991). "Key considerations in the selection of seed particles for LDV measurements." Laser Anemometry, Advances and Applications, Vol. 2, Editors: Alexander Dybbs, and Bahman Ghorashi, ASME.

Meyers, J. F. (1985). "The Elusive Third Component." International Symposium on Laser Anemometry, ASME Winter Annual Meeting, Miami Beach, Florida.

- Moffat, Robert J. (1988). "Describing the uncertainties in experimental results." Experimental Thermal and Fluid Science, Vol. 1, pp. 3-17.
- Moore, M. C. (1994). "Bedload Transport: The Effects of Particle Shape and an Investigation of a Wide Range of Transport Rates." M. S. Thesis, Virginia Polytechnic Institute and State University, Blacksburg, Virginia.
- Morris, H. M. (1955). "Flow in rough conduits." Transactions of the ASCE, Vol. 120, pp. 373-398.
- Naden, P. (1987). "An Erosion Criterion for Gravel-Bed Rivers." Earth Surface Processes Landforms, Vol. 12, pp. 83-93.
- Nakagawa, H., and I. Nezu (1977). "Prediction of the Contributions to the Reynolds Stress from Bursting Events in open-Channel Flows." Journal of Fluid Mechanics, vol. 80, pp. 99-128.
- Nakagawa, H., and I. Nezu (1978). "Bursting Phenomenon Near the Wall in Open-Channel Flows and its Simple Mathematical Model." Memoirs, Faculty of Engineering, Kyoto University, Vol. 40, pp. 213-240, Japan.
- Nakagawa, H., and I. Nezu (1981). "Structure of Space-Time Correlation's of Bursting Phenomenon in an Open Channel Flow." Journal of Fluid Mechanics, Vol. 104, pp. 1-43.
- Neill, C. R., and M. S. Yalin (1969). "Qualitative Definition of Beginning of Bed Movement." Journal of the Hydraulics Division, ASCE, Vol. 95, HY1, January, pp. 585-587.
- Nelson, J., R. L. Shreve, S. R. McLean, and T. G. Drake (1995). "Role of Near-Bed Turbulence Structure in Bed Load Transport and Bed Form Mechanics." Water Resources Research, Vol. 31, No 8, pp. 2071-2086.
- Nezu, I., and Rodi, W. (1986). Open-Channel Flow Measurements with a Laser Doppler Anemometer. Journal of Hydraulic Engineering, vol. 112, No. 5, May, pp. 335-355.
- Nezu, I., and H. Nakagawa (1993). Turbulence in Open Channel Flow. Published by A. A. Balkema, Rotterdam.
- Nikuradse, J. (1933). "Stromungsgesetze in rauhen Rohren." Forschg. Arb. Ing. - Wes. No. 361.
- Offen, G. R., and S. J. Kline (1974). "Combined Dye-Streak and Hydrogen Bubble Visual Observation of a Turbulent Boundary Layer." Journal of Fluid Mechanics, Vol. 62, pp. 223-239.
- O'Loughlin, E. M. (1965). Doctoral Dissertation, Department of Civil Engineering, University of Iowa, Ames, Iowa.

- Paintal A. S. (1971). "Concept of Critical Shear Stress in Loose Boundary Open Channels." Journal of the Hydraulics Division, ASCE, Vol. 9, pp. 91-114.
- Paintal, A. S. (1971). "A Stochastic Model of Bed Load Transport." Journal of Hydraulic Research, Vol. 9, No. 4, pp. 527-554.
- Paola, Chris (1996). "Incoherent Structure: Turbulence as a Metaphor for Stream Braiding." Coherent Flow Structures in Open Channels, Edited by P. J. Ashworth, S. J. Bennett, J. L. Best, and S. J. McLelland, Published by John Wiley & Sons, Ltd.
- Papanicolaou, A. (1997). "The role of turbulence on the initiation of sediment motion." Doctoral Dissertation, Virginia Polytechnic Institute and State University, Blacksburg, Virginia.
- Papanicolaou, A., M. Balakrishnan, P. Diplas, and C. L. Dancey (1995). "Effects of Particle Packing on Bedload Motion." Proceedings of the First International Conference on Water Resources, San Antonio, Texas, August 14-18, pp. 712-716.
- Papanicolaou, A., P. Diplas, M. Balakrishnan, , and C. L. Dancey (1996). "A note on incipient motion of river sediment particles." Proceedings of the 11th ASCE Engineering Mechanics Conference, Florida, May 19-22, pp. 657-660.
- Rajagopalan, S., and Antonia, R.A. (1982). Use of a Quadrant Analysis Technique to Identify Coherent Structures in a Turbulent Boundary Layer. Physics of Fluids, vol. 25 (6), June, pp. 949-956.
- Raupach, M. R., A. S. Thom, and I. Edwards (1980). "A Wind-Tunnel Study of Turbulent Flow Close to Regularly Arrayed Rough Surfaces." Boundary-Layer Meteorology, Vol. 18, pp. 373-397.
- Raupach, M.R., Antonia, R.A., and Rajagopalan, S. (1991). Rough-Wall Turbulent Boundary Layers. Applied Mechanics Review, Vol. 44, January, pp. 1-25.
- Reid, I., and L. E. Frostick (1987). "Toward a Better Understanding of Bedload Transport." Recent Developments in Fluvial Sedimentology, Society of Economic Paleontologists and Mineralogists, Special Publication No. 39, pp. 13-19.
- Reynolds, A. J. (1974). Turbulent Flows in Engineering. Wiley & Sons, London, Great Britain.
- Roberson, J. A., and Clayton T. Crowe (1985). Engineering Fluid Mechanics. Houghton Mifflin Company, Boston, Massachusetts.
- Schlichting, H. (1979). Boundary Layer Theory. McGraw Hill Book Company.

Sekine, M., and H. Kikkawa (1988). "A Fundamental Study on the Sediment Transport in an Open Channel Flow." *Memoirs of the School of Science and Engineering, Waseda University*, No. 52, pp. 103-141.

Shields, A. (1936). "Anwendung der Ähnlichkeitsmechanik und der Turbulenzforschung auf die Geschiebebewegung." *Mitteilungen der Preussischen Versuchsanstalt für Wasserbau und Schiffbau*, No. 26, Berlin, Germany (English Translation by W. P. Ott and J. C. Uchelon, California Institute of Technology, Pasadena, California, USA).

Smith, C.R., and Metzler, S.P. (1983). The Characteristics of Low-Speed Streaks in the Near-Wall Region of a Turbulent Boundary Layer. *Journal of Fluid Mechanics*, vol. 129, pp. 27-54.

Steffler, P. M., N. Rajaratnam, and A.W. Peterson (1985). "LDA Measurements in Open Channel." *Journal of Hydraulic Engineering*, ASCE, Vol. 111, pp. 119-130.

Sumer, B. M., and R. Deigaard (1981). "Particle Motions Near the Bottom in Turbulent Flow in an Open Channel." *Journal of Fluid Mechanics*, Vol. 109, pp. 311-338.

Tennekes, H., and J. L. Lumley (1992). *A first course in turbulence*. 14th printing, MIT Press Design Department, Boston, Massachusetts.

Vanoni, V. A. (1964). "Measurements of Critical Shear Stress for Entraining Fine Sediments in a Boundary Layer." Report KH-R-7, W. M. Keck Laboratory of Hydraulic and Water Resources, California Institute of Technology.

Vanoni, V. A. (1975). "River Dynamics." *Advances in Applied Mechanics*, Vol. 15, pp. 1-87.

Vanoni, V. A., P. C. Benedict, D. C. Bondurant, J. E. McKee, R. F. Piest, and J. Smallshaw (1966). "Sediment Transportation Mechanics: Initiation of Motion, Progress Report, Task Committee on Preparation of the Sedimentation Manual." *Journal of the Hydraulics Division*, ASCE, Vol. 92, No. Hy2, March, pp. 291-314.

Wallace, J. M. (1985). "The vortical structure of bounded turbulent shear flow." *Flow of Real Fluids* (ed. Meier, G. E. A., and F. Obermeier), Lecture Notes in Physics, Springer-Verlag, No. 235, pp. 253-268.

Wark, C. E., and H. M. Nagib (1991). "Experimental Investigation of Coherent Structures in Turbulent Boundary Layers." *Journal of Fluid Mechanics*, Vol. 230, pp. 183-208.

Weiberg, P. L., and J. D. Smith (1985). "A theoretical model for saltating grain in water." *Journal of Geophysical Research*, Vol. 90, pp. 7341-7354.

- Weiberg, P. L., and J. D. Smith (1987). "Calculations of Critical Shear Stress for Motion of Uniform and Heterogeneous Sediments." Water Resources Research, Vol. 23, pp. 1471-1480.
- Wei, T., and W. W. Willmarth (1991). "Examination of V-Velocity Fluctuations in a Turbulent Channel Flow in the Context of Sediment Transport." Journal of Fluid Mechanics, Vol. 223, pp. 241-252.
- White, C. M. (1940). The Equilibrium of Grains on the Bed of a Stream." Proceedings of the Royal Society of London, Series A, 174, pp. 322-338.
- White, W. R., and T. J. Day (1982). "Transport of graded gravel bed material." Gravel-Bed Rivers, eds. R. D. Hey, J. C. Bathurst, and C. R. Thorne, Wiley, Chichester, pp. 181-223.
- White, F. M. (1986). Fluid Mechanics. II Edition, McGraw-Hill Publishing Company, New York.
- Wilcock, P. R. (1988). "Methods for Estimating the Critical Shear Stress of Individual Fractions in Mixed-Size Sediment." Water Resources Research, Vol. 24, pp. 1127-1135.
- Williams, J. J., P. D. Thorne, and A. D. Heathershaw (1989). "Measurements of Turbulence in the Benthic Boundary Layer over a Gravel Bed." Sedimentology, Vol. 36, pp. 959-971.
- Willmarth, W.W., and Lu, S.S. (1972). Structure of the Reynolds Stress Near the Wall. Journal of Fluid Mechanics, Vol. 55, part I, pp. 65-92.
- Wooding, R. A., E. F. Bradley, and J. K. Marshall (1973). "Drag Due to Regular Arrays of Roughness Elements of Varying Geometry." Boundary-Layer Meteorology, Vol. 5, pp. 285-308.
- Wylie C. R., and L. C. Barrett (1982). Advanced Engineering Mathematics. V Edition, McGraw-Hill Book company, New Delhi, India.
- Yalin, M. S. (1977). Mechanics of Sediment Transport. II Edition, Pergamon Press, New York, NY.

Appendix A1

LDV Background

A1.1 Basic Description of LDV Operation

The laser Doppler velocimeter, first used by Yeh and Cummins in 1964, has since been accepted as one of the standard fluid flow measuring tools. A number of books treat LDV systems in detail (for example, Drain, 1980; Durst et al, 1981) and only a brief discussion, relevant to the laser system used in this work, is provided here.

A laser (acronym for “Light Amplification by Stimulated Emission of Radiation”) beam is an intense, electromagnetic radiation, that is emitted by certain substances when they are sufficiently excited by an electric field or sometimes, an intense pulsating light source. For example, the substance used in the laser that was used in the present work is argon gas, excited by a high-voltage electric field.

Now consider a monochromatic laser beam split into two parts, and that the two resulting beams intersect in a region in space. These two beams originated from the same source and are monochromatic as well. When two monochromatic beams of light whose frequency, and phase relation are well defined and consistent, intersect, alternate bands of high (light) and low (dark) intensity bands, called interference fringes, are formed. The distance between a dark and light zone, the fringe spacing, f_s , is a function of only the wavelength of the light, λ , and the angle between the two beams, θ (in the medium where the light beams cross).

The fringe spacing is calculated using the commonly accepted fringe model as,

$$f_s = \frac{\lambda}{2 \sin\left(\frac{\theta}{2}\right)} \quad [\text{A1}\cdot\text{1}]$$

Since λ in a specified medium is constant, f_s is also fixed.

When a particle traverses the region containing interference fringes, it crosses the alternating bright and dark bands, scattering light in all directions. The frequency of the scattered light is proportional to the component of particle's velocity perpendicular to the interference fringes and therefore, the frequency is the relevant information in the signal for LDV. Since the fringe spacing can be determined from Equation A1.1, the velocity of the particle can be calculated by timing its travel across a predetermined number of interference fringes (hence, the velocity is an average across the measurement volume). The flow must be appropriately seeded to scatter 'sufficient' laser light so that a powerful signal is obtained. It should be reemphasized that the laser system measures the velocity of the seed material and not the flow molecules themselves.

Properly chosen seed is typically small enough so that it follows the flow sufficiently closely, but is big enough so that the quantity of scattered light is adequate for a good signal. Menon and Lai (1991), for example, discuss appropriate laser seeding requirements for various types of flows. Seed requirement for the present work is discussed in Chapter IV.

A1.2 The Laser Measurement Volume

The intersection region of the laser beams is ellipsoidal in shape. The particle crossings that occur in this ellipsoidal region are the relevant measurement events. The three-component LDV system used in the present work has six beams, and the ellipsoidal region is defined by the intersection region of the six beams. For convenience, the surface of the ellipse is defined to have a constant light intensity value that is equal to $1/e^2$ of the beam's centerline value (there are three ellipses, all of which coincide). The size of the ellipsoidal volume in the present work is estimated to be approximately 80 microns by 300 microns (which varies slightly with laser wavelength).

Since fruitful flow measurements could occur anywhere in the ellipsoid, strictly speaking, laser measurements are not 'point' measurements, but rather an average for the ellipsoidal region. In flow situations where steep velocity gradients are encountered, the averaging process across the ellipsoidal region increases measurement error.

A1.3 The Doppler Signal

As different seed particles travel across the ellipsoidal volume, light with frequency equal to the Doppler shift, but with randomly varying amplitude intensity, is scattered. The randomness arises from the disordered seeding particle distribution with the measurement volume. Each particle that traverses the laser measurement volume, produces a beat frequency (the Doppler frequency) that lasts for a duration equal to its transit time through the measurement volume.

Depending on the state of excitation, the cross section of the laser beam may take different shapes. Each shape is commonly referred to as the mode of the laser beam. Of

all the modes TEM₀₀ mode is the most suitable and required mode for LDV measurements and its amplitude envelope is Gaussian. For optimum performance of the laser system optical components, TEM₀₀ mode is vital. A typical voltage signal output for a particle going through the measurement volume consists of a sinusoidal voltage component superimposed on a mean value, called the ‘pedestal’. A signal processor is typically employed to subtract the pedestal value from the total signal, and remaining sinusoidal component is used to determine the Doppler frequency, f_D , as

$$f_D = \frac{V_n}{f_s} = \frac{V_n \left(2 \sin \frac{\theta}{2} \right)}{\lambda} \quad [\text{A1.2}]$$

where, V_n is the component of the particle’s velocity that is normal to the fringes. For a laser system with specified geometrical configuration, θ can be measured; for a specified medium, λ is known; then V_n is directly proportional to f_D . The uncertainty in the V_n measurement depends on θ and λ . Consider the variation of λ with temperature in an incompressible medium such as water. For example, in water, λ reduces by about 9 parts per million per °C (calculated from μ values for a range of 0 to 70°C, Handbook of Biochemistry and Molecular Biology). This means that for all practical purposes the need to calibrate laser velocimeter systems to account for temperature changes of the medium is obviated. However, the measurement uncertainty in θ introduces uncertainty in the V_n measurement. Experimentally estimated measurement uncertainty of θ , and its effect on flow statistics will be discussed later in a separate appendix.

A1.4 Flow Direction Sensing Through Frequency Shifting

The Doppler shift due to the particle crossing the fringes is proportional only to the magnitude of the velocity, and does not contain any information about the direction. The information about the particle's direction can be obtained if the symmetry of the output signal was removed. In other words, if the fringes can be moved relative to the fluid then the signal would be non-zero and equal to the shift frequency even when the flow is stagnant. In practice, the fringe movement is accomplished by shifting the frequency of one of the laser beams by using an acousto-optical device, called a frequency shifter. Acoustic waves of suitable wavelengths in a transparent medium, produce an effect that is very similar to a moving diffraction grating (another frequency shifting device). The acoustic waves generate alternating layers of high and low pressure regions, each with slightly different refractive index, effectively forming a three-dimensional diffraction grating (Drain, 1980). The wavelength of the input acoustic wave determines the wavelength of output laser beam. This effect was first observed by W. L. Bragg, hence, the acousto-optical frequency shifters are often called Bragg cells.

From the fringe model point of view, the frequency-shifted fringes move at a velocity that is proportional to the shift frequency. The scattered light that reaches the photodetector has both the shift and the Doppler frequency in it. Next, the signal from the photodetector reaches the downmixer. The downmixer output is such it is an algebraic sum of the shift and the Doppler frequencies. If the shift direction coincides with the flow direction, the output frequency will be lower, while for an opposite shift direction, it will be higher. The frequency shifter also removes the pedestal (if an internal filter is provided

for this purpose), compresses the frequency of large turbulence signals, optimizes the frequency range, and minimizes fringe bias error (Laser Velocimetry Systems, 1986).

In the present work, three frequency shifters (TSI, model 9186A), one for each of the three colors, were employed. The frequency shift is 40 MHz, with further frequency downmixing so that the signal processor can resolve small frequency changes relative 40 MHz.

A1.5 Signal Processing With Frequency Counters

As far as velocity measurement is concerned, the frequency of the output signal is the relevant information in the signal. The frequency varies with the seed velocity. Several different techniques, such as photon correlation, frequency tracking, spectrum analysis, and frequency counters, are used for measuring the signal. Frequency counters (TSI, Model 1992) were employed in this work for this purpose.

Frequency counters operate effectively even at the low data rates (typically 30 data per second or less) encountered in the present work, as long as the signal-to-noise ratio is acceptable. Basically, the frequency counter is an extremely accurate electronic clock that measures the time, τ_i , for n_i cycles of the output Doppler signal, with n_i typically being equal to 8 fringes.

The frequency counter is equipped with a validation circuit that verifies the consistency, and repeatability of the Doppler signal. In other words, the circuit compares two Doppler frequencies, one computed based on 5 fringe-, and the second on 8 fringe-crossings. If the comparison of the two frequencies is within $\pm x$ % (x is user-specified, and is set equal to 1 in this work) of each other, then the data is accepted as being good.

Data thus validated is sent as a digital output to the computer for storage. One of the main advantages of the validation circuit is that it virtually eliminates signals from multiple particles in the laser measurement volume as being accepted as good data.

A1-6 Optical Train of the LDV System

The optical components employed in the LDV system were listed in Chapter III. A brief description of the major optical components is provided here. A good review of such components, for example, is provided by Durst et al. (1981). As mentioned before, the optical train of the laser system consists of, polarizers, beam splitters, collimator, prisms, mirrors, frequency shifter assemblies, beam stops, and steering modules.

The laser light is linearly polarized in the vertical direction. The polarity of the laser beam can be adversely affected due to internal reflections when it goes through different optical components. The polarizers change the polarization of the outgoing laser beam so that the desired polarity direction is achieved.

The beam splitters aid in splitting the beam into two. The path length through the beam splitter for each of the two beams is equal, so that the two are in phase. The two split beams will have equal intensity if the plane of polarity of the incoming laser beam is perpendicular to the plane containing the two outgoing beams. Thus, the plane of polarization of the incoming green beam is vertical and the two outgoing beams are contained by a horizontal plane. The same holds good for violet. The incoming blue beam is horizontally polarized, and its two outgoing beams are contained in a vertical plane.

The collimator is used to control the laser beam divergence. Controlling the beam divergence maximizes the intensity of the laser beam at the waist and ensures that the beam crossing point and the waist coincide. The prism is employed in splitting the laser beam into its constituent colors and the mirrors are used to reflect the laser beams.

The frequency shifter was discussed in Section A1.4. Multiple, frequency-shifted laser beams emerge from the frequency shifter. Only one of these beams is selected (based on the beam's position, at 25 mm, from the unshifted beam), tuned for peak power, and the other beams are literally blocked off by the beam stops. The beam stops have beam adjustable blockers that can be used to stop any desired beam(s).

The steering module contains a pair of antireflective coated glass wedges that can be rotated, and is used to steer the beam so that the crossing at the measurement volume is as close to being perfect as possible. For reasons of brevity, other optical components such as lenses, beam expanders, beam displacers, and photomultiplier tubes are not discussed here. More information about different optical components may be found in books that deal in LDV (e.g., Laser Velocimetry Systems, 1980)

Several errors and biases that are unique to the LDV system must be considered in estimating the uncertainty in the experimental measurements. These errors and biases are discussed in Appendix A2.

Appendix A2

Estimation of Experimental Uncertainty

Uncertainty in the experimental measurements is discussed in this section. The experimental uncertainty arises from (1) natural randomness due to sampling variations and (2) fixed errors called biases. Uncertainty estimates from both sources are addressed here. The uncertainty estimates simply provide the width of the error band within which a measured quantity is expected to lie (in the present case with 20 to 1 odds, or 95% probability).

A2.1 Measurement Bias in LDV Systems

Several types of measurement biases, such as velocity, filter, fringe or angle, and velocity gradient bias are encountered in LDV system measurements. Additional error could be introduced by the elements of the transformation matrix required for converting the fluid velocity components to the flume coordinates. These biases introduce a fixed error in the experimental measurements. The special panel report by Edwards (1989) describes the various biases encountered in LDV systems and recommends specific corrective measures. Some of these errors (velocity bias) can be “corrected” during post-processing of data, while others have to be rectified before obtaining the data.

The filter bias is introduced due to improper setting of the filter high and low limits, in comparison to the received signal from the photodetector. Such a filter setting can bias

the received signal either toward a high or low value. In this work, care was taken to open the filter wide enough that filter bias was eliminated. This was confirmed by checking the signal histogram by using the FIND (commercial software, TSI, Inc.) software.

Fringe bias is introduced when either an inadequate number of fringes is crossed by a scattering seed, or when signals from multiple seeds are accepted erroneously as a single signal. Single data realizations from multiple seed particles are reduced by the validation circuit that compares the consistency and repeatability of the Doppler signal based on a 5- and 8-fringe measurements to within 1%. When a frequency-shifting technique is employed, with the shift frequency greater than twice the Doppler shift, fringe bias is significantly reduced, though not completely eliminated. Also, care must be taken to include all possible flow angles that can possibly occur in a given flow condition. In the present experiments care was taken to ensure that all possible flow angles were included. That is, with proper shifting, fringe bias is insignificant compared to other uncertainty sources, in the present investigation.

Velocity bias occurs in LDV due to the inherent way in which measurements are effected with this technique. The arrival of a seed particle at the measurement volume is not independent of the fluid velocity, which brings it there. Faster traveling seed particles have a higher probability of crossing the laser measurement volume, and thus, uncorrected laser measurements will tend toward higher average velocity values. Several schemes have been proposed to remedy velocity bias problems; Edwards (1989) gives a good comparison of the different schemes. The 3-D inverse velocity scheme proposed by McLaughlin and Tiederman (1973) was adopted here, though other schemes such as sample and hold, time between measurements (Dimotakis, 1976), and transit time weighting (Buchhave et al.,

1979) were also included in the Fortran program, Menu3d. A comparison of the performance of various velocity bias correction schemes is provided in Balakrishnan and Dancey (1997). For the low data rate encountered in this work, the 3-D inverse velocity scheme compared most favorably with other published work (see, Balakrishnan and Dancey, 1994, and 1997). The implementation of the velocity bias scheme is discussed next.

A2.2 Implementation of Velocity Bias Correction

The flow mean quantities are calculated using the inverse velocity bias correction scheme (McLaughlin and Tiederman, 1973) as follows. Let x_i be the instantaneous quantity, whose ensemble mean, $\langle x \rangle$, needs to be estimated (ensemble average is denoted by “ $\langle \rangle$ ”). Then,

$$\langle x \rangle = \frac{\sum_{i=1}^N x_i F_i}{\sum_{i=1}^N F_i} \quad [\text{A2}\cdot\text{1}]$$

Where F_i is the bias correction or weighting factor, defined as,

$$F_i = \frac{1}{\sqrt{U_i^2 + V_i^2 + W_i^2}} \quad [\text{A2}\cdot\text{2}]$$

Where U_i , V_i , and W_i are the three velocity components, stream-wise, span-wise, and normal, respectively, in the flume coordinates. Here, x_i could be U , U^2 , or UW , etc.

Equations A2.1 and A2.2 were employed in this work. All of the results presented in this work have been velocity bias corrected using the 3-D correction scheme (McLaughlin and Tiederman, 1973) given by Equation A2.2. The error due to velocity bias (relative to the 3-D correction model, and *not absolute*), shown in Table A2.1, indicates that the maximum

error could be as high as 40%, though for most cases it is less than 10%. The maximum error occurs in the near-bed area, where the velocity is lower than at the core part of the flow.

A2.3 Uncertainty Due to Randomness

The LDV measurements, which are initially in the laser beam coordinate system, are transformed to the flume coordinate system during LDV data post-processing. The mutual locations of the laser beams, the angle between them, and other relevant information were measured during each day an experiment was conducted. These measurements were input (called the A-Matrix) to generate the transformation matrix required for the coordinate transformation. The A-Matrix elements and other constants used in each of the five packing density, and the single ball case are presented in Table A2.2.

The magnitude of the uncertainty in the LDV measurements depends on the uncertainty in measuring the quantities (angle between the beams and the beam orientation) that are used to compute the A-matrix elements, and on the randomness of the measurement process and data sampling (Moffat, 1988). The beam angle measurements that are used to compute the A-matrix elements were repeated numerous times to obtain a good estimate of the average uncertainty in beam angle measurements. The uncertainties in these measurements and in the velocity measurements themselves were then allowed to propagate through the transformation equations and the resulting uncertainty in the mean velocities, rms quantities, and the cross terms were estimated. The results of these uncertainty estimates (positive values of the uncertainties relative to the corresponding variable) are presented in table A2.3. Some of the relative uncertainties that are large (more than 100 %)

are for quantities that are rather small in magnitude, and mostly occur near the roughness elements.

Table A2.1. Velocity bias error summary for the streamwise component.

Pkg.	Location	<U>			u'			z/d
		NC ⁽¹⁾	3-D ⁽²⁾	% dev. ⁽³⁾	NC ⁽¹⁾	3-D ⁽²⁾	% dev. ⁽³⁾	
2	A, Bed	0.277	0.259	7	0.069	0.071	4	0.8893
	A, Core	0.348	0.337	3	0.063	0.063	1	2.0811
	B, Bed	0.162	0.143	14	0.06	0.061	3	0.0897
	B, Core	0.344	0.333	3	0.064	0.064	1	2.0811
	C, Bed	0.04	0.029	41	0.08	0.071	11	0.0897
	C, Core	0.353	0.342	3	0.064	0.065	1	2.0811
20	A, Bed	0.289	0.249	16	0.106	0.111	5	0.8969
	A, Core	0.521	0.516	1	0.05	0.051	4	4.5686
	B, Bed	0.256	0.233	10	0.083	0.082	0.2	0.5490
	B, Core	0.52	0.51	2	0.074	0.075	2	4.2127
	C, Bed	0.781	0.056	38	0.077	0.068	13	0.5490
	C, Core	0.531	0.513	3	0.094	0.088	7	4.2127
35	A, Bed	0.291	0.222	31	0.142	0.144	2	0.8893
	A, Core	0.658	0.642	3	0.105	0.108	3	3.5530
	B, Bed	0.216	0.159	35	0.136	0.128	6	0.7318
	B, Core	0.651	0.633	3	0.11	0.114	3	3.3954
	C, Bed	0.216	0.175	24	0.116	0.112	4	0.7939
	C, Core	0.652	0.636	3	0.106	0.109	3	3.4575
50	A, Bed	0.351	0.295	19	0.142	0.144	1	0.8818
	A, Core	0.708	0.693	2	0.106	0.109	2	3.5454
	B, Bed	0.402	0.36	11	0.13	0.135	4	0.8818
	B, Core	0.716	0.701	2	0.106	0.109	3	3.5454
	C, Bed	0.373	0.336	11	0.124	0.125	0.2	0.8818
	C, Core	0.711	0.696	2	0.106	0.109	3	3.5513
70	D, Bed	0.361	0.301	20	0.167	0.16	4	0.5657
	D, Core	1.102	1.09	1	0.132	0.132	1	5.3004
	E, Bed	0.401	0.346	16	0.165	0.161	3	0.5657
	E, Core	1.109	1.097	1	0.122	0.124	2	5.3004

¹ NC = No velocity bias correction effected

² McLaughlin and Tiederman, 1977

³ Absolute value of relative deviation presented. $\% dev. = \left| \frac{U_{NC} - U_{3D}}{U_{3D}} \right| 100$

Table A2-2. Transformation matrix elements.

Qty.	2%	20%	35%	50%	70%	Single Ball
θ_{vg}	31.315515	31.311106	30.783254	30.742385	31.352475	31.373199
x'	0.00761618	0.07906091	0.00526618	-0.012188	-0.0122881	0.07055915
y'	-0.2866872	-0.2699013	-0.2548688	-0.252187	-0.2980575	-0.2443802
z'	0.95799396	0.95963673	0.96696131	0.96760176	0.95446883	0.96710896
A_{11}	0.99968752	0.99888515	0.99931482	0.9993306	0.99888643	0.99777332
A_{21}	0.01361921	0.00768899	0.00860167	0.01098625	0.01089534	0.00353029
A_{31}	0.0209613	0.04657612	0.03599876	0.03489493	0.0459041	0.06660289
A_{12}	-0.0072989	0.00383863	0.00023578	-0.0017743	0.00344636	0.00706863
A_{22}	0.96103828	0.97014865	0.97112082	0.96727521	0.95351946	0.98737688
A_{32}	-0.2763189	-0.2424807	-0.2385881	-0.2537233	-0.3013117	-0.1582307
A_{13}	-0.0239079	-0.0470502	-0.0370114	-0.0365405	-0.0470534	-0.0663208
A_{23}	0.2760796	0.24238912	0.23843315	0.25349156	0.3011344	0.15834912
A_{33}	0.96083738	0.96903756	0.97045339	0.96664721	0.95242011	0.98515335
Flume Angle	0.2%	0.2%	0.8%	1%	1.2%	0.2%
LDV Angle	3.8°	3.8°	3.8°	3.8°	3.8°	4.1°

Note: θ_{vg} = Angle between the two optical axes of the LDV system

x' , y' & z' = unit vectors perpendicular to the plane containing the three pairs beams.

A_{11} - A_{33} = Elements of the A-Matrix.

Flume angle = slope of the flume

LDV angle = slope of the LDV traverse table with the horizontal

Table A2.3. Summary of uncertainty from the beam angle measurements.

Packing	Remarks	Uncertainty (%)								
		<U>	<V>	<W>	(u') ²	(v') ²	(w') ²	<uv>	<uw>	<vw>
2(A)	NB	0.8	23.3	1.9	4.3	15.2	6.5	10.7	0.9	3.4
2(A)	C	0.6	30.6	6.5	4.7	10.9	6.6	12.5	1.8	6.2
2(B)	NB	1.3	33.3	4.1	4.2	16.2	6.4	10.3	1.7	6
2(B)	C	0.6	49.1	6.6	4.6	11.3	6.5	12.3	1.8	6.2
2(C)	NB	7.4	39.9	3.3	4.2	22.5	6.5	9.6	1.6	5.7
2(C)	C	0.6	24.7	7.2	4.7	11.1	6.6	12.4	1.7	6.1
20(A)	NB	1.3	94	15.4	4.4	30	6.9	10	0.8	2.8
20(A)	C	0.7	12.5	9.9	10.6	11.4	12	29.1	8.7	31
20(B)	NB	1.1	516	7.2	4.4	21	6.6	10.3	2	6.9
20(B)	C	0.4	78.7	93.3	4.5	13.1	6.6	11.5	1.7	6.2
20(C)	NB	4.3	99.4	12.4	5	17.4	7.5	12.4	3	10.6
20(C)	C	0.6	38.6	48.2	5.3	13.2	7.6	14.3	1.7	6.1
35(A)	NB	1.9	66	110	4.3	39.3	6.7	9.5	0.5	2
35(A)	C	0.5	26.2	21.7	4.3	17.6	6.5	10.6	1.8	6.5
35(B)	NB	2.4	46.1	28.7	4.4	40.7	6.7	9.7	2.2	8.1
35(B)	C	0.5	20.5	27.4	4.2	19.6	6.4	10.2	1.7	6
35(C)	NB	1.9	74.7	61.1	4.3	23.4	6.6	10.2	2.6	9.3
35(C)	C	0.5	27.8	38.8	4.3	17.9	6.4	10.4	1.7	6.2
50(A)	NB	1.3	119	39.9	4.1	40	6.3	9.1	0.6	2.3
50(A)	C	0.4	26.1	545	4.2	20.5	6.3	10	1.8	6.6
50(B)	NB	1.1	22.6	13.3	4.1	32.4	6.4	9.4	1.1	4
50(B)	C	0.4	25.3	68.3	4.1	26.4	6.4	9.6	1.7	6.2
50(C)	NB	1.1	28.7	16.4	4.1	26.9	6.4	9.6	1.5	5.3
50(C)	C	0.4	35.2	143	4.2	23.3	6.4	9.9	1.8	6.5
70(D)	NB	1.5	40.4	238	4.2	33.3	6.4	9.3	2.2	7.7
70(D)	C	0.3	13.3	15.4	4.2	18.3	6.4	10.2	1.6	5.8
70(E)	NB	1.3	33.8	236	4.2	31.4	6.4	9.3	2	7.1
70(E)	C	0.3	12	15.1	4.2	23.9	6.4	9.6	1.6	5.7
1 ball	NB	1.2	47.6	0.9	2.6	2.8	2.7	8.1	0.8	3.1

Note: NB = Flow Near Bed; C = Core part of the flow

Vita

Mahalingam Balakrishnan (Mahesh Bala), was born in Ooty, India. He is the second son of Kalyani and Balakrishnan.

He obtained his undergraduate engineering degree in Mechanical Engineering from Regional Engineering College at Bhopal, India in June, 1985. He worked as a boiler construction engineer with Bharat Heavy Electricals Limited for four years. In June of 1989 he married Anu Thirumurthy, and started his Master's degree program in the fall of 1989 at the University of Alabama, Tuscaloosa, Alabama. He began his doctoral program at the Department of Mechanical Engineering at Virginia Polytechnic Institute and State University in fall 1992.